technische universität
dortmund

Analysis of Rare Hadronic Decay Modes and Simulation Studies for the Scintillating Fibre Tracker at the LHCb Experiment

Dissertation zur Erlangung des akademischen Grades
Dr. rer. nat.

vorgelegt von

Moritz Demmer
aus Essen

Fakultät Physik
Technische Universität Dortmund

Dortmund, im November 2018

Der Fakultät Physik der Technischen Universität Dortmund zur Erlangung des akademischen Grades eines Doktors der Naturwissenschaften vorgelegte Dissertation.

Datum des Einreichens der Arbeit: 23. November 2018
Datum der mündlichen Prüfung: 17. Januar 2019

1. Gutachter: Prof. Dr. Bernhard Spaan
2. Gutachter: Prof. Dr. Kevin Kröninger

Vorsitzender der Prüfungskommission:	Prof. Dr. Heinz Hövel
Vertreter der wissenschaftlichen Mitarbeiter:	Dr. Julia Nase
Vorsitzender des Promotionsausschusses:	Prof. Dr. Thomas Weis

Abstract

The work presented in this thesis comprises two individual topics: While the first part presents a branching ratio measurement of the decay $B_s^0 \to K_S^0 K_S^0$, the second part discusses the author's contribution to the simulation of the upgraded LHCb detector.

To reduce systematic uncertainties, the branching ratio is measured normalised to the branching ratio $\mathcal{B}(B^0 \to \phi K_S^0)$. The analysed data sample corresponds to an integrated luminosity of $3\,\mathrm{fb}^{-1}$ of pp collisions recorded at centre-of-mass energies of 7 and 8 TeV by the LHCb experiment. The branching ratio has been measured as:

$$\mathcal{B}(B_s^0 \to K_S^0 K_S^0) = \left(22.9 \pm 7.3\,(\text{stat}) \pm 1.7\,(\text{syst}) \pm 2.2\,(\mathcal{B}(B^0 \to \phi K_S^0)) \pm 1.3\,({}^{f_d}\!/\!{}_{f_s})\right) \cdot 10^{-6}\,.$$

The result is compatible within $1.7\,\sigma$ with results for the branching ratio $\mathcal{B}(B_s^0 \to K^0 \overline{K}^0)$ from various theory predictions and a measurement performed by the Belle experiment.

The performance of the *Scintillating Fibre* (SciFi) tracker, which will be installed for the upgrade of the LHCb experiment during the Long Shutdown 2 of the LHC, depends mainly on the light yield of the scintillating fibres. Since this light yield is reduced over time by radiation induced damage, the correct description of the light yield attenuation depending on the integrated luminosity is a crucial part of the tracker's simulation. The second part of the thesis describes the construction of a software framework that allows to simulate lookup maps for this attenuation as a function of the hit position, which are then used in the LHCb detector simulation.

Kurzfassung

Diese Arbeit umfasst zwei verschiedene Hauptthemen: Während im ersten Teil die Messung des Verzeigungsverhältnis des Zerfalls $B_s^0 \to K_S^0 K_S^0$ beschrieben wird, zeigt der zweite Teil den Beitrag des Autors zur Simulation des LHCb Detektors nach seinem Upgrade.

Um systematische Unsicherheiten zu verringern, wird das Verzeigungsverhältnis relativ zum Verzeigungsverhältnis $\mathcal{B}(B^0 \to \phi K_S^0)$ gemessen. Der verwendete Datensatz entspricht einer integrierten Luminosität von $3\,\mathrm{fb}^{-1}$ von pp-Kollisionen, aufgenommen vom LHCb-Experiment bei Schwerpunktenergien von 7 und 8 TeV. Die Messung des Verzweigungsverhältnis ergibt:

$$\mathcal{B}(B_s^0 \to K_S^0 K_S^0) = \left(22.9 \pm 7.3\,(\text{stat}) \pm 1.7\,(\text{syst}) \pm 2.2\,(\mathcal{B}(B^0 \to \phi K_S^0)) \pm 1.3\,({}^{f_d}\!/\!{}_{f_s})\right) \cdot 10^{-6}\,.$$

Das Ergebnis ist innerhalb von $1.7\,\sigma$ kompatibel mit den Werten für das Verzweigungsverhältnis $\mathcal{B}(B_s^0 \to K^0 \overline{K}^0)$ aus verschiedenen theoretischen Vorhersagen sowie aus der Messung durch das Belle-Experiment.

Die Leistungsfähigkeit des *Scintillating Fibre* (SciFi) Tracker, welcher für das Upgrade des LHCb Detektor während des Long Shutdown 2 des LHC installiert wird, hängt hauptsächlich von der Lichtausbeute der szintillierenden Fasern ab. Da diese Lichtausbeute durch strahlungsinduzierte Schäden reduziert wird, ist eine korrekte Beschreibung dieser Abschwächung in Abhängigkeit von der integrierten Luminosität ein entscheidender Teil der Detektorsimulation. Der zweite Teil der Arbeit beschreibt den Aufbau eines Software-Frameworks, das es ermöglicht, die Lichtausbeuteabschwächung als Funktion der Hit-Position zu simulieren. Dies wird im LHCb Software-Framework für die Detektorsimulation verwendet.

Contents

Appendices

Introduction

The field of particle physics seems to be in a dilemma: Even though its big theory, the *Standard Model of Particle Physics* (SM) [1–3], which describes the fundamental particles and their interactions and thus the emergence and decay of matter and antimatter, has been very successful with its predictions to date, it does not succeed in explaining the composition of the known universe: What are dark matter and dark energy? Why is the universe dominated by matter although a production in equal parts of matter and antimatter is observed? What causes the relative weakness of the gravitational force and how does it relate to the other fundamental forces? While experiments conducted by particle physicists collect datasets larger than ever at energies previously unattainable in a laboratory environment, the SM is completed and established further instead of being contradicted by experimental results.

According to our current understanding, three conditions had to be met in the early universe in order to explain the asymmetry between matter and antimatter with the laws of particle physics [4]:

1.) The violation of the conservation of the baryon number.

2.) The universe has departed from the thermal equilibrium at some point in the past.

3.) The violation of the C (charge) as well as the CP (charge and parity) symmetries.

Although the SM includes different types of CP violation that were first measured in 1964 in the decays of neutral kaons [5], its magnitude is not enough for the observed matter-antimatter imbalance. This leads to the fact that high precision measurements for searches of potential new sources of CP violation and possibly tiny inconsistencies in the SM are an important field of modern particle physics.

The *Large Hadron Collider beauty* (LHCb) experiment at the *Large Hadron Collider* (LHC), located beneath the franco-swiss border near the city of Geneva, specialises on the so called indirect search for New Physics beyond the SM, i.e. it pursues said precision measurements by investigating decays of heavy flavoured hadrons whose observables are precisely predicted in the SM but that could be altered by processes beyond the SM. Among others, these measurements include the determination of CP violation parameters and branching ratios of rare decays. LHCb benefits from the immense number of heavy flavoured hadrons produced in proton-proton collisions at centre-of-mass energies of currently $\sqrt{s} = 13$ TeV. On the other hand however, the hadronic environment of proton-proton collisions poses a challenge for the analysis of hadron decay processes, especially with purely hadronic final states. Nevertheless, the LHCb experiment has collected the world's largest data sample of beauty and charm hadron decays to date.

This thesis presents the search for the rare hadronic decay $B_s^0 \to K_S^0 K_S^0$ and performs a measurement of its branching ratio normalised to the branching ratio of the decay $B^0 \to \phi K_S^0$, using data collected by the LHCb experiment in the years 2011–2012 (Run I) and 2015–2016 (Run II). While the branching ratio calculation itself is a probe for new physics beyond the SM, it also serves as a preparation for a potential analysis of CP violation in these decay channels. The considered final states are $K_S^0 \to \pi^+\pi^-$ and $\phi \to K^+K^-$. As such a measurement is a complex and challenging undertaking, it was conducted in close collaboration with another member of the Dortmund LHCb group, Timon Schmelzer. The chapters describing the branching ratio measurement focus on the author's own work. To draw a full picture of the analysis however, it is necessary to include all contributions. While this thesis shows the result for the Run I datasets, the final publication will consists of the combined result for the Run I and Run II datasets.[1] The part of Timon's work that is presented in this thesis comprises the selection of signal candidates for the decay $B_s^0 \to K_S^0 K_S^0$ (see Chapter 5) and the study of some of the systematic uncertainties (see Section 6.2). He too will present the results of the Run I subset and additionally those of the Run II subsets in his own Ph.D. thesis:

> T. Schmelzer, *Observation of the Decay* $B_s^0 \to K_S^0 K_S^0$ *at the LHCb Experiment*, PhD thesis, TU Dortmund University, in preparation

In order to increase the sensitivity of rare heavy flavour processes, e.g. through lower statistical uncertainties, the LHCb experiment is planning to record data at an instantaneous luminosity of $2 \cdot 10^{33}\ \mathrm{cm}^{-2}\ \mathrm{s}^{-1}$ after the Long Shutdown 2, which will take place in 2019–2020. In order to benefit from the higher instantaneous luminosity, the LHCb detector will undergo an extensive upgrade of its components and trigger system [7]. The even higher multiplicity of particle tracks calls for a new tracking system, which includes a new downstream tracker with a new technology not previously used at LHCb before: The *Scintillating Fibre* (SciFi) tracker [8]. Charged particles passing through the scintillating fibres produce scintillating photons that are guided through the fibre by total reflections and can then be measured at the upper and lower end of the tracker in order to determine hit positions. One challenge for the simulation of the SciFi tracker, be it for performance studies or to provide simulated decays for physics analyses, is the correct description of radiation induced damage in the scintillating fibres, which can

---

[1] Since the internal review process of the branching ratio measurement is not completed at the time of submission of this thesis, it is possible that the result presented in this thesis will differ from that shown in the final publication.

lead to a reduced light yield. Since the SciFi tracker's performance mainly depends on the light yield, this may in turn lead to decreasing tracking efficiency over its lifetime. The work presented in the second part of this thesis was the main contribution for the construction of a software framework that allows to simulate lookup maps for the light yield attenuation as a function of the hit position, in dependence of a dose map for a given integrated luminosity. The framework also enables an easy re-simulation of the lookup maps for changed conditions, e.g. a revision of dose maps. This allows to use the lookup maps in the centralised production of simulation samples.

Outline

Chapter 1 introduces the theoretical foundations, e.g. the phenomenology of neutral meson mixing and decays and the mechanisms of $\mathcal{CP}$ violation. Furthermore, it provides a motivation for the analysis of the decays $B^0 \to \phi K^0_\mathrm{S}$ and $B^0_s \to K^0_\mathrm{S} K^0_\mathrm{S}$. The LHC and the LHCb detector are described in Chapter 2, including an introduction for the upgrade of the LHCb detector. Chapter 3 gives an overview of the general strategy pursued in the branching ratio measurement and discusses methods applied in the course of the analysis. The selection of signal candidates of the normalisation channel, $B^0 \to \phi K^0_\mathrm{S}$, and the main channel, $B^0_s \to K^0_\mathrm{S} K^0_\mathrm{S}$, are presented in Chapter 4 and Chapter 5, respectively. The actual measurement follows in Chapter 6. Last, but not least, Chapter 7 describes the SciFi tracker as well as the basic functionality of scintillating fibres and the process of radiation damage, before discussing the simulation and results of the light yield attenuation lookup maps. The thesis closes with a summary and a conclusion.

1 Theory

The *Standard Model of Particle Physics* (SM) is a relativistic quantum field theory, which describes the properties of — from today's point of view — all elementary subatomic particles and their weak, strong, and electromagnetic interactions. Even though astronomy experiments like the Planck space observatory and their results based on the Standard Model of cosmology (ΛCDM model) lead to the conclusion that only 4.9 % of our universe consist of ordinary (anti-)matter [9] and can therefore be explained by the Standard Model, most of its predictions have been proven right in the last decades — the latest being the discovery of Higgs boson production in association with a top quark pair [10, 11] and the discoveries of Higgs boson decays to bottom quarks [12, 13] and tau leptons [14, 15] by the ATLAS and CMS collaborations at the Large Hadron Collider (see Section 2.1).

This chapter starts with a short overview of the Standard Model. Furthermore, Section 1.2 summarizes the physics of neutral mesons systems. The chapter closes with descriptions of the investigated decays $B^0 \to \phi K^0_S$ and $B^0_s \to K^0_S K^0_S$ in Section 1.3. If not stated otherwise, the information and notation used throughout this chapter is based on Refs. [16–20].

1.1 The Standard Model of Elementary Particles

According to the *Standard Model of Particle Physics* (SM), the matter observed in our universe consists of two types of fundamental particles: leptons (l) and quarks (q), which are fermions with a spin $S = \frac{1}{2}$, and bosons that carry an integer spin of $S = 0$ (scalar bosons) or $S = 1$ (vector bosons). In total there are six leptons and six quarks, as depicted in Fig. 1.1, and twelve corresponding anti- particles. They are divided into three generations or families, with an increasing mass from the first to the third family.

There are three fundamental leptons with an electric charge of $-e_0$, where e_0 is the elementary charge, namely the electron (e^-) the muon (μ^-) and the tauon (τ^-), and the three corresponding neutrinos electron neutrino (ν_e), muon neutrino (ν_μ) and tau neutrino (ν_τ) that have no electrical charge. The six quarks can be classified as either so called up-type quarks with electric charge $\frac{2}{3}e_0$ — in particular the up quark (u), charm quark (c) and top quark (t) — and three so called down-type quarks with charge $-\frac{1}{3}e_0$, namely the down quark (d), strange quark (s) and beauty or bottom quark (b).

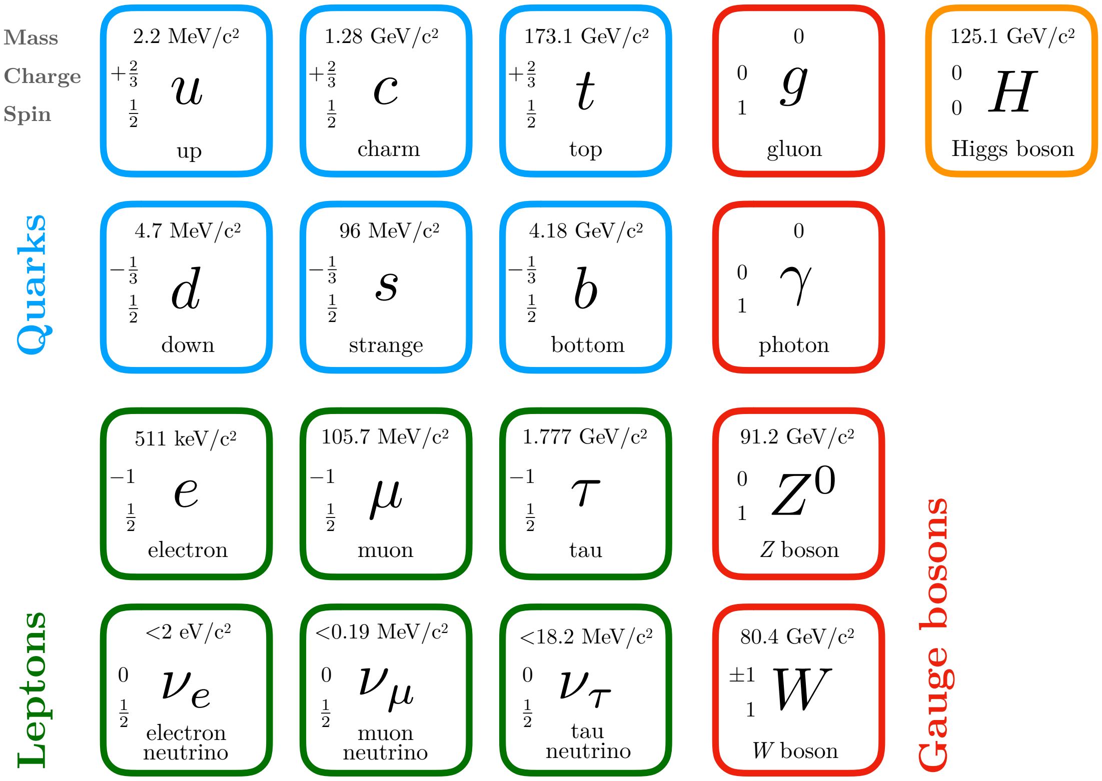

Figure 1.1 – Schematic depiction of the fundamental particles and their properties in the Standard Model of Particle Physics. The fermions — quarks and leptons — arise in three generations. Each of the generations contains up- and down-type quarks, a charged lepton, and an accompanying neutrino. The particle properties are taken from [20]. Figure from Ref. [21].

The anti-particles of leptons and quarks are obtained with a *CP* transformation of the corresponding particles and therefore carry an opposite charge and parity but share the same mass and spin with their particle equivalent. Anti-particles are denoted with a bar ($\overline{q}$, $\overline{\nu}$) or in case of the charged leptons with a plus sign for their positive electric charge of $Q = +e_0$ (e^+, μ^+, τ^+).
The so called gauge bosons (with $S = 1$) mediate the three forces that enables different interactions between elementary particles: the massless gluon (g) is the mediator of the strong force, the also massless photon (γ) is the mediator of the electromagnetic force and finally the massive Z^0 and $W^\pm$ are mediators of the weak force. The Higgs boson with $S = 1$ is the last of the elementary particles that was only discovered in the last years [22].

The Lagrangian that defines the dynamics of the Standard Model is a sum of two terms:

$$\mathcal{L}_{\text{SM}} = \mathcal{L}_{\text{SU}(3)_C} + \mathcal{L}_{\text{SU}(2)_L \otimes \text{U}(1)_Y}. \tag{1.1}$$

The first term is the Lagrangian of *Quantum Chromodynamics* (QCD), a quantum field theory with an SU(3) symmetry group, that describes the strong interaction. The second term describes the *Glashow-Weinberg-Salam* (GWS) model [3, 23], a theory that unifies the electromagnetic with the weak interaction to the electroweak interaction.

The strength of a particle interactions depends on a coupling constant and the particle's charge that corresponds to the interaction — this charge has always an opposite sign for an anti-particle. For the strong force, this charge is the so called colour charge that is only carried by quarks and gluons. Hence, leptons do not interact strongly. A property of the strong interaction is the asymptotic freedom of quarks [24, 25]: The coupling of the strong interaction increases with larger distances and lower energies, while it decreases for small length scales. Another characteristic of the strong interaction is the confinement of quarks, i.e. they do not occur individually but only in bound states. These so called hadrons can be further divided into mesons and baryons [26]. The former consist of a quark anti-quark pair ($q\overline{q}$), the latter of three quarks or anti-quarks. Two prominent examples of baryons are the constituents of atoms: protons consist of the quarks (uud) and neutrons have a quark content of (udd). In the last year, the LHCb experiment at the Large Hadron Collider (see Chapter 2, Page 25) also observed exotic hadron states: so called tetraquarks ($q\overline{q}q\overline{q}$) [27, 28] and pentaquark ($qqqq\overline{q}$) [29] states. The only quark that was not observed in a bound state is the top quark. Because of its high mass of $m_t = (173.0 \pm 0.4)$ GeV [20] the top quark decays too quick to form a hadron.

The spontaneous symmetry breaking through the Englert-Brout-Higgs-Guralnik-Hagen-Kibble[1] mechanism [30–32] is the reason why the $W^{\pm}$ and Z^0 gauge bosons have mass is. In order to also attribute mass to the fundamental fermions, one has to introduce a mechanism referred to as the Yukawa coupling that describes the coupling of fermions to the Higgs field. On the supposition that neutrinos are massless, the mass eigenstates of leptons are also the eigenstates of the weak interaction. This is not possible for the quark sector. Here, one can only define either the up- or down-type quarks mass eigenstates to be also eigenstates to the weak interaction. The most common convention is to select the up-type quarks. The mass eigenstates of the down-type quarks (d, s, b) are connected to their weak eigenstates (d', s', b') trough the

---

[1] For simplicity shortened to "Higgs" for the rest of this chapter.

Cabibbo-Kobayashi-Maskawa (CKM)[2] matrix $\boldsymbol{V}_{\text{CKM}}$[33]:

$$\begin{pmatrix} d' \\ s' \\ b' \end{pmatrix} = \boldsymbol{V}_{\text{CKM}} \begin{pmatrix} d \\ s \\ b \end{pmatrix}, \quad \text{with } \boldsymbol{V}_{\text{CKM}} = \begin{pmatrix} V_{ud} & V_{us} & V_{ub} \\ V_{cd} & V_{cs} & V_{cb} \\ V_{td} & V_{ts} & V_{tb} \end{pmatrix}. \tag{1.2}$$

$\boldsymbol{V}_{\text{CKM}}$ is a unitary and complex matrix that can therefore be described by three real rotation angles and one complex phase, which becomes apparent when writing the matrix in the Chau-Keung parametrization[34], which is defined as:

$$\boldsymbol{V}_{\text{CKM}} = \begin{pmatrix} c_{12}c_{13} & s_{12}c_{13} & s_{13}\mathrm{e}^{-i\delta} \\ -s_{12}c_{23} - c_{12}s_{23}s_{13}\mathrm{e}^{i\delta} & c_{12}c_{23} - s_{12}s_{23}s_{13}\mathrm{e}^{i\delta} & s_{23}c_{13} \\ s_{12}s_{23} - c_{12}c_{23}s_{13}\mathrm{e}^{i\delta} & -s_{23}c_{12} - s_{12}c_{23}s_{13}\mathrm{e}^{i\delta} & c_{23}c_{13} \end{pmatrix}, \tag{1.3}$$

with the complex phase δ and $s_{ij} = \sin\theta_{ij}$, $c_{ij} = \cos\theta_{ij}$. Since it violates the $\mathcal{CP}$[3] symmetry of the Standard Model Lagrangian, defined in Eq. (1.1), this same phase δ is the only cause of $\mathcal{CP}$ violation in the SM.

Because it allows for a better display of the hierarchy of the CKM matrix, one of the most common parametrizations is the Wolfenstein parametrization [35] with the parameters A, λ, ρ and η, which are defined by:

$$\lambda = s_{12} \tag{1.4}$$

$$A\lambda^2 = s_{23} \tag{1.5}$$

$$A\lambda^3 = s_{13}\mathrm{e}^{-i\delta}. \tag{1.6}$$

By means of a series expansion of the parameter λ one arrives at the following representation of the CKM matrix:

$$\begin{aligned} \boldsymbol{V}_{\text{CKM}} = &\begin{pmatrix} 1 - \frac{1}{2}\lambda^2 & \lambda & A\lambda^3(\rho - i\eta) \\ -\lambda & 1 - \frac{1}{2}\lambda^2 & A\lambda^2 \\ A\lambda^3(1 - \rho - i\eta) & -A\lambda^2 & 1 \end{pmatrix} \\ &+ \begin{pmatrix} -\frac{1}{8}\lambda^4 & 0 & 0 \\ \frac{1}{2}A^2\lambda^5[1 - 2(\rho + i\eta)] & -\frac{1}{8}\lambda^4(1 + 4A^2) & 0 \\ \frac{1}{2}A\lambda^5(\rho + i\eta) & \frac{1}{2}A\lambda^4[1 - 2(\rho + i\eta)] & -\frac{1}{2}A^2\lambda^4 \end{pmatrix} \\ &+ \mathcal{O}(\lambda^6). \end{aligned} \tag{1.7}$$

From this representation, it becomes evident that quark transitions are most probable within one generation and are suppressed for transitions to the next (second after next)

---

[2] Cabibbo first introduced a quark mixing model for the first two quark generations, Kobayashi and Maskawa later extended his theory for the third generation.

[3] $\mathcal{CP}$ stands for the operation of charge conjugation C and parity P. In particle physics, parity is understood as the point reflection of a particle in space.

generation, e.g. by $\mathcal{O}(\lambda)$ for transitions between the 1^{st} and 2^{nd} generation and up to $\mathcal{O}(\lambda^3)$ for 1^{st} to 3^{rd} generation transitions.
Requiring the unitarity of the CKM matrix $\boldsymbol{V}^{\dagger}_{\text{CKM}}\boldsymbol{V}_{\text{CKM}} = 1$, one ends up with the following unitarity conditions:

$$\begin{aligned}&\sum_i |V_{ik}|^2 = 1\\&\sum_k V_{ik}V^*_{ik} = 0\\&\text{with } i \in \{u,c,t\} \text{ and } k \in \{d,s,b\}.\end{aligned} \tag{1.8}$$

The six vanishing relations can be interpreted as triangles in the complex plane, with very different shapes but the same area, proportional to the Jarlskog parameter [36]:

$$J = \pm\mathcal{I}\text{m}(V_{ik}V^*_{il}V_{jl}V^*_{jk}) \quad \text{with } i \neq j, l \neq k, \tag{1.9}$$

which can be seen as a good measure for $\mathcal{CP}$ violation in the electroweak sector, independent of phase-conventions [20].
Because of it sides being in the same order in λ of $\mathcal{O}(\lambda^3)$ and therefore having interior angles of the order $\mathcal{O}(1)$, the triangle with the unitarity condition

$$V_{ud}V^*_{ub} + V_{cd}V^*_{cb} + V_{td}V^*_{tb} = 0 \tag{1.10}$$

is the most frequently used and is thereby often referred to as *the* CKM triangle. As can be seen in Fig. 1.2, dividing Eq. (1.10) by $V_{cd}V^*_{cb}$, leads to a triangle that is well aligned in the complex $\bar{\rho}$-$\bar{\eta}$-plane. Its apex is given as

$$\bar{\rho} + i\bar{\eta} = -\frac{V_{ud}V^*_{ub}}{V_{cd}V^*_{cb}}, \tag{1.11}$$

while the three angles are defined as

$$\alpha = \arg\left(-\frac{V_{td}V^*_{tb}}{V_{ud}V^*_{ub}}\right), \quad \beta = \arg\left(-\frac{V_{cd}V^*_{cb}}{V_{td}V^*_{tb}}\right), \quad \gamma = \arg\left(-\frac{V_{ud}V^*_{ub}}{V_{cd}V^*_{cb}}\right) \tag{1.12}$$

and furthermore its three sides are

$$R_u = \left|\frac{V_{ud}V^*_{ub}}{V_{cd}V^*_{cb}}\right|, \quad R_t = \left|\frac{V_{td}V^*_{tb}}{V_{cd}V^*_{cb}}\right|, \quad R_c = \left|\frac{V_{cd}V^*_{cb}}{V_{cd}V^*_{cb}}\right|. \tag{1.13}$$

Because of the involved CKM matrix elements, this triangle corresponds to many processes that involve neutral B^0 ($|\,\bar{b}d\,\rangle$) mesons. By measuring the corresponding elements of the CKM matrix in flavour-physic processes, one can determine the parameters of the CKM triangle. Hence, one possible test of the SM mechanism with indirect searches for New Physics is to find contradictions in these measurements, e.g. $\alpha + \beta + \gamma > 180^\circ$ or an open apex. As depicted in Fig. 1.2, this can be tested with a combined fit of all measurements of the CKM triangle parameters and therefore overconstraining the apex.

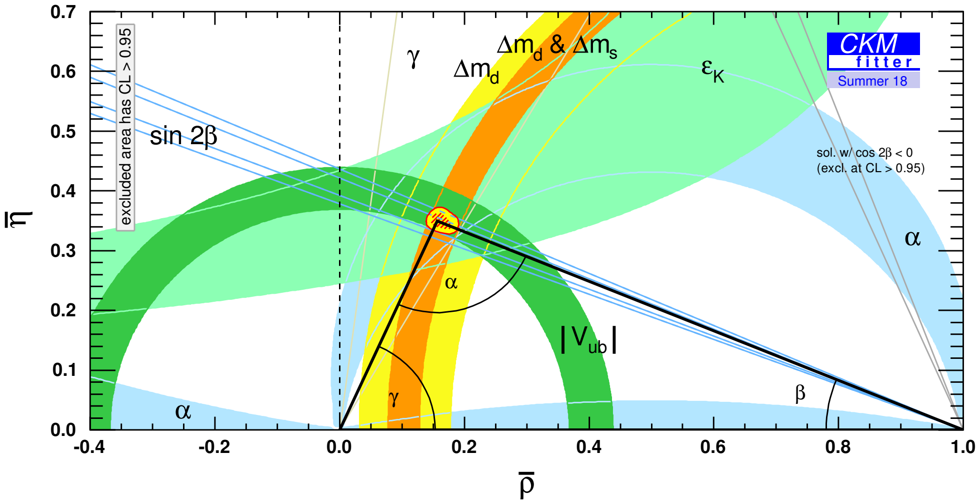

Figure 1.2 – The CKM triangle in the complex $\bar\rho$-$\bar\eta$-plane [37]. The triangle is obtained by dividing the CKM unitarity relation $\sum_{i=u,c,t} V_{id}V_{ib}{}^* = 0$ by $V_{cd}V_{cb}^*$. The different colour bands represent the experimental constraints on the triangle parameters. The red hashed region is the 68 % confidence level from a global fit of all experimental constraints to overconstrain the triangle's apex.

As mentioned before, it is also possible to obtain other unitarity triangles from the remaining unitarity relation, e.g.

$$V_{us}V_{ub}^* + V_{cs}V_{cb}^* + V_{ts}V_{tb}^* = 0. \tag{1.14}$$

Because it has to sides with a length $\mathcal{O}(\lambda^2)$ and $\mathcal{O}(\lambda^4)$ and is hence nearly degenerated, the triangle itself is today of no greater use for the study of CKM unitarity. But its angle

$$\beta_s = \arg\left(-\frac{V_{ts}V_{tb}^*}{V_{cs}V_{cb}^*}\right) \tag{1.15}$$

on the other hand is of great interest, since it enters B_s^0 meson mixing is therefore and important observable for $\mathcal{CP}$ violation in the B_s^0 meson sector, e.g. in the decay $B_s^0 \to K_S^0 K_S^0$, see Section 1.3.

1.2 Neutral Meson Systems

This section elaborates on the formalism of neutral meson systems, especially their mixing and decay mechanisms, and is based on the descriptions in Refs. [16, 17, 19, 20]. As introduced in Section 1.1, bound states consisting of a quark and an anti-quark $|\, q\bar{q}'\,\rangle$ are called mesons. For a neutrally charged state, both quarks are either up- or down-type quarks. While lighter mesons, e.g. $|\, \phi\,\rangle = |\, s\bar{s}\,\rangle$, decay predominantly via electromagnetic or strong interactions, heavier mesons, e.g. $|\, B^0\,\rangle = |\, \bar{b}d\,\rangle$, only decay via the weak interaction, which enables effects like mixing to their anti- particles and $\mathcal{CP}$ violation.

The neutral mesons occur as either $|\, P^0\,\rangle$ or $|\, \bar{P}^0\,\rangle$ with opposite flavour content but a common mass m_0 and are eigenstates of the electromagnetic and strong interactions. Throughout this section, P^0 may refer to either a K^0, D^0, B^0 or a B_s^0 meson. As a consequence of the weak interaction, P^0 and $\bar{P}^0$ are able to decay. Furthermore, they mix, i.e. oscillate between the two states $P^0/\bar{P}^0$ before decaying, since any conservation law that is respected by the weak interaction forbids real or virtual transitions to common states.

1.2.1 Neutral Meson Mixing

In the Wigner-Weisskopf approximation [38, 39], the beam of an oscillating and decaying neutral meson P^0 is described, in its restframe, by a time dependent wave function

$$|\, \psi(t)\,\rangle = \psi_1(t)|\, P^0\,\rangle + \psi_2(t)|\, \bar{P}^0\,\rangle, \tag{1.16}$$

with the proper time t. Its time-evolution is given by a Schrödinger-like differential equation:

$$i\frac{\mathrm{d}}{\mathrm{d}t}\begin{pmatrix}\psi_1\\ \psi_2\end{pmatrix} = \boldsymbol{H}\begin{pmatrix}\psi_1\\ \psi_2\end{pmatrix} = (\boldsymbol{M} - i\boldsymbol{\Gamma})\begin{pmatrix}\psi_1\\ \psi_2\end{pmatrix}. \tag{1.17}$$

The 2×2 Hamiltonian $\boldsymbol{H}$ is not Hermitian, which allows the mesons to decay and not only oscillate. Thus, the matrices $\boldsymbol{M}$ and $\boldsymbol{\Gamma}$ are Hermitian and since $\mathcal{CPT}$ conservation is assumed in the SM, decay widths and masses of P^0 and $\bar{P}^0$ are assumed to be identical, which leads to the fact that $M_{11} = M_{22} \equiv m$, $M_{21} = M_{12}^*$, $\Gamma_{11} = \Gamma_{22} \equiv \Gamma$, and $\Gamma_{21} = \Gamma_{12}^*$. Subsequently, Eq. (1.17) becomes

$$\boldsymbol{H}\begin{pmatrix}\psi_1\\ \psi_2\end{pmatrix} = \begin{pmatrix} m - {}^{i}\!/\!{}_{2}\Gamma & M_{12} - {}^{i}\!/\!{}_{2}\Gamma_{12} \\ M_{12}^* - {}^{i}\!/\!{}_{2}\Gamma_{12}^* & m - {}^{i}\!/\!{}_{2}\Gamma \end{pmatrix}\begin{pmatrix}\psi_1\\ \psi_2\end{pmatrix}. \tag{1.18}$$

While intermediate states that contribute to $\boldsymbol{M}$ are virtual, physical states, to which both P^0 and $\bar{P}^0$ can decay, contribute to $\boldsymbol{\Gamma}$.
Since $\boldsymbol{H}$ is not Hermitian, the eigenvalues of the two eigenstates of $\boldsymbol{H}$ are complex:

$$\begin{aligned} \mu_a &= m_a - {}^i\!/\!{}_2\Gamma_a \\ \mu_b &= m_b - {}^i\!/\!{}_2\Gamma_b . \end{aligned} \tag{1.19}$$

Here, m_a / m_b are the masses and Γ_a / Γ_b are the decay widths of the eigenstates P_a and P_b, respectively. The characterizing quantities of a meson system, are the average and the differences of their masses and decay widths:

$$\begin{aligned} m &= \frac{m_a + m_b}{2}, & \Gamma &= \frac{\Gamma_a + \Gamma_b}{2}, \\ \Delta m &= m_a - m_b , & \Delta\Gamma &= \Gamma_a - \Gamma_b . \end{aligned} \tag{1.20}$$

For the $B^0 - \bar{B}^0$ and $B_s^0 - \bar{B}_s^0$ systems, the labels a and b are chosen to correspond to the mass of the eigenstates: $a = H$ for the heavy eigenstate, and $b = L$ for the light eigenstate.[4] Hence, Δm is positive, while the sign of $\Delta\Gamma$ has to be determined experimentally. Under the condition that $\mathcal{CPT}$ symmetry is conserved, the mass eigenstates can be expressed in terms of the flavour eigenstate P^0 and $\bar{P}^0$ as

$$\begin{aligned} |P_H\rangle &= p|P^0\rangle + q|\bar{P}^0\rangle, \\ |P_L\rangle &= p|P^0\rangle - q|\bar{P}^0\rangle. \end{aligned} \tag{1.21}$$

While the signs in front of p and q are a convention, they are constrained via the normalization condition $|p|^2 + |q|^2 = 1$. Through the diagonalization of $\boldsymbol{H}$, their ratio is fixed to

$$\frac{p}{q} = \sqrt{\frac{M_{12}^* - {}^i\!/\!{}_2\Gamma_{12}^*}{M_{12} - {}^i\!/\!{}_2\Gamma_{12}}} = \frac{\Delta m - {}^i\!/\!{}_2\Delta\Gamma}{2(M_{12} - {}^i\!/\!{}_2\Gamma_{12})}. \tag{1.22}$$

1.2.2 Decays of Neutral Mesons

They decay of the flavour eigenstates P^0 and $\bar{P}^0$ into a certain final state $|f\rangle$ or its $\mathcal{CP}$-conjugate state $|\bar{f}\rangle$ can be expressed by the decay amplitudes

$$\begin{aligned} A_f &= \langle f|H|P^0\rangle, & A_{\bar{f}} &= \langle \bar{f}|H|P^0\rangle, \\ \bar{A}_f &= \langle f|H|\bar{P}^0\rangle, & \bar{A}_{\bar{f}} &= \langle \bar{f}|H|\bar{P}^0\rangle, \end{aligned} \tag{1.23}$$

---

[4] For the $K^0 - \bar{K}^0$ system, a different naming scheme is applied. Here, the lifetimes of the two eigenstates are the distinguishing characteristic and therefore used as a label, see Section 1.2.5.

all mediated by the weak interaction Hamiltonian H. The $\mathcal{CP}$ transformation interchanges P^0 and $\bar{P}^0$. Choosing $(\mathcal{CP})^2 = 1$, it follows

$$\mathcal{CP}|\,P^0\,\rangle = \mathrm{e}^{+i\xi_{P^0}}|\,\bar{P}^0\,\rangle, \qquad \mathcal{CP}|\,\bar{P}^0\,\rangle = \mathrm{e}^{-i\xi_{P^0}}|\,P^0\,\rangle \tag{1.24}$$

$$\mathcal{CP}|f\rangle = \mathrm{e}^{+i\xi_f}|\bar{f}\,\rangle, \qquad \mathcal{CP}|\bar{f}\,\rangle = \mathrm{e}^{-i\xi_f}|f\rangle. \tag{1.25}$$

The phases ξ_{P^0} and ξ_f depend on flavour content and parity of the wave functions.

1.2.3 Time Evolution Formalism

The evolution over time of the neutral meson mass eigenstates follow an exponential evolution:

$$|\,P_H(t)\,\rangle = \mathrm{e}^{-i\mu_H t}|\,P_H\,\rangle = \mathrm{e}^{-im_H t}\mathrm{e}^{-\frac{\Gamma_H}{2}t}|\,P_H\,\rangle, \tag{1.26}$$

$$|\,P_L(t)\,\rangle = \mathrm{e}^{-i\mu_L t}|\,P_L\,\rangle = \mathrm{e}^{-im_L t}\mathrm{e}^{-\frac{\Gamma_L}{2}t}|\,P_L\,\rangle. \tag{1.27}$$

Taking into account Eq. (1.21) and Eq. (1.27), the time evolution of an initial flavour eigenstate P^0 or $\bar{P}^0$ follows as

$$|\,P^0(t)\,\rangle = g_+(t)|\,P^0\,\rangle - \frac{q}{p}g_-(t)|\,\bar{P}^0\,\rangle, \tag{1.28}$$

$$|\,\bar{P}^0(t)\,\rangle = g_+(t)|\,\bar{P}^0\,\rangle - \frac{p}{q}g_-(t)|\,P^0\,\rangle, \tag{1.29}$$

where

$$g_\pm(t) = \frac{1}{2}\left(\mathrm{e}^{-i\mu_H t} \pm \mathrm{e}^{-i\mu_L t}\right) = \frac{1}{2}\left(\mathrm{e}^{-im_H t - \frac{\Gamma_H}{2}} \pm \mathrm{e}^{-im_L t - \frac{\Gamma_L}{2}}\right). \tag{1.30}$$

For studies $\mathcal{CP}$ violation, see Section 1.2.4, in decay processes with a final state f and its $\mathcal{CP}$-conjugate $\bar{f}$, the decay rates

$$\begin{aligned} \Gamma(P^0(t)\to f) &= |\langle f\,|\,H\,|\,P^0(t)\,\rangle|^2, & \Gamma(P^0(t)\to \bar{f}) &= |\langle \bar{f}\,|\,H\,|\,P^0(t)\,\rangle|^2, \\ \Gamma(\bar{P}^0(t)\to f) &= |\langle f\,|\,H\,|\,\bar{P}^0(t)\,\rangle|^2, & \Gamma(\bar{P}^0(t)\to \bar{f}) &= |\langle \bar{f}\,|\,H\,|\,\bar{P}^0(t)\,\rangle|^2, \end{aligned} \tag{1.31}$$

are interesting observables to measure experimentally. When further defining the complex parameters

$$\lambda_f = \frac{1}{\bar{\lambda}_f} = \frac{q}{p}\frac{\bar{A}_f}{A_f} \quad \text{and} \quad \bar{\lambda}_{\bar{f}} = \frac{1}{\lambda_{\bar{f}}} = \frac{q}{p}\frac{A_{\bar{f}}}{\bar{A}_{\bar{f}}} \tag{1.32}$$

these decay rates can be written as

$$
\begin{aligned}
\Gamma(P^0(t)\to f) &= \quad |A_f|^2\Big[|g_+(t)|^2 + |\lambda_f|^2|g_-(t)|^2 + 2\,\mathcal{R}e\left(\lambda_f g_+^*(t) g_-(t)\right)\Big],\\
\Gamma(P^0(t)\to \bar{f}) &= |\bar{A}_{\bar{f}}|^2\left|\frac{q}{p}\right|^2\Big[|g_-(t)|^2 + |\bar{\lambda}_{\bar{f}}|^2|g_+(t)|^2 + 2\,\mathcal{R}e\left(\bar{\lambda}_{\bar{f}} g_+(t) g_-^*(t)\right)\Big],\\
\Gamma(\bar{P}^0(t)\to f) &= |A_f|^2\left|\frac{p}{q}\right|^2\Big[|g_-(t)|^2 + |\lambda_f|^2|g_+(t)|^2 + 2\,\mathcal{R}e\left(\lambda_f g_+(t) g_-^*(t)\right)\Big],\\
\Gamma(\bar{P}^0(t)\to \bar{f}) &= \quad |\bar{A}_{\bar{f}}|^2\Big[|g_+(t)|^2 + |\bar{\lambda}_{\bar{f}}|^2|g_-(t)|^2 + 2\,\mathcal{R}e\left(\bar{\lambda}_{\bar{f}} g_+^*(t) g_-(t)\right)\Big],
\end{aligned}
\tag{1.33}
$$

where, with Eq. (1.30) in mind,

$$
|g_\pm(t)|^2 = \frac{\mathrm{e}^{-\Gamma t}}{2}\Big[\cosh\left(\frac{\Delta\Gamma t}{2}\right) \pm \cos(\Delta m t)\Big], \tag{1.34}
$$

$$
g_\pm^*(t) g_\mp(t) = \mp\frac{\mathrm{e}^{-\Gamma t}}{2}\Big[\sinh\left(\frac{\Delta\Gamma t}{2}\right) + i\sin(\Delta m t)\Big]. \tag{1.35}
$$

With the introduction of the derived $\mathcal{CP}$ observables

$$
D_f = \frac{2\mathcal{R}e(\lambda_f)}{1+|\lambda_f|^2}, \qquad C_f = \frac{1-|\lambda_f|^2}{1+|\lambda_f|^2}, \qquad S_f = \frac{2\mathcal{I}m(\lambda_f)}{1+|\lambda_f|^2}, \tag{1.36}
$$

$$
D_{\bar{f}} = \frac{2\mathcal{R}e(\bar{\lambda}_{\bar{f}})}{1+|\bar{\lambda}_{\bar{f}}|^2}, \qquad C_{\bar{f}} = \frac{1-|\bar{\lambda}_{\bar{f}}|^2}{1+|\bar{\lambda}_{\bar{f}}|^2}, \qquad S_{\bar{f}} = \frac{2\mathcal{I}m(\bar{\lambda}_{\bar{f}})}{1+|\bar{\lambda}_{\bar{f}}|^2}, \tag{1.37}
$$

that fulfil the conditions

$$
D_f^2 + C_f^2 + S_f^2 = 1 \quad \text{and} \quad D_{\bar{f}}^2 + C_{\bar{f}}^2 + S_{\bar{f}}^2 = 1, \tag{1.38}
$$

the decay rates can in conclusion be expressed as

$$\begin{aligned}
\frac{\Gamma(P^0(t)\to f)}{\mathrm{e}^{-\Gamma t}} &= \frac{1}{2}|A_f|^2\left(1+|\lambda_f|^2\right) & &\left[\cosh\left(\frac{\Delta\Gamma}{2}t\right)+D_f\sinh\left(\frac{\Delta\Gamma}{2}t\right)\right.\\
& & &\left.+C_f\cos(\Delta m t)-S_f\sin(\Delta m t)\right], \qquad (1.39)\\
\frac{\Gamma(P^0(t)\to \bar{f})}{\mathrm{e}^{-\Gamma t}} &= \frac{1}{2}|\bar{A}_{\bar{f}}|^2\left|\frac{q}{p}\right|^2\left(1+|\bar{\lambda}_{\bar{f}}|^2\right) & &\left[\cosh\left(\frac{\Delta\Gamma}{2}t\right)+D_{\bar{f}}\sinh\left(\frac{\Delta\Gamma}{2}t\right)\right.\\
& & &\left.+C_{\bar{f}}\cos(\Delta m t)-S_{\bar{f}}\sin(\Delta m t)\right], \qquad (1.40)\\
\frac{\Gamma(\bar{P}^0(t)\to f)}{\mathrm{e}^{-\Gamma t}} &= \frac{1}{2}|A_f|^2\left|\frac{p}{q}\right|^2\left(1+|\lambda_f|^2\right) & &\left[\cosh\left(\frac{\Delta\Gamma}{2}t\right)+D_f\sinh\left(\frac{\Delta\Gamma}{2}t\right)\right.\\
& & &\left.-C_f\cos(\Delta m t)+S_f\sin(\Delta m t)\right], \qquad (1.41)\\
\frac{\Gamma(\bar{P}^0(t)\to \bar{f})}{\mathrm{e}^{-\Gamma t}} &= \frac{1}{2}|\bar{A}_{\bar{f}}|^2\left(1+|\bar{\lambda}_{\bar{f}}|^2\right) & &\left[\cosh\left(\frac{\Delta\Gamma}{2}t\right)+D_{\bar{f}}\sinh\left(\frac{\Delta\Gamma}{2}t\right)\right.\\
& & &\left.-C_{\bar{f}}\cos(\Delta m t)+S_{\bar{f}}\sin(\Delta m t)\right], \qquad (1.42)
\end{aligned}$$

which is their most common parametrization.

1.2.4 *CP* Violation in Neutral Meson Systems

Overall, one can distinguish between three different kinds of phases that are involved in transitions amplitudes: The so called *spurious* phases in *CP* transformations, ξ_{P^0} and ξ_f in Eq. (1.25), are global and convention-dependent. As they do not come from any dynamics, they cannot be measured and are set to 0 for convenience. *Strong* phases arise in final-state interactions mediated by the electromagnetic or strong forces. Since they conserve the *CP* symmetry, strong phases are considered *CP* even. On the other hand, *weak* phases originate ultimately from the coupling of $W^{\pm}$ bosons to quarks via the phase in the CKM matrix. As they change sign under *CP* transformation, these phases are considered *CP* odd. In contrast to the spurious phases, the existence of the strong and weak phases is physically motivated but only relative strong and weak phases between different terms of transitions amplitudes are convention-independent. The mixing and decay mechanisms of neutral meson systems shown in the previous sections allow three different types of *CP* violation, depending on the transitions that include weak phases: Violation of the *CP* symmetry in the decay (direct *CP* violation), *CP* violation in the mixing (indirect *CP* violation), and *CP* violation in the interference of decay and decay after mixing. These three manifestations will be further described in the following paragraphs.

Direct *CP* Violation

Direct *CP* violation occurs when the absolute value of the decay amplitude of a meson to a certain final state f deviates from the absolute value of the decay amplitude of the *CP* conjugated process, i.e.:

$$\left|\frac{A_f}{\bar{A}_{\bar{f}}}\right| \neq 1. \tag{1.43}$$

For this to happen, different direct decays with amplitudes A_i, waek phases ϕ_i and strong phases δ_i must interfere. An example with two contributing processes would be

$$\begin{aligned} A_f &= A_1 \mathrm{e}^{i(\delta_1+\phi_1)} + A_2 \mathrm{e}^{i(\delta_2+\phi_2)}, \\ \bar{A}_{\bar{f}} &= A_1 \mathrm{e}^{i(\delta_1-\phi_1)} + A_2 \mathrm{e}^{i(\delta_2-\phi_2)}. \end{aligned} \tag{1.44}$$

In the case that $\delta_1 \neq \delta_2$ and $\phi_1 \neq \phi_2$, one arrives at Eq. (1.43). Thus, the occurrence of direct *CP* violation requires a difference of strong and weak phases between contributing processes.

Indirect *CP* Violation

CP violation in the mixing is defined by unequal mixing rates of a neutral meson and its anti-meson:

$$\Gamma(P^0 \to \bar{P}^0) \neq \Gamma(\bar{P}^0 \to P^0). \tag{1.45}$$

Mixing transition are described by the off-diagonal elements of the effective Hamiltonian in Eq. (1.18) that can be written as

$$M_{12} = |M_{12}|\mathrm{e}^{i\phi_M}, \qquad \Gamma_{12} = |\Gamma_{12}|\mathrm{e}^{i\phi_\Gamma}. \tag{1.46}$$

For unequal mixing rates to occur, it follows that $|\Gamma_{12}/M_{12}| \neq 0$ and $\phi_M - \phi_\Gamma \neq 0$. As a consequence, taking Eq. (1.22) in mind, this leads to:

$$\left|\frac{q}{p}\right| \neq 1. \tag{1.47}$$

CP Violation in the Interference of Decay and Decay after Mixing

Lastly, *CP* violation can occur if a meson and its anti-particle have common final state f. In this case, the decay amplitudes of the direct decay, $P^0 \to f$, and the decay after mixing, $P^0 \to \bar{P}^0 \to f$, can interfere and cause a $\mathcal{CP}$ violation

$$\mathcal{Im}(\lambda_f) \neq 0, \tag{1.48}$$

which is even possible without the presence of direct or indirect $\mathcal{CP}$ violation, as becomes apparent from Eq. (1.32).

1.2.5 Neutral Kaons

Together with the charged kaons $K^{\pm}$, the pions $\pi^{\pm}$ and π^0, and the η, the two neutral kaons K^0 and $\bar{K}^0$ form the octet of light spin-0 mesons with negative parity. In the valence quark model $|K^0\rangle = |\bar{s}d\rangle$, $|\bar{K}^0\rangle = |s\bar{d}\rangle$, which makes the kaons strange particles with a strangeness of $+1$ for the K^0 and -1 for $\bar{K}^0$.

In contrast to other neutral meson systems, the mixing eigenstates of the neutral kaon system have very different lifetimes. Therefore, these eigenstates are labelled by their lifetimes, instead of their masses: K^0_S is the short-lived neutral kaon while K^0_L is the long-lived neutral kaon. The differences of their masses and decay widths are defined as

$$\Delta m = m_L - m_S, \qquad \Delta\Gamma = \Gamma_L - \Gamma_S, \tag{1.49}$$

with

$$\mu_S = m_S - {}^{i}\!/\!_{2}\Gamma_S \quad \text{and} \quad \mu_L = m_L - {}^{i}\!/\!_{2}\Gamma_L, \tag{1.50}$$

analogous to Eqs. (1.19) to (1.20). Measurements [20] have shown that

$$\begin{aligned} \tau_L &= \frac{1}{\Gamma_L} = (5.116 \pm 0.021) \cdot 10^{-8}\,\mathrm{s}, \\ \tau_S &= \frac{1}{\Gamma_S} = (0.8954 \pm 0.0004) \cdot 10^{-10}\,\mathrm{s}, \end{aligned}$$

and

$$\Delta m = (0.5293 \pm 0.0009) \cdot 10^{10}\,\hbar\mathrm{s}^{-1} = (3.4839 \pm 0.0059) \cdot 10^{-22}\ \mathrm{MeV}$$

Since K^0_L is heavier than K^0_S, the mass eigenstates are written analogous to Eq. (1.21):

$$|K^0_\mathrm{L}\rangle = p_K|K^0\rangle + q_K|\bar{K}^0\rangle, \qquad |K^0_\mathrm{S}\rangle = p_K|K^0\rangle - q_K|\bar{K}^0\rangle. \tag{1.51}$$

In the case of a $\mathcal{CP}$ invariance and that $|\bar{K}^0\rangle$ is defined as $\mathcal{CP}|K^0\rangle$, $q_K = p_K$ applies and therefore K^0_S would be the $\mathcal{CP}$ even and K^0_L the $\mathcal{CP}$ odd state. But direct $\mathcal{CP}$ violation, e.g. in the decay $K^0 \to \pi\pi$, and indirect $\mathcal{CP}$ violation were both measured in the $K^0 - \bar{K}^0$

system [20]. The CP violation in $K^0 - \bar{K}^0$ mixing is given by the parameter $\tilde{\epsilon}$ [20, 40] where, following Eq. (1.47),

$$\frac{p_K}{q_K} = \frac{1+\tilde{\epsilon}}{1-\tilde{\epsilon}}. \tag{1.52}$$

As a consequence, K^0_S and K^0_L are mixtures of the CP eigenstates K_1 and K_2:

$$|K^0_\mathrm{S}\rangle = \tfrac{1}{\sqrt{1+|\tilde{\epsilon}|^2}}\left(|K_1\rangle + \tilde{\epsilon}|K_2\rangle\right), \tag{1.53}$$

$$|K^0_\mathrm{L}\rangle = \tfrac{1}{\sqrt{1+|\tilde{\epsilon}|^2}}\left(|K_2\rangle + \tilde{\epsilon}|K_1\rangle\right) \tag{1.54}$$

with

$$|K_1\rangle = \tfrac{1}{\sqrt{2}}\left(|K^0\rangle - |\bar{K}^0\rangle\right), \qquad |K_2\rangle = \tfrac{1}{\sqrt{2}}\left(|K^0\rangle + |\bar{K}^0\rangle\right) \tag{1.55}$$

and

$$CP|K_1\rangle = |K_1\rangle, \qquad CP|K_2\rangle = -|K_2\rangle. \tag{1.56}$$

Under certain assumptions and phase conventions [20, 40], $\tilde{\epsilon} = \epsilon$ applies, which has been measured [20] to be

$$|\epsilon| = (2.228 \pm 0.011) \cdot 10^{-3}$$

1.3 The Decays $B \to \phi K^0_\mathrm{S}$ and $B^0_s \to K^0_\mathrm{S} K^0_\mathrm{S}$

This analysis aims to measure the branching ratio of the rare decay $B^0_s \to K^0_\mathrm{S} K^0_\mathrm{S}$ relative to the the branching ratio of $B^0 \to \phi K^0_\mathrm{S}$ — with the final states $K^0_\mathrm{S} \to \pi^+\pi^-$ and $\phi \to K^+K^-$— as a preparation for future CP violation measurements in these channels. Since both decays have purely hadronic final states they are in general challenging to analyse in a hadronic collider such as the LHC. However, they contain interesting CP observables, which makes it worth the effort.

This section aims to give a qualitative overview of the two decays, their decay amplitudes and the resulting CP observables, the physical properties of the decay components, and their experimental status.

1.3.1 Decay Topology of Flavour Changing Neutral Currents

Both decays comprise a change of quark flavour without changing its electric charge, which is referred to as a *flavour changing neutral current* (FCNC) process. This kind of transition is called a flavour changing neutral current, which in the SM can only occur on loop-level. Besides so called box diagrams, which portray the mixing of neutral mesons, Feynman diagrams containing loops are so called *penguin diagrams*. The amplitudes of the investigated decays are dominated by gluonic penguin diagrams, as shown in Fig. 1.3. Gluonic penguins have a single loop, mediating the quark transitions $\overline{b} \to \overline{s} q' \overline{q}'$ transition involving a $W^{\pm}$ boson and a gluon. For $B^0 \to \phi K^0_S$, the quark-anti-quark pair $q'\overline{q}'$ is $s\overline{s}$, while it is $d\overline{d}$ for $B^0_s \to K^0_S K^0_S$.

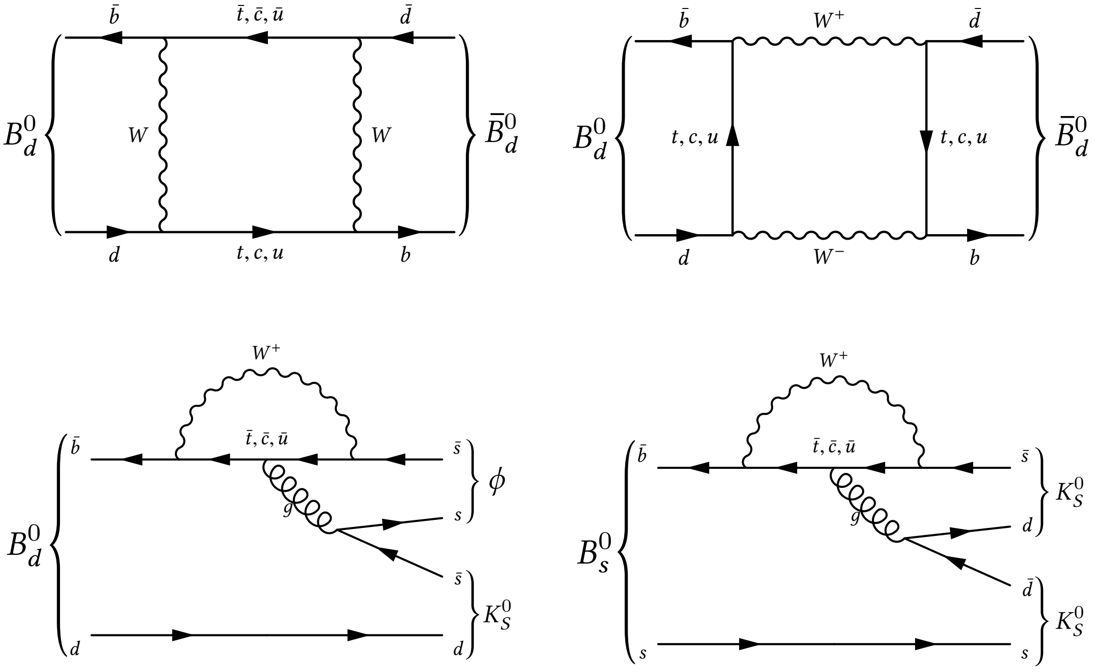

$B^0 \to \phi K^0_S$ $\qquad$ $B^0_s \to K^0_S K^0_S$

Figure 1.3 – Top: Feynman *box* diagrams for the $B^0 - \overline{B}^0$ mixing. The Feynman diagram for the $B^0_s - \overline{B}^0_s$ mixing can be obtained by interchanging the d ($\overline{d}$) for a s ($\overline{s}$) in the initial (final) state.
Bottom: Leading order Feynman diagrams for the dominating decay amplitudes contributions of (c) $B^0 \to \phi K^0_S$ and (d) $B^0_s \to K^0_S K^0_S$.

In order to calculate the corresponding decay amplitudes, FCNC processes are often parametrized in terms of an effective Hamiltonian [17, 41–43]

$$\mathcal{H}_{\text{eff}} = \frac{G_F}{\sqrt{2}} \sum_{\alpha} \lambda^q_\alpha C_\alpha(\mu) Q_\alpha(\mu), \tag{1.57}$$

with the Fermi constant G_F, the local operators Q_α, and the *Wilson coefficients* C_α [41, 44]. Together with the CKM factors λ^q_α, which are defined as

$$\lambda^q_\alpha \equiv V^*_{\alpha b} V_{\alpha q'} \quad \text{with} \quad q = s \quad \text{for} \quad \overline{b} \to \overline{s} q' \overline{q}' \tag{1.58}$$

the C_α determine the weight with which each operator Q_α is entering the sum in Eq. (1.57) and therefore are often interpreted as the "short distance effects". The amplitude for the decay $B_q \to f_{CP}$ with the final state $f_{CP} = \phi K^0_S, K^0_S K^0_S$ and therefore comprising a $\bar{b} \to \bar{s}$ transition is then given as

$$A(B_q \to f_{CP}) = \langle f_{CP} | \mathcal{H}_{\mathrm{eff}} | B_q \rangle = \frac{G_F}{\sqrt{2}} \sum_\alpha \lambda^s_\alpha C_\alpha(\mu) \langle f_{CP} | Q_\alpha(\mu) | B_q \rangle, \tag{1.59}$$

with the transition matrix elements $\langle f_{CP} | Q_\alpha(\mu) | B_q \rangle$ between B_q and its final state f_{CP}, which is evaluated at the renormalization scale μ. This free scale separates the short distance (C_α) from the long distance effects, contained in the operators Q_α [43]. Therefore, contributions from heavy particles with a mass $m > \mu$, such as t, $W^\pm$, and Z^0, are included in C_α and moreover also contributions from possible heavy particles beyond the SM. Since it is possible to calculate the Wilson coefficients from theory, this approach — referred to as *Operator Product Expansion* [41] — enables the search for physics beyond the SM.

In general, the operators Q_α correspond to the Feynman diagrams contributing to the total decay amplitude. The amplitudes of both decays investigated here are proportional to the sum of the penguin amplitudes

$$A_{f_{CP}} \propto \lambda^s_t P_t + \lambda^s_c P_c + \lambda^s_u P_u \tag{1.60}$$

one for each internal quark t, c, and u, with the CKM factors λ^s_α defined in Eq. (1.58). Because of the unitarity of the CKM matrix, Eq. (1.60) can be rewritten in one of the following forms

$$\begin{aligned} \lambda^s_t P_t + \lambda^s_c P_c + \lambda^s_u P_u &= \lambda^s_t (P_{tu}) + \lambda^s_c (P_{cu}) \\ &= \lambda^s_t (P_{tc}) + \lambda^s_u (P_{uc}) \\ &= \lambda^s_c (P_{ct}) + \lambda^s_u (P_{ut}) \end{aligned} \tag{1.61}$$

with

$$P_{\alpha\beta} \equiv P_\alpha - P_\beta. \tag{1.62}$$

Decay Observables of $B^0_s \to K^0_S K^0_S$

The decay $B^0_s \to K^0_S K^0_S$ is a pure $\bar{b} \to \bar{s} d \bar{d}$ penguin decay, whose amplitude comprises contributions from the gluonic penguin diagram, shown in Fig. 1.3d, and electroweak penguin diagrams [45, 46], where the gluon is exchanged by a Z^0 or a γ, coupling to the loop, i.e. either to the loop quark or the $W^\pm$. When taking advantage of the CKM unitarity, while explicitly writing out the weak-phase dependence and absorbing *CP*-conserving strong phases in P, one can rewrite Eq. (1.60) with Eqs. (1.61) to (1.62) as [46]

$$A_{K^0_S K^0_S} = |\lambda^s_u| \, e^{i\gamma} P_{uc} - |\lambda^s_t| \, P_{tc} \tag{1.63}$$

with a weak phase γ. From this amplitude, with Eq. (1.32) and Eq. (1.47) in mind, one can deduce the two observables [46]

$$\begin{aligned} \mathcal{B} &\propto \tfrac{1}{2}\left(\left|A_{K^0_S K^0_S}\right|^2 + \left|\bar{A}_{K^0_S K^0_S}\right|^2\right), \\ S_{B^0_s \to K^0_S K^0_S} \propto \mathcal{Im}\left(\lambda_{K^0_S K^0_S}\right) &= \mathcal{Im}\left(e^{-2i\beta_s} \frac{\bar{A}_{K^0_S K^0_S}}{A_{K^0_S K^0_S}}\right) \end{aligned} \tag{1.64}$$

the branching ratio $\mathcal{B}$ and the interference $\mathcal{CP}$ violation asymmetry $S_{B^0_s \to K^0_S K^0_S}$, with the $\mathcal{CP}$-conjugate amplitude $\bar{A}_{K^0_S K^0_S}$ for the decay $\bar{B}^0_s \to K^0_S K^0_S$ and the mixing angle β_s, as defined in Eq. (1.15). The angle β_s only contains CKM matrix elements that are only complex in higher orders of the Wolfenstein parametrization, see Eq. (1.7), and furthermore it can be assumed that $\beta_s \approx 0$ in the SM [45]. Under the assumption that contributions from $\lambda^s_u P_{uc}$ are negligible and taking into account that $\beta_s \approx 0$, it follows that $\lambda_{K^0_S K^0_S} = 1$. Therefore it is expected that $S_{B^0_s \to K^0_S K^0_S} = 0$ [45]. Hence, the measurement of $\mathcal{CP}$ violation in the decay $B^0_s \to K^0_S K^0_S$ would be a null test of the SM, e.g. like the measurement of $\mathcal{CP}$ violation in $B^0_s \to \phi\phi$ [47], but with the important prerequisite to understand and account for corrections coming from the neglect of P_{uc}. One possible solution for this problem would be to also measure the same observables in the U-spin symmetric decay $B^0 \to K^0_S K^0_S$, where the corresponding CKM factors are in the same order of magnitude, which allows for a precise measurement of the contribution from P_{uc}. This is explained in detail in Ref. [45].

Since the branching ratios of $B^0_s \to K^0_S K^0_S$ and $B^0 \to K^0_S K^0_S$ are in the order of $\mathcal{O}(10^{-5})$ and $\mathcal{O}(10^{-6})$ [20], respectively, and the reconstruction of a fully hadronic final state is challenging at a hadronic collider such as LHC, this analysis does not perform the above mentioned null test of the SM. Instead, it focusses on the search of the decay $B^0_s \to K^0_S K^0_S$ with the LHCb experiment as a preparation for future measurements and further aims at a measurement of the branching ratio relative to the branching ratio of a normalisation channel, the decay $B^0 \to \phi K^0_S$.

Decay Observables of $B \to \phi K^0_S$

Even though the decay $B^0 \to \phi K^0_S$ is not the main topic of the physic analysis presented in this thesis, its importance for the examination of *CP* violation shall be discussed shortly in this paragraph.
Just like the decay $B^0_s \to K^0_S K^0_S$, $B^0 \to \phi K^0_S$ is a pure penguin decay with a $\bar{b} \to \bar{s}s\bar{s}$ transition. Its amplitude contains in general contributions from the gluonic penguin diagram, shown in Fig. 1.3c, but also electroweak penguin diagrams.
Following Eq. (1.60) and Eqs. (1.61) to (1.62) the decay amplitude can be written as [48]

$$A_{\phi K^0_S} = \lambda^s_u P_{ut} + \lambda^s_c P_{ct} \tag{1.65}$$

Now, considering that a common final state is reached via $K^0 - \bar{K}^0$ mixing, the Interference *CP* violation observable is given as [48]

$$\begin{aligned}\lambda_f &= \frac{q}{p}\frac{\bar{A}_{\bar{f}}}{A_f} = \frac{q_B}{p_B}\frac{q_K}{p_K}\frac{\bar{A}_{\bar{f}}}{A_f} \\ &\approx \frac{V^*_{tb}V_{td}}{V_{tb}V^*_{ts}}\frac{V^*_{cd}V_{cs}}{V_{cd}V^*_{cs}}\frac{\bar{A}_{\bar{f}}}{A_f} \approx \frac{V_{td}}{V^*_{td}}\frac{A\left(\bar{B}^0 \to \phi\bar{K}^0\right)}{A\left(B^0 \to \phi K^0\right)}\end{aligned} \tag{1.66}$$

when omitting terms $> \mathcal{O}(\lambda^4)$ in the Wolfenstein parametrization (see Eq. (1.7), Page 8). With *CP* transformation, $A\left(B^0 \to \phi K^0\right) = -A\left(\bar{B}^0 \to \phi\bar{K}^0\right)$ with $\lambda^s_\alpha \to \lambda^{s\,*}_\alpha$. Therefore, the ratio $\bar{A}/A$ can be written as

$$\frac{\bar{A}_{\bar{f}}}{A_f} \approx \eta_f \tag{1.67}$$

when neglecting contributions from λ^s_u in Eq. (1.65). Subsequently

$$\begin{aligned}\lambda_f &\approx \eta_f \frac{V_{td}}{V^*_{td}} = \eta_f \mathrm{e}^{-i2\beta} \\ &\Rightarrow -\eta_f S_f \approx \sin 2\beta\end{aligned} \tag{1.68}$$

where $\eta_f = -1$ for $B^0 \to \phi K^0_S$, using the definition of S_f in Eq. (1.37). The angle β has been already measured to a great success by the LHCb experiment in multiple modes, e.g. in the "gold-plated" channel for β, $B^0 \to J/\psi K^0_S$ [49, 50]. The current world average, including the latest measurement from the LHCb experiment is [20]:

$$\sin 2\beta = 0.699 \pm 0.017\,.$$

In the SM, corrections to the value of S_f in $B^0 \to \phi K^0_S$, which are defined as $\Delta S_{\phi K^0_S} \equiv -\eta_{\phi K^0_S} S_{\phi K^0_S} - \sin 2\beta$, are mostly dictated by the size of P_{ut}/P_{ct}, i.e. the contribution of

λ^s_u to the decay amplitude. Examples for this contribution are additional amplitudes from $b \to u$ tree diagrams, loop diagrams with u quark contributions, and final-state interactions [51]. These corrections are expected to be in the range of 0.01 to 0.05 [48, 52]. The experimental comparison between the interference *CP* violation asymmetries in $B^0 \to J/\psi K^0_S$, and $B^0 \to \phi K^0_S$ is an interesting probe for physics beyond the SM, since the FCNC process of $B^0 \to \phi K^0_S$ may be sensitive to possible new physics contributions in the loop, thus enhancing the measured $S_{\phi K^0_S}$ in this decay. Here, the current world average from measurements by the Belle and BaBar experiments amounts to [20]

$$S_{\phi K^0_S} = 0.59 \pm 0.14\,.$$

Since it is still dominated by its statistical uncertainty, future measurements by the LHCb and Belle 2 experiments will help to reveal a possible tension.
However, the measurement of $S_{\phi K^0_S}$ is challenged by the alternative final state $K^+K^-K^0_S$, which is not a *CP* eigenstate. The $K^+K^-K^0_S$ system is *CP* odd (even) if the K^+K^- system has an odd (even) angular momentum. Hence, a measurement of $S_{\phi K^0_S}$ must account for the inference with $B^0 \to K^+K^-K^0_S$ decays, which are mostly S-wave states, see Section 4.3.2.

1.3.2 Properties and Experimental Status of $B^0_s \to K^0_S K^0_S$

The reconstruction and thus any kind of measurements in the decay $B^0_s \to K^0_S K^0_S$ is complicated by its small branching fraction and experimental challenges. The latter is first and foremost the decay topology of a neutral mother particle, B^0_s, decaying into two long-lived neutral particles, K^0_S, which in turn have purely hadronic final states, with $K^0_S \to \pi^+\pi^-$, as depicted in Fig. 1.4. This decay topology, together with the longer flight distance of the K^0_S meson compared to e.g. the B^0_s meson impedes the reduction of combinatoric background on the one side, but also the reconstruction of the B^0_s decay vertex and thus, among other things, its decay time, which is crucial for a time-dependent measurement of of the decay rate, in order to measure the *CP* observable S_f.

The first and only measurement in the decay $B^0_s \to K^0_S K^0_S$ is the measurement of the branching fraction $\mathcal{B}(B^0_s \to K^0\bar{K}^0)$ that has been accomplished in 2015 by the Belle experiment [53, 54]. Here, the branching ratio was measured to

$$\mathcal{B}(B^0_s \to K^0\bar{K}^0) = \left(19.6^{+5.8}_{-5.1}\,(\text{stat}) \pm 1.0\,(\text{syst}) \pm 2.0\,\left(N_{B^0_s\bar{B}^0_s}\right)\right) \cdot 10^{-6}.$$

This measurement is compatible with theory predictions from different theoretical models that are all in the order of $20 \cdot 10^{-6}$, see Table 1.1.
The analysis conducted in the course of this thesis performed a search for the decay $B^0_s \to K^0_S K^0_S$ with the LHCb experiment and furthermore aims to measure $\mathcal{B}(B^0_s \to K^0_S K^0_S)/\mathcal{B}(B^0 \to \phi K^0_S)$ in order to contribute to a more precise world average and

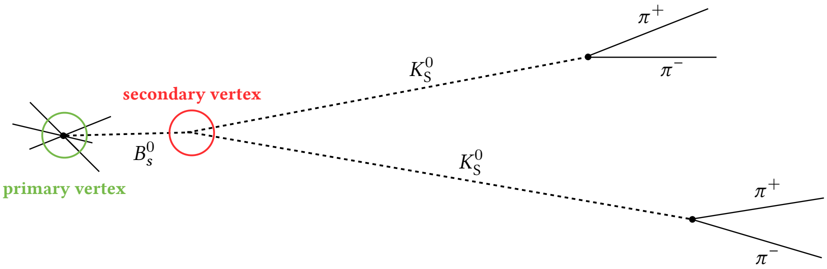

Figure 1.4 – Schematic depiction of the $B^0_s \to K^0_S K^0_S$ decay topology. It represents the decay of a neutral mother particle, B^0_s, decaying into two long-lived neutral particles, K^0_S. These have in turn purely hadronic final states, with $K^0_S \to \pi^+\pi^-$. Therefore, the background reduction and decay time reconstruction are experimentally challenging, especially in the hadronic environment of the LHC.

pave the way for future measurements of $C\!P$ violation in these decay channels. The measurement itself is further discussed in Chapter 6, with preparatory studies of $B^0 \to \phi K^0_S$ and $B^0_s \to K^0_S K^0_S$ outlined in Chapter 4 and Chapter 5, respectively.

Table 1.1 – Theory predictions for the branching ratio of the decay $B^0_s \to K^0\overline{K}^0$ [55]. The theoretical models are QCD factorization (QCDF) [56], soft-collinear effective theory (SCET) [57] and perturbative QCD (pQCD) [55]. The errors the predictions correspond to the uncertainties in the input hadronic quantities, from the scale dependence, and the CKM matrix elements, respectively, and are further explained in the corresponding references [55–57].

Model	Prediction (in 10^{-6})
QCDF	$24.7^{+2.5+13.7+2.6+25.6}_{-2.4-9.2-2.9-9.8}$
SCET	$17.7 \pm 6.6 \pm 0.5 \pm 0.6$
pQCD	$15.6^{+5.0+8.3+0.0}_{-3.8-4.7-0.0}$

2 The LHCb Experiment at the Large Hadron Collider

The *Large Hadron Collider beauty* (LHCb) experiment is one of the four main experiments at the LHC operated by the *European Organization for Nuclear Research* (CERN). While the two larger experiments, ATLAS and CMS are designed as *general-purpose detector* (GPD) performing direct searches for physics beyond the SM (New Physics) effects, LHCb is probing the SM with indirect searches, i.e. through high precision measurements of b and c hadron decays. This includes measurements of possibly $\mathcal{CP}$ violating decays or the search for rare decay modes of b and c hadrons. Here, even small contributions from new physics effects may alter the results and lead to deviations from the SM expectations, as explained in Section 1.3 on Page 18.
In order to succeed with its physics programme, the LHCb experiment requires a large sample of b and c hadrons, which are produced in proton-proton (pp) collisions of the LHC, as well as detector components that are able to reconstruct the decay chains of said hadrons with a high precision and furthermore can differentiate between various final state particles, especially pions and kaons.

This chapter starts with a short introduction of the LHC and its four main experiments. The main part however is dedicated to the description of the LHCb experiment and its detector components and furthermore the data processing with the trigger stages and the software framework. The chapter closes with an outlook to the upcoming upgrade of the LHCb experiment.

2.1 The Large Hadron Collider

The Large Hadron Collider is to date not only the largest man-made particle accelerator and collider of the world, but also operates at the highest beam and centre-of-mass energies [58]. The LHC is a circular collider with a circumference of approximately 26 km and is located in a tunnel 50 to 175 m below ground at the France-Switzerland border near the Swiss city of Geneva. At four designated interaction points, the two opposite circling proton beams are brought to collisions at centre-of-mass energies of up to $\sqrt{s} = 14$ TeV, where the four main experiments, mentioned before, are measuring the proton-proton collisions' outcome. In contrast to its predecessor, the Large Electron–Positron Collider, proton beams were chosen for the LHC to allow for a broad range of possible measurements with a wide energy spectrum and at the same time minimising synchrotron losses. The disadvantage of proton beams is the hadronic nature of the collisions, leading to a large number of particles, which can be challenging, especially for purely hadronic decay chains like $B \to K_S^0 K_S^0$ with $K_S^0 \to \pi^+\pi^-$ (see Section 1.3.2, Page 23).

2.1.1 LHC Accelerator Complex and Collider

The particle acceleration in the LHC depends on an array of pre-accelerators, as shown in Fig. 2.1: After splitting the protons from Hydrogen atoms, stored in a gas bottle, they are injected to the *Linear Accelerator 2* (LINAC2). From here, they are subsequently accelerated by the *Proton Synchrotron Booster* (BOOSTER), the *Proton Synchrotron* (PS), and the *Super Proton Synchrotron* (SPS) before being injected at an energy of 450 GeV to the LHC via the two transfer lines TI2 and TI8. The proton beams are distributed in so called bunch trains, where each bunch train consists of four batches of 72 bunches with a bunch spacing of 25 ns and an intensity of $1.15 \cdot 10^{11}$ protons. After reaching a total number of up to 2808 bunches in each proton beam in the LHC, they are further accelerated to a beam energy of 7 TeV. At the four interaction points, they are brought to collisions at a design luminosity of up to $10^{34}\,\mathrm{cm}^{-2}\,\mathrm{s}^{-1}$ with a rate of 40 MHz. Superconducting NbTi magnets, which are cooled to 1.9 K with superfluid helium, keep the beams on course and a system of superconducting radio-frequency cavities accelerates and contains the bunches.

In the course of its first running period (Run I) from 2010–2012 LHC delivered *pp* collisions at a reduced centre-of-mass energy of $\sqrt{s} = 7$ TeV (2010/11) and $\sqrt{s} = 8$ TeV (2012) with a higher bunch spacing of 50 ns, after recovering from serious damage to the cooling infrastructure and several magnets, caused by a fault in the electrical connection between two magnets [59]. In the second running period (Run II), 2015–2018, LHC was able to deliver the design luminosity by increasing the centre-of-mass energy to $\sqrt{s} = 13$ TeV with a smaller bunch crossing rate of 25 ns. The measurement of the $B_s^0 \to K_S^0 K_S^0$ branching ratio is based on data recorded during Run I and the first half of Run II (2015 & 2016).

2.1.2 The LHC Experiments

Together with LHCb, seven experiments are located at the four interaction regions of the LHC: LHCb and the other three main experiments, located at the four interaction points and three smaller experiments, located in the direct vicinity of a interaction point.

The two *general-purpose detector*s (GPDs) ATLAS (‘A Toroidal LHC Apparatus’) [61] and CMS (‘Compact Muon Solenoid’) [62] are located at opposite interaction points of the collider. They are most famous for the joint discovery of the last missing SM particle, the Higgs boson [22, 63, 64]. In general, they target a wide range of research

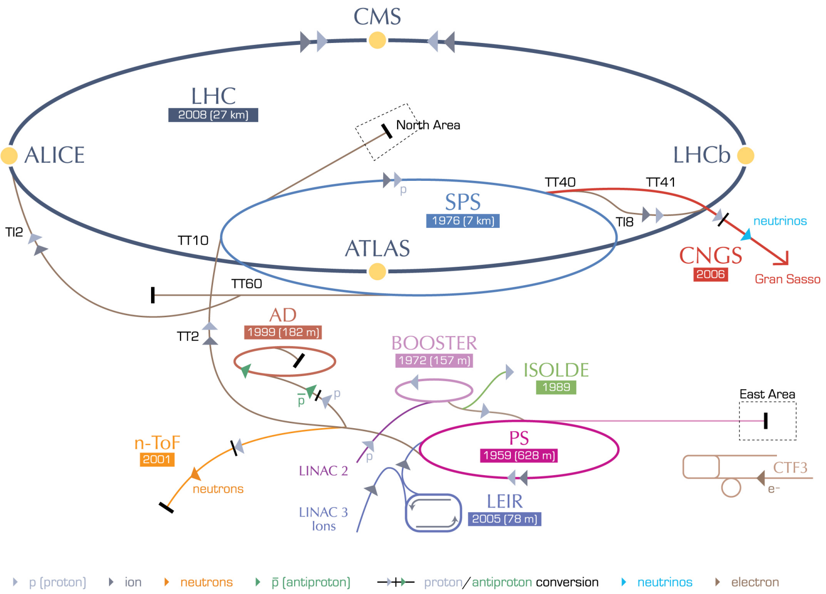

Figure 2.1 – Schematic overview of CERN's accelerator complex [60]. The pre-accelerator chain for the proton-proton collision mode consists of the Linear Accelerator 2, the Proton Synchrotron Booster, the *Proton Synchrotron* (PS), and the *Super Proton Synchrotron* (SPS). For the ion-ion collision mode, the LINAC2 and the *Proton Synchrotron Booster* (BOOSTER) are substituted by LINAC3 and the *Low Energy Ion Ring* (LEIR). Other CERN machines that use parts of the *Large Hadron Collider* (LHC) accelerator complex are the *Antiproton Decelerator* (AD), the *CERN Neutrinos for Gran Sasso* (CNGS), the *Isotope Separator Online Device* (ISOLDE), and the *Neutrons Time of Flight* (n-ToF).

topics about direct searches for physics beyond the SM, i.e. the search for dark matter, extra dimensions and super-symmetric partners of the SM particles.

The fourth main experiment, ALICE ('A Large Ion Collider Experiment') [65], mainly analyses data taken from Pb-Pb or Pb-p collisions, to investigate the properties and phase transitions of the so called quark-gluon plasma, a state of strongly interacting particles forming at a state of high temperatures and densities.

The physics program of TOTEM ('Total Elastic and Diffractive Cross Section Measurement') [66] is encoded in its name: the second smallest LHC experiment is committed to the measurement of the pp cross section and investigates the proton structure. Its detectors are located on both sides of the CMS detector.

The smallest LHC experiment, LHCf (Large Hadron Collider forward) [67], uses the ATLAS interaction point and looks at particles produced in the extreme forward region of collisions, especially pions, in order to improve the understanding of cosmic rays.

MoEDAL ('Monopole and Exotics Detector at the LHC') [68], whose passive nuclear-track detectors are installed around the LHCb interaction point, is dedicated to the search for magnetic monopoles, hypothetical particles with a magnetic charge. Its physics programme is expanded with the search for highly ionizing stable massive

particles that are predicted by some beyond SM theories.
The last and not yet further explained LHC experiment, LHCb, will be described in detail in Section 2.2.

2.1.3 Production of Beauty Hadrons at the LHC

Due to its unprecedented centre-of-mass energies and collision rates, the LHC can among other things be considered as a high-yield b hadron factory. Table 2.1 shows the measured production cross section for $b\bar{b}$ quark pairs

$$\sigma_{b\bar{b}} = \sigma(pp \to b\bar{b}X)$$

for the years 2011, 2012, 2015, and 2016.

Table 2.1 – Production cross sections for $b\bar{b}$ quark pairs from pp collisions for different years, measured by the LHCb experiment [69–71].

Year	$\sqrt{s}$ [TeV]	$\sigma_{b\bar{b}}$ [mb]
2011	7	288 ± 48
2012	8	298 ± 36
2015(16)	13	515 ± 53

Several processes can be considered for the b quark production, gluon-gluon fusion ($gg \to b\bar{b}$) and quark-antiquark annihilation ($q\bar{q} \to b\bar{b}$) being the most probable mechanisms under the conditions in the LHC. Figure 2.3 shows leading order Feynman diagrams for these two processes.

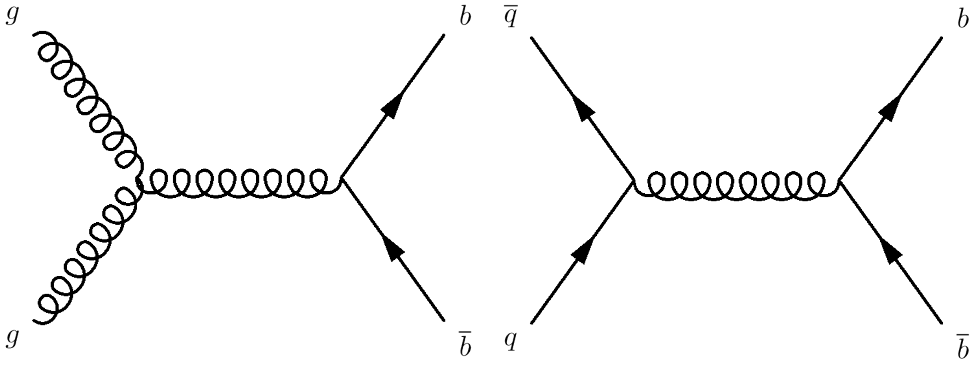

Figure 2.2 – Leading order Feynman diagrams for the $b\bar{b}$ quark pair production from gluon-gluon fusion (left) and quark-antiquark annihilation (right).

The high centre-of-mass energies reached by the LHC, enables the production of the whole spectrum of b hadrons. The $b\bar{b}$ pairs hadronise separately and incoherently, preferably to the comparably light b mesons, i.e. to B^0 (40 %), to B^+ (40 %), to B_s^0 (11 %), and in the remainder of 9 % to the heavier b mesons and baryons [72]. Assuming that detection and selection efficiencies remain constant over these data taking years, the increase of $\sigma_{b\bar{b}}$ by a factor of ~ 1.7 means an equally high increase for the number of measured b hadrons in the LHC experiments. In principle, the productions mentioned above are symmetric in quark flavour and therefore the flavour conjugate states of the b hadrons is implied. But since the pp collisions can be considered a defined initial positively charged state with a baryon number not-equal zero, the ratio of the production rates to specific hadrons and their charge conjugates do not necessarily have to be the same. This so called production asymmetry has to be considered e.g. for measurements of $C\!P$ violation.

Since protons are composite particles, meaning that its constituents may have very different momenta, their collision can lead to a high asymmetry between the two gluon momenta. This in turn leads to a high momentum of the $b\bar{b}$ pair system and hence a strong boost along the flight direction of the protons, parallel to the beam axis. Thus, the probability that both quarks of a $b\bar{b}$ quark pair have small angles $\theta_{1,2}$ wrt. the beam axis is high. Fig. 2.3 depicts the correlation between production angles $\theta_{1,2}$.

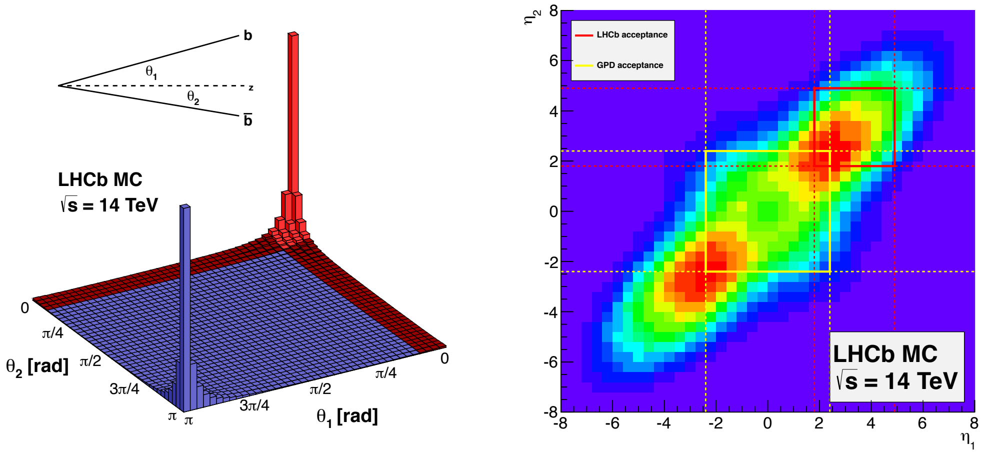

Figure 2.3 – Distributions of the production angle θ (left) and pseudorapidity η (right) from simulated $b\bar{b}$-quark-pair-production in pp collisions with a centre-of-mass energy $\sqrt{s} = 14$ TeV. The detector acceptance of the LHCb detector is marked by the red shaded region / rectangle (left / right). [73]

2.2 The LHCb Detector

The detector of the *Large Hadron Collider beauty* (LHCb) experiment (LHCb detector) was designed to study decays of b as well as c hadrons. The distribution of the $b\bar{b}$ pair production angles shown in Fig. 2.3 leads to the unique design among the four main LHC experiments as a single-arm forward spectrometer, the main reason to only cover the forward region being the limited space in the underground cavern at LHC's IP8 (Interaction Point 8). Figure 2.4 shows a schematic cross section of the detector in the (y, z)-plane. As a single-arm forward spectrometer, LHCb's sub-detectors — for the tracking of particle trajectories and their identification — are arranged from the interaction point at $z = 0$ downstream alongside the beam pipe (positive z-axis). The LHCb detector covers an angular acceptance of ± 15 to 300 mrad (± 250 mrad) in the horizontal (vertical) plane. This translates to an acceptance of particles of $1.8 < \eta < 4.9$, with the *pseudorapidity* $\eta = -\ln(\tan\theta/2)$, θ being the azimutal angle wrt. the beam axis. Looking at Fig. 2.3, where the detector acceptance is marked by the red shaded region, LHCb's acceptance covers about 25 % of the produced $b\bar{b}$ quark pairs.

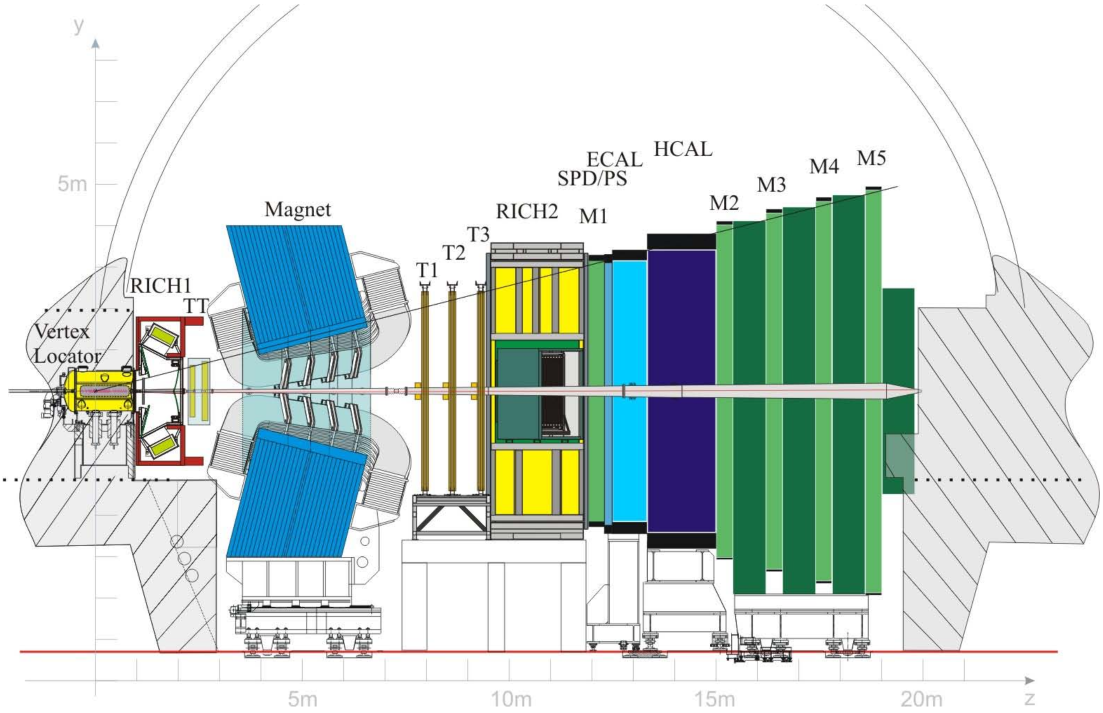

Figure 2.4 – Schematic view of the LHCb detector in the (y, z)-plane [74], modified. The individual sub-detectors shown here are described in detail in Sections 2.2.1 to 2.3.1.

With the *Vertex Locator* (VELO) (see Section 2.2.1), the LHCb detector features a unique sub-detector. Under stable beam conditions, it comes as close as 8 mm to the interaction region to be able to resolve production and decay vertices of b hadrons, which have typical flight distances of $\mathcal{O}(\text{cm})$ due to the boost. During beam injection and acceleration, the aperture of the beam is larger and therefore the VELO is retractable by 3 cm, so that it is in the shadow of the beam pipe and hence protected by fluctuations in the beam diameter. Nonetheless, unexpectedly large fluctuations could lead to severe and even irreversible damage to the VELO and similar sensitive sub-detectors of other LHC experiments. To protect them and the experiments in general, several systems monitor the beam losses and background levels in the vicinity of the LHCb detector to detect instabilities of the beams as early as possible. The main device for this task is the *Beam Conditions Monitor* (BCM) [75]. It is empowered to trigger a beam dump as soon as it measures a density of charged particle around the beam pipe that may damage detector components.

The next sections describe the different sub-detectors of the LHCb experiment. A complete explanation of the detector is presented in Ref. [74]. If not stated otherwise, information is taken from Refs. [74, 76].

2.2.1 Tracking System

The key abilities for the precision measurement of c and b hadrons include an accurate determination of production and decay vertices, particle trajectories and a high momentum resolution under the challenging conditions posed by the environment of a hadron collider. LHCb's tracking system includes the *Vertex Locator* (VELO), surrounding the interaction region of the pp collisions, the *Tracker Turicensis* (TT) upstream of the magnet, and the tracking stations T1–T3 downstream of the magnet, including the *Inner Tracker* (IT) and the *Outer Tracker* (OT). The warm dipole magnet with an integrated magnetic field of 4 Tm deflects charged particles, enabling the measurements of their momenta by measuring the curvature of their tracks. Overall, the tracking system achieves a relative momentum resolution of $\delta p/p = 0.5\,\%$ for lower momenta, up to $1\,\%$ for tracks with a momentum of $200\ \text{GeV}$.

Vertex Locator

Due to their boost (see Section 2.1.3), the b hadrons produced in LHCb have typical flight distances of $\mathcal{O}(\text{cm})$ before decaying. The *Vertex Locator* (VELO) is able to resolve the production and decay vertices and therefore to reconstruct their decay times by measuring cylindrical track coordinates close to the pp interaction region. The cylindrical detector consists of 21 discs installed perpendicular to the beam pipe, of which six are located upstream and fifteen downstream of the nominal collision point. Each disc has a diameter of 42 mm and consists of two halves of silicon strip modules, in order to be able to retract the VELO from the beam during beam injection and acceleration. The individual modules have sensors for measuring the radial distance from the beam pipe, R and the azimuthal angle, φ, of particles. The z-position can be determined through the position of the module along the beam axis. The VELO achieves an *impact parameter* (IP) resolution of $(15 + 29/p_T[\text{GeV}])\mu\text{m}$, the IP being the perpendicular distance of a track to its production vertex.

Silicon Trackers and Outer Tracker

LHCb's tracking system is completed by three additional trackers. The *Tracker Turicensis* (TT), located between the first *Ring-Imaging Cherenkov Detector* (RICH) detector RICH1 (further explained in Section 2.2.2) and the dipole magnet, consists of four layers of silicon micro-strip sensors, covering an area of $130 \times 160\,\text{cm}^2$. The three tracking stations T1–T3 positioned downstream of the magnet combine two detector technologies: the *Inner Tracker* (IT) uses the same technology as the TT and is positioned in a cross-like shape around the beam pipe in T1–T3 with a vertical spread of ~40 cm and a horizontal spread of ~120 cm. The silicon strips used in the TT and IT offer a good hit resolution and fast response time in spite of being installed in regions of high track density and radiation levels. The *Outer Tracker* (OT) extends the IT to the full LHCb acceptance with outer dimensions of about $6 \times 5\,\text{m}^2$. Since the track density is lower in the outer regions of T1–T3, the OT uses straw drift tubes. They are filled with a gas mixture of 70 % Argon, 28.5 % CO_2 and 1.5 % O_2, providing a drift time below 50 ns. The O_2 is injected to enable a recombination with free radicals produced due to radiation and therefore to decrease the rate of ageing [77].

All trackers use a so called x-u-v-x arrangement for their detecting layers: the silicon strips (drift tubes) of the silicon trackers (OT) in the first and the last layer of a station are oriented vertically while the strips in the second (third) layer are tilted by -5° ($+5^\circ$) in the xy-plane. This enables the measurement of the y-coordinate of passing particles. The dimension of the cross-shaped boundary between IT and OT was determined by the requirement, that the occupancies in the OT should not exceed 10 % at an instantaneous luminosity of $2 \cdot 10^{32}\,\text{cm}^{-2}\,\text{s}^{-1}$. Starting with the data taking period after the LS2 however, it is planned to record data at an increased luminosity of $2 \cdot 10^{33}\,\text{cm}^{-2}\,\text{s}^{-1}$. This requires among others an upgrade of the tracking system because an excessive increase of the track multiplicity. Section 2.4 will give a short introduction of the LHCb detector upgrade and Section 7.1 focusses on the upgrade of the tracking stations T1–T3, as a preparation for the simulation studies of the new tracker replacing the IT and OT shown in Chapter 7.

2.2.2 Particle Identification System

Because of the high multiplicity of a hadronic collider, the accurate identification of final state particles plays a crucial role in the analysis of interesting b and c hadron decays. In a measurement of a rare process for example, particles stemming from common decays with a similar topology could be confused with signal particles and therefore distort the measurement. In the LHCb detector, the *particle identification* (PID) system, consisting of two *Ring-Imaging Cherenkov Detector* (RICH) detectors, the calorimeter system, and the muon system, aims at minimizing this effect. By combining all information, likelihoods for different particle hypotheses can be determined.

RICH Detectors

The main task of the Ring-Imaging Cherenkov Detector detectors, RICH1 and RICH2, is to distinguish between charged pions, kaons and protons. For this, they exploit the Cherenkov effect: If a particle travels through a dielectric medium at a certain velocity v, that is greater than the speed of light c' in this medium, it is emitting photons in a cone along the flight direction. The opening angle θ_C of this cone is correlated with the particle's speed via

$$\cos\theta_\mathrm{C} = \frac{c'}{v} = \frac{c}{nv} \tag{2.1}$$

where n denotes the medium's refractive index. With the help of spherical mirrors, the Cherenkov photons are projected onto photo-detectors, where they can be reconstructed as rings. Together with the information on the particle momentum from the tracking system, measurements of the rings radius and θ_C allow to calculate v and therefore likelihoods for different mass hypothesis. Figure 2.5a shows an example of reconstructed Cherenkov rings.
RICH1 is positioned between VELO and TT and covers a momentum range of $\sim$1–60 GeV/c using $\mathrm{C_4F_{10}}$ and, in Run I, aerogel as Cherenkov radiators. RICH2, which is located downstream of the T stations, employs a $\mathrm{CF_4}$ radiator that covers charged hadron separation between 15 and 100 GeV/c. Both detectors use a combination of flat and spherical mirrors to direct the Cherenkov light out of the detector acceptance and to focus the ring images on *Hybrid Photon Detector* (HPD) as can be seen in Fig. 2.5b.

Calorimeters

LHCb's calorimeters provide energy measurements of particles and are the only way to detect neutral particles. They are further used for trigger decisions, based on the presence of e.g. hadrons above a certain deposited energy. The whole calorimeter system consists of the *scintillator pad detector* (SPD), the *preshower detector* (PS), the *electromagnetic calorimeter* (ECAL), and the *hadron calorimeter* (HCAL). The SPD enables the distinction between photons and electrons, since only electrons induce particle showers. Separated by a lead layer of 2.5 mm thickness from the SPD, the PS allows for a better separation of electrons from light charged hadrons. The last two components of the calorimeter system are designed as so called *shashlik* calorimeters, where alternating layers of lead (iron) cause traversing particle to produce electromagnetic (hadronic) showers in the ECAL (HCAL) and scintillator material layers measure the energies of those showers.

Muon System

The identification of muons and the triggering of muons with a high *transverse momentum* (p_T) are two important tasks for the LHCb detector, since muons are present in

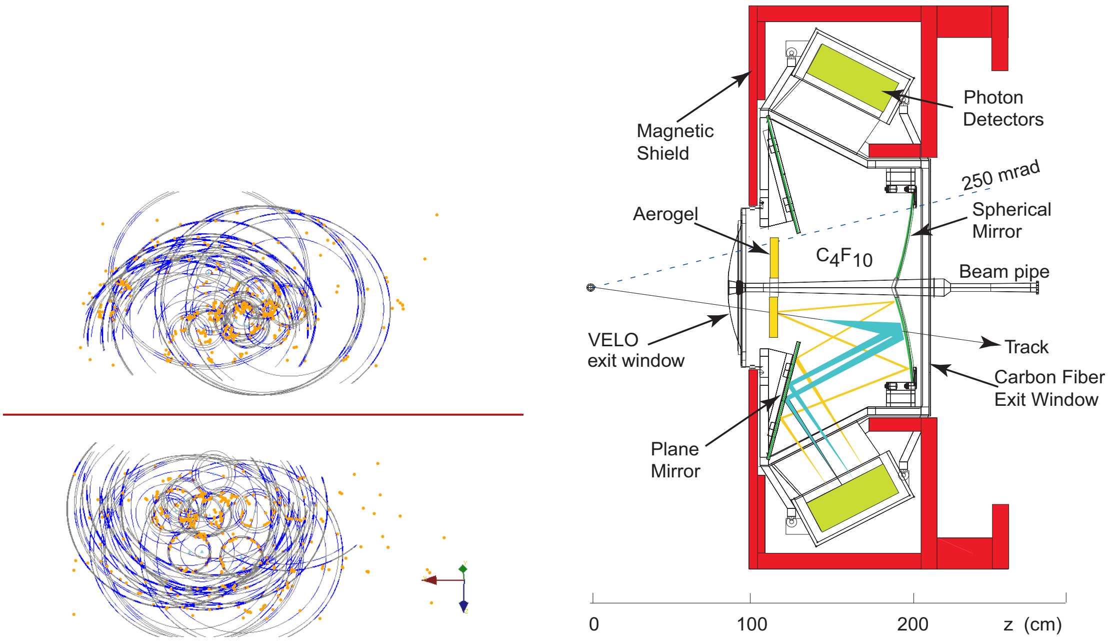

(a) **(b)**

Figure 2.5 – (a) Reconstructed rings, fitted to measured Cherenkov photons (orange dots) [78]. (b) Side view of the schematic layout of RICH1 [74].

many $C\!P$-sensitive or rare b hadron decays, for example the two gold-plated channels for $C\!P$ violation $B_s^0 \to J/\psi(\mu^+\mu^-)\phi$ and $B^0 \to J/\psi(\mu^+\mu^-)K_S^0$ or the rare decay $B_s^0 \to \mu^+\mu^-$.[1] The muon system consists of five stations M1–M5 with a total absorber length of about 20 interaction lengths, including the calorimeter system. They are built of *multi-wire proportional chamber* (MWPC) combined with 80 cm thick iron absorbers in M2–M5 and a triple-gas electron multiplier detector in the inner region of M1 that is more capable at withstanding the high particle flux close to the beam pipe. M1–M3 are particularly used to measure the p_{T} and the track direction of muon candidates while the main purpose of M4 and M5 is the identification of piercing particles.

2.3 Data Processing at LHCb

The following subsections give an overview of the processing of recorded and simulated data within the LHCb experiment. Since only a small fraction of the pp collisions in the LHCb detector shows processes that are of interest for further studies, measured events first have to pass so called triggers, that reduce the data-flow rate from 40 MHz to 5 kHz. This is further explained in Section 2.3.1. The next steps are the reconstruction and

---

[1] The notation $J/\psi(\mu^+\mu^-)$ is short for $J/\psi \to \mu^+\mu^-$

further selection of interesting events with the LHCb software. Section 2.3.2 elaborates on the generation of simulated datasets for physics analysis purposes and upgrade studies.

2.3.1 Trigger Stages

Operating at the nominal LHC bunch crossing rate of 40 MHz with the nominal Run I LHCb luminosity of $2 \cdot 10^{32}\,\mathrm{cm}^{-2}\,\mathrm{s}^{-1}$, $b\bar{b}$ pairs are produced at a rate of ~100 kHz. Of these events, only ~15 % lead to the hadronisation and decay of a B with all decay products in the acceptance of the LHCb detector. This number of interesting events is further reduced by the fact that the branching ratios of rare or $\mathcal{CP}$-sensitive decays, that are considered worth storing for physics analysis are typically less than 10^{-3} [74]. The task of LHCb's two consecutive trigger stages is to maximise the ratio of events of interest for physics analyses by reducing the amount of irrelevant events. Figure 2.6 gives an overview of the different trigger schemes in 2011, 2012 and Run II. The following description of the trigger stages is based on [79–81].

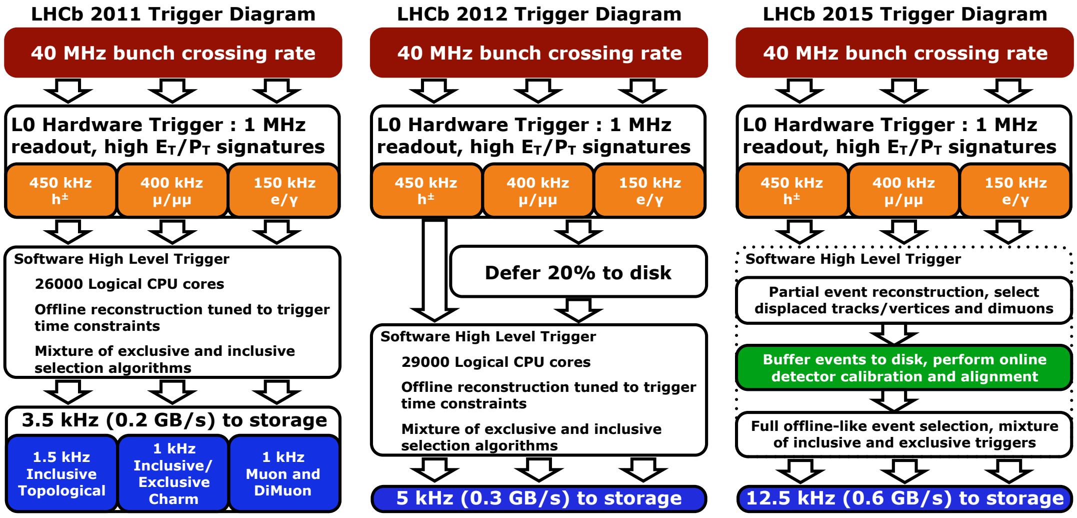

(a) 2011 **(b)** 2012 **(c)** Run II

Figure 2.6 – Trigger schemes in (a) 2011 (no events deferred), (b) 2012 (20 % of events accepted by L0 deferred to disc for later processing), and (c) 2015 (exemplary for Run II) (all events accepted by HLT1 deferred). [79, 81].

Level Zero

The *Level-0* (L0) trigger is hardware-based and operates synchronously to the bunch crossing rate. To achieve this, its decisions are based on the detector systems that offer fast responses: the muon and calorimeter systems. The L0 calorimeter trigger `L0Photon`, `L0Electron`, and `L0Hadron` draw a first particle hypothesis from the reconstruction of particles with a high *transverse energy* (E_{T}) measured in the ECAL or HCAL, combined with the information from PS and SPD. For the selection of hadrons, e.g. in $B_s^0 \to K_{\mathrm{S}}^0 K_{\mathrm{S}}^0$, typical thresholds in `L0Hadron` are $E_{\mathrm{T}} > 3.5$ GeV (3.7 GeV) for 2012 (Run II). The `L0Muon` and `L0DiMuon` trigger select events with high p_{T} muons that are an indicator for interesting decays as explained above.

Furthermore the L0 identifies and discards events with a *primary vertex* (PV) multiplicity above a certain threshold through the VELO pile-up (proton interactions per bunch-crossing) system, since such events are disadvantageous for the analysis of *b* hadron decays. The total output rate of L0 is limited to 1 MHz, which enables the subsequent trigger stages to execute more complex and thus computing time-consuming algorithms which in turn leads to more precise reconstructions of events.

High Level Trigger

The second trigger stage *High Level Trigger* (HLT), consisting of HLT1 and HLT2, is software based and runs on a so called *Event Filter Farm* (EFF) with ~ 29 000 (~ 52 000) logical CPU cores in 2012 (Run II). The EFF is located in the LHCb cavern, behind the shielding wall outside the radiation area. After passing the HLT, an event is sent to the storage system to be further processed by the central preselection, the so called *stripping* (see Section 2.3.2).

In a first step, HLT1 performs a partial reconstruction of an incoming event, by using information from the tracking system to reconstruct tracks of charged particles with an adequate *impact parameter* (IP), the so called *Forward Tracking*. The event is passed to HLT2, if at least one track in the event passes the criteria on track quality and p_{T}. The thresholds for those criteria can be tuned to reach an optimal output rate. In 2012, the HLT1 output rate was tuned to ~ 150 kHz.

With this further reduced input rate, HLT2 achieves a reconstruction of the complete event with the input information on vertices and tracks from HLT1. In addition to that, first physics selections are applied, e.g. topological trigger lines based on 2-, 3- and 4-body detached vertices to inclusively select *c* and *b* hadron decays.

During its first data taking period, the LHC achieved to deliver stable *pp* collisions for ~ 30 % of the time. In order to use the idle time of the EFF, the LHCb trigger started to use the local hard discs of the EFF to improve the overall performance of the HLT. As can be seen in Fig. 2.6b, ~ 20 % of the events accepted by the L0 stage were stored (deferred) for a later processing in the time between two LHC fills. This more effective use of the EFF's CPU power enabled an improvement of the reconstruction in HLT2, one example being the employment of a track reconstruction algorithm for long lived particles, e.g. K_{S}^0, which could also reconstruct their trajectories if they decayed outside the VELO.

In the course of Run II, the trigger scheme was changed in the way that HLT1 and HLT2 were turned into two asynchronous, independent stages operating on the same nodes. Now, all events that pass the HLT1 requirements are deferred to the local storage for a later processing, see Fig. 2.6c. The EFF resources freed up as a result enable an optimal execution time per event for both HLT steps and allow for an online calibration and alignment of the detector before the HLT2 reconstruction. The optimized calibration lead to an offline- quality reconstruction in HLT2.

2.3.2 Software

The data for the various studies performed for this thesis is either simulated data or data recorded by the LHCb detector‘s *Data Acquisition* (DAQ). In both cases, it is processed by the LHCb software framework, as depicted in Fig. 2.7. The framework is mostly based on the `GAUDI` [82] framework and it is subdivided into several packages with separate tasks and fields of application. The following paragraphs will elaborate on the most important of these packages: the software package for reconstruction, `Brunel`, the end-user software package for n-tuple selection and analysis, `DaVinci`, and the packages `Gauss` (including `Geant4`) and `Boole` for the generation of simulated data. Not further explained here is the software package `Moore`, which employs the software code for the High Level Trigger and has therefore implicitly been described in Section 2.3.1.

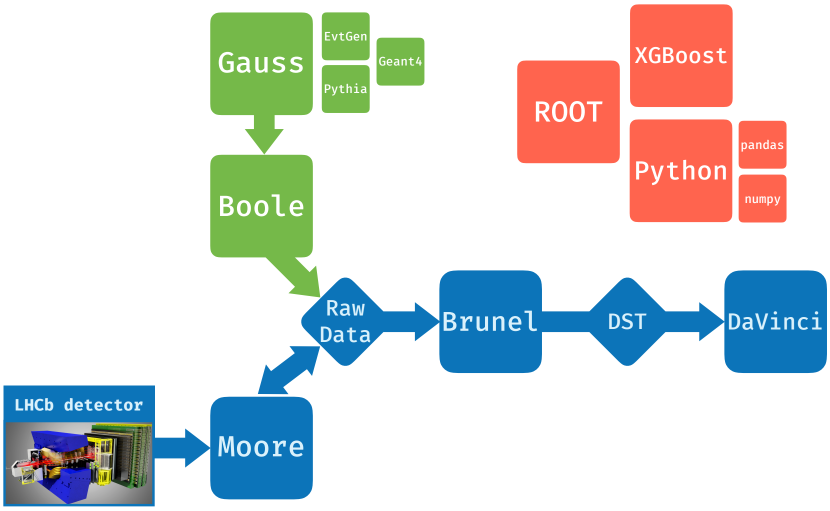

Figure 2.7 – A schematic overview of the data flow in the LHCb experiment and the software packages involved. The rhombi indicate different data formats while software packages are represented by squares. The flow of simulated data is shown in green (top left), data flow that is common to simulated and recorded data is shown in blue (bottom). Red indicates software packages, that are not part of the LHCb software framework and are not directly linked to these data flows, but used in the end-user data analysis (top right).

Reconstruction

The `Brunel` [83] software project is a collection of interfaces to algorithms and tools used for the event reconstruction from either simulated data (see Section 2.3.2) or the output of the DAQ system. More precisely, the reconstruction of tracks from charged particles using hits in the tracking system, the reconstruction of neutral particles, e.g. π^0's or γ's, using measurements from the calorimeters, and the *particle identification* (PID), where information from measured calorimeter clusters, RICH rings and hits in the muon stations are used. From this, the event reconstruction creates so called proto-particle objects, containing information from the tracking and PID that are used for the further reconstruction of specific decay chains.

Tracking `Brunel` contains several algorithms, which combine hits in the VELO, the TT and the tracking stations T1–T3 to reconstruct the particle trajectories (tracks) through the LHCb detector. The track reconstruction starts with the search for so called *seeds* — the initial track candidates [84] — in the region where the magnetic field is low, i.e. the VELO and the T stations (see upper part of Fig. 2.8). After the removal of duplicate track segments by a so called Clone Killer algorithm [85], the next step is then to fit the particle trajectories with a Kalman filter [86] that corrects for $\mathrm{d}E/\mathrm{dx}$ energy loss and accounts for multiple scattering. The χ^2 and the pull distribution of the fit serve as benchmark for the quality of reconstructed tracks. The reconstructed tracks are divided into five different track types, which depend on the sub-detectors that are involved in the reconstruction as shown in Fig. 2.8:

Long track: The so called long tracks have the most precise momentum measurement and spatial resolution in the primary interaction region, as they are reconstructed in the whole tracking system from the VELO to the T stations. Therefore, they are the most valuable tracks for the reconstruction of b hadron decays.

Downstream track: These tracks are reconstructed from hits in the TT and the T stations and are important for the reconstruction of decay products from long-lived particles such as K^0_S mesons or Λ baryons that can decay outside of the VELO.

Upstream track: Particles that are bent out of the acceptance of LHCb, e.g. due to their low momenta, are measured in the VELO and the TT. Since they still pass RICH1, they can be used as an input for the particle identification algorithms of the RICH detectors, e.g. for a better understanding of background.

VELO track: The fourth type of track is the VELO track, which is — as the name implies — reconstructed in the VELO. On the one hand they can be used for the reconstruction of primary vertices, on the other hand they are utilised as an input for the search of long or upstream tracks.

T track: Tracks that are reconstructed only in the T stations are denoted as T tracks. They are not used in physics analyses but are utilised as an input for the reconstruction of Downstream tracks.

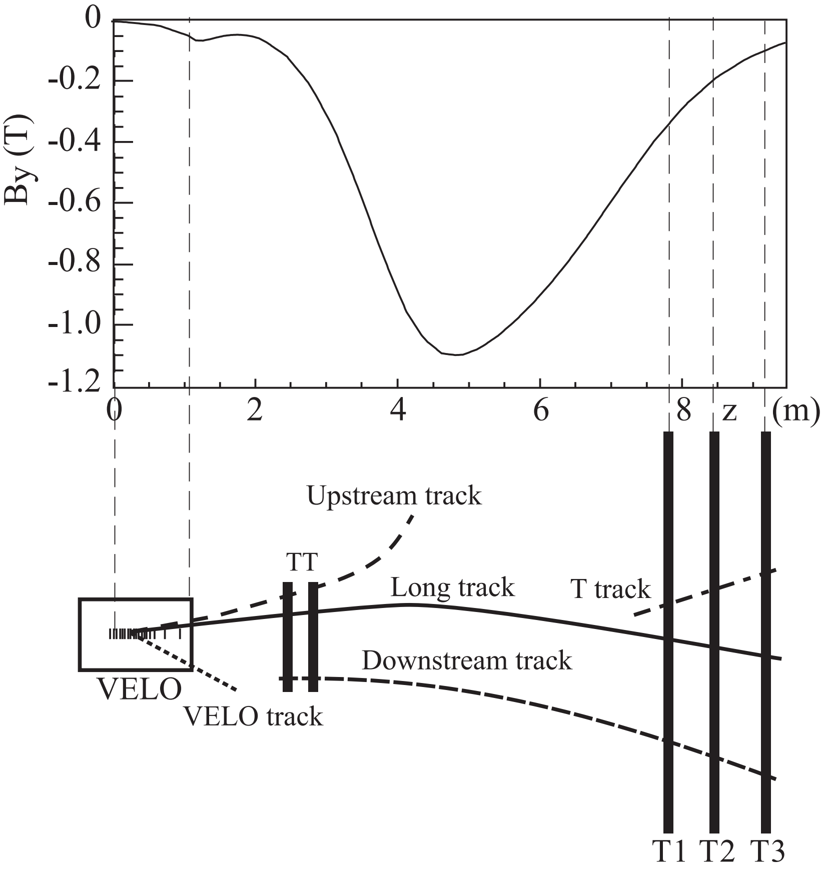

Figure 2.8 – Schematic illustration of the different track types in the (y, z)-plane: Up-/Downstream, Long, T, and VELO track. The main magnetic field component (B_y) as a function of z is shown above, as a reference. [74]

Particle Identification As introduced in Section 2.2.2, the identification of particles (PID) is achieved by combining measurements from the sub- detectors of the PID system.

The calorimeter system is able to identify electron, π^0 and γ candidates by combining tracks and clusters in SPD, PS and the calorimeters.

Charged hadrons, i.e. $\overset{(-)}{p}$, $\pi^\pm$ and $K^\pm$ are distinguished with the RICH system. Under consideration of all tracks and HPD pixel hits, the global likelihood of an event is minimized by varying the particle hypothesis for each track successively. The result of this procedure are the differences of the logarithmic likelihood $\Delta\mathcal{L}$, which is obtained by replacing the individually determined particle hypothesis of each track with a pion hypothesis.

The information from all PID sub-systems is combined using neural nets (NN) to calculate total probabilities (ProbNN$K^{\pm}$, ProbNN$\pi^{\pm}$, etc.) for each particle hypothesis of charged particles.

Stripping and Data Selection

The final part of the data flow in the LHCb experiment — before the end-user data analysis — is performed with the `DaVinci` [87] software package. By combining the proto-particles created in the reconstruction and particle hypotheses, it forms final state particle objects, which are further combined to intermediate states. At the end, the full decay chain can be reconstructed.

The `DaVinci` package incorporates various algorithms that produce observables for the use in physics analyses, e.g. algorithms to calculate kinematic variables of all particles in a decay chain, to reconstruct and fit said decay chains, and, in case of simulated events, to match reconstructed particles with the initially generated particles. The algorithm's outputs can be used to determine requirements on the reconstruction quality of combined particles and decay chains to separate background candidates.

Considering an an average of 60 LHCb publications per year, it would be highly inefficient in terms of computing resources, to allow an individual physics analysis to access the full dataset for the reconstruction of a particular decay. Instead, the first step of signal reconstruction and selection, the so called *stripping*, is organized and performed centrally. This is among other things possible, because many analysed decays share the same (type) of intermediate particles, e.g. decays like $B \to K^0_S hh$ with $K^0_S \to \pi^+\pi^-$. The stripping employs in- and exclusive selections, so called stripping lines, with loose requirements on the combination of final and intermediate state particles to signal decays. The stripping-selected data is then accessible to the collaboration and can be further processed with individual `DaVinci` algorithms to create `ROOT` [88] n-tuples, which contain the determined decay observables as well as the event and candidate information needed for the physics analyses. The n-tuples are then further selected locally (*offline*) with `ROOT` itself or software frameworks like `Python` by the analysts.

Simulation

The generation of simulated events is performed with the `Gauss` [89, 90] software package which in turn makes use of other software packages for different stages of the simulation, see Fig. 2.7: The pp collisions as well as the hadronisation process is simulated with the Monte Carlo generator `Pythia` [91, 92]. Since it contains many established models for the mixing and CP violation of heavy hadrons, their decay is simulated with `EvtGen` [93] and the software package `Geant4` [94, 95] simulates the interaction of particles with the detector material.

In a next step the digitization of traversing particles' energy deposition, i.e. the detector response, and the decision of the L0 trigger stage are emulated with the `Boole` [96] package. The remaining data flow of simulated events is the same as for recorded data, as depicted in Fig. 2.7.

Various simulation samples can be generated for different purposes: For studies of the sub-detectors, e.g. after an upgrade, only parts of the simulation chain are used, for example `Boole` and `Brunel` to study the detector response and reconstruction capabilities. To study the physical properties of a detector and its interaction with particles and radiation a confined simulation with `Geant4` can be performed, as shown in Chapter 7, Page 101.

For physics analyses, Signal Monte Carlo samples are used to study the signature of a certain signal process (e.g. $B_s^0 \to K_S^0 K_S^0$), e.g. to calculate efficiencies of certain processes.

2.4 The LHCb Upgrade

Since the LHCb's physics agenda of high precision measurements in *c* and *b* hadron decays relies on a precise determination of their production (primary) and decay (secondary) vertices, LHCb recorded at an instantaneous luminosity of approximately $2 \cdot 10^{32}$ to $4 \cdot 10^{32}\,\mathrm{cm}^{-2}\,\mathrm{s}^{-1}$, a factor 25 to 50 below the LHC design luminosity of $10^{34}\,\mathrm{cm}^{-2}\,\mathrm{s}^{-1}$, during the data taking periods of 2011–2012 (Run I) and 2015–2018 (Run II). In order to boost the sensitivity of rare heavy flavour processes, the LHCb experiment is planning to record data at an instantaneous luminosity of $2 \cdot 10^{33}\,\mathrm{cm}^{-2}\,\mathrm{s}^{-1}$, after the LHC *Long Shutdown 2* (LS2) (2019–2020). However, because of limiting components of the current LHCb detector design, an increased instantaneous luminosity does not imply an equal increase in interesting data [7]. Even after upgrading sub-detectors like the OT, which would suffer from a highly enlarged occupancy due to the higher track multiplicity, the hardware trigger stage would remain a limiting factor. The Level-0 thresholds, that would be required to reduce the read-out rate at higher luminosities, would also reject signal events. This leads to reduced trigger efficiencies, especially for hadronic decays. Hence, the data recorded by the sub-detectors of the upgraded LHCb detector will be read out trigger-less at the full collision rate and further processed by a full software trigger, as shown in Fig. 2.9a. To further increase the trigger efficiencies, a simplified version of the offline reconstruction is already employed at trigger level (see Fig. 2.9b).

Besides the upgraded front-end electronics for a trigger-less read-out, the LHCb sub-detectors are further upgraded to maintain their performance at the higher instantaneous luminosity. Figure 2.10 shows a schematic side view of the upgraded LHCb detector. The next sub-sections will elaborate more on the specific sub-detector upgrades.

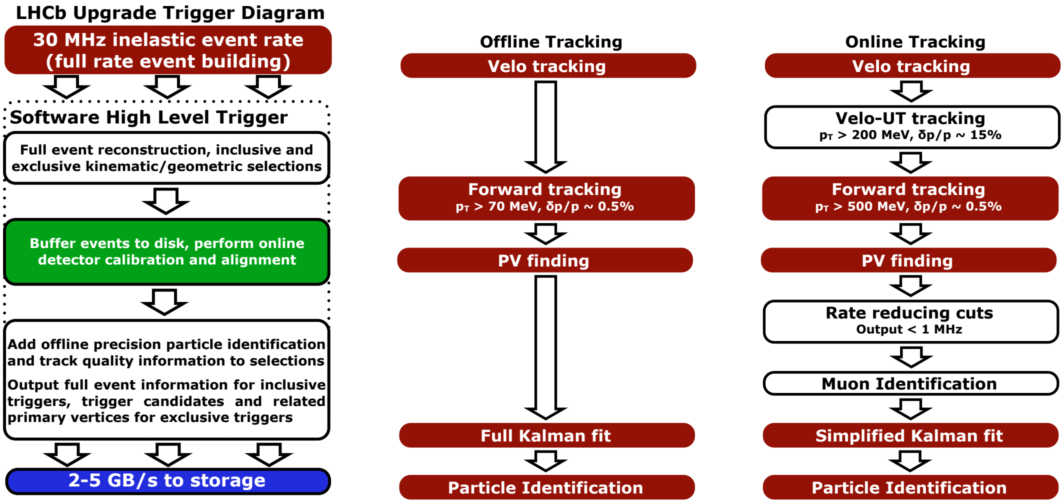

(a) Trigger Scheme **(b)** Online Tracking

Figure 2.9 – (a) Trigger Scheme as planned for the LHCb Upgrade; The software High Level Trigger processes data at the full event rate, without filtering the events with a hardware trigger stage. (b) Comparison between on- and offline reconstruction; To increase the trigger efficiencies, a simplified version of the reconstruction is already performed at trigger level. [97]

2.4.1 Upgrade of the Tracking System

In the course of the LHCb Upgrade, all sub-detectors of the tracking system will be replaced. Due to the higher track multiplicities, the tracking detectors need higher granularities and, as mentioned before, their front-end electronics are required to read out data with the full collision rate.

The new Vertex Locator is a pixel detector with $\sim 41 \cdot 10^6$ pixels with an area of $55 \times 55\,\mu\text{m}^2$ each [98]. The pixel sensors are arranged in a similar pattern as in the old VELO but will be closer to the Interaction Point, the closest distance to the beam axis being 5.1 mm.

Also the tracking stations up- and downstream of the magnet will be replaced. In general, all trackers are designed to maximise the tracking efficiency as well as spatial and momentum resolution. By increasing the detecting layers, the tracking efficiency could be increased, but the higher material budget leads to multiple scattering due to the higher radiation length, which in turn aggravates the momentum resolution. The replacement for the TT, the *upstream tracker* (UT), features the same x-u-v-x geometry and also uses silicon micro-strips as the detecting material. The sensors are directly connected to especially developed *Application-specific integrated circuits* that serve as front-ends. Close to the beam-pipe, the micro-strips arrangement is optimized for a higher granularity. The downstream tracking stations are interchanged with a new homogeneous tracking detector, instead of separated Inner and Outer Tracker: The new *Scintillating Fibre* (SciFi) tracker, uses scintillating fibres, instrumented by *silicon*

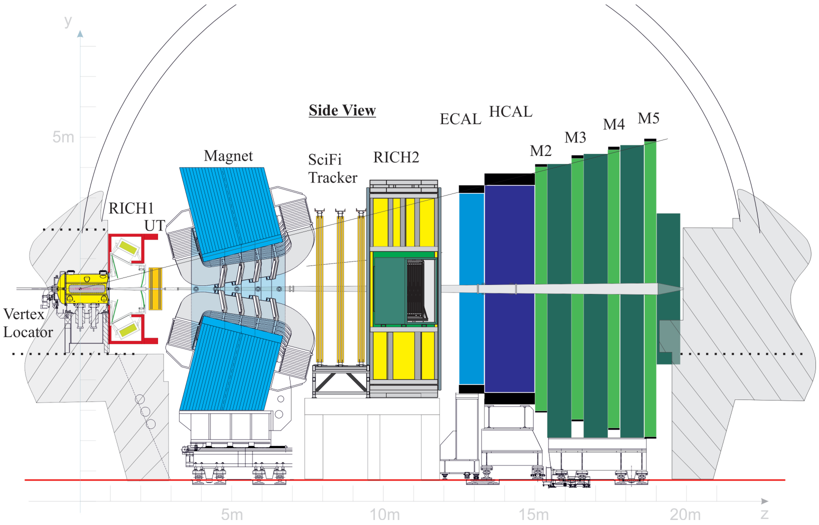

Figure 2.10 – Schematic view of the upgraded LHCb detector in the (y, z)-plane [8], modified. Compared to Fig. 2.4, the main changes noticeable in this figure are the removal of M1, the replacement of the TT by an *upstream tracker* (UT), and the replacement of the tracking stations T1–T3 with IT and OT by the *Scintillating Fibre* (SciFi) tracker.

photomultipliers (SiPMs). The LHCb Tracker Upgrade Technical Design Report, Ref. [8], makes the following demands:

- A single hit spatial resolution of $\leq$ 100 µm in the bending plane, compared to 200 µm / 50 µm for the OT / IT, which leads to a comparable momentum resolution $\delta p/p$ of ~0.3 to 0.6 % for tracks between 1 and 50 GeV. As shown in Fig. 2.11, a better hit resolution would not necessarily lead to a better momentum resolution. Furthermore, this single hit spatial resolution is sufficient, since the extrapolation of long tracks is dominated by effects from multiple scattering in the detectors upstream of the magnet.

- A material budget with a radiation length of $\leq$ 1 % per detecting module, so that the effects of multiple scattering are smaller compared to those in the upstream tracker.

- A hit detection efficiency as large as possible (~99 %), as well as front- and back-end electronics capable of a read-out at the full collision rate of 40 MHz.

- The SciFi tracker should be well-suited to uphold this required performance for an integrated luminosity of up to 50 fb^{-1} (LHC Run III & Run IV).

The SciFi tracker is further described in Section 7.1, on Page 101.

2.4.2 Upgrade of the Particle Identification System

The main changes for the sub-detectors of the PID system are needed because of the removal of the L0 trigger and the 40 MHz detector read-out [99].
Since the RICH electronics are encased together with the HPDs, the upgraded RICH detectors will feature Multi-anode Photomultipliers with external read-out electronics. Furthermore, the RICH1 mirror geometry will be optimized for higher occupancies.
Concerning the calorimeter system, the PS and SPD will be removed, since they mainly provided information for the hardware trigger. An upgrade of the inner part of the ECAL is foreseen for the LHC Long Shutdown 3. Apart from that, the electronics of the calorimeters will be upgraded for the 40 MHz read-out.
Because of the increased occupancies due to the higher track multiplicities, the first station of the muon system M1, will be removed. The remaining stations M2–M5 will be protected by a new shielding in front of M2, which reduces the particle flux. Concerning the muon system electronics, only the back-end electronics need to be upgraded for the new full software trigger.

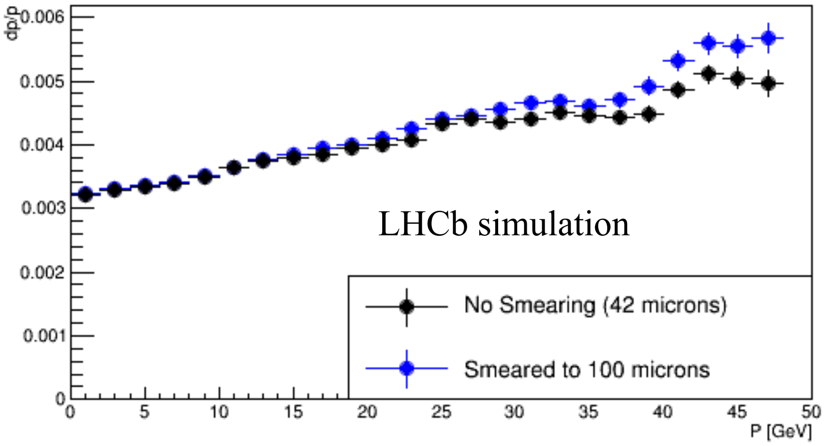

(a) Long Track Momentum Resolution

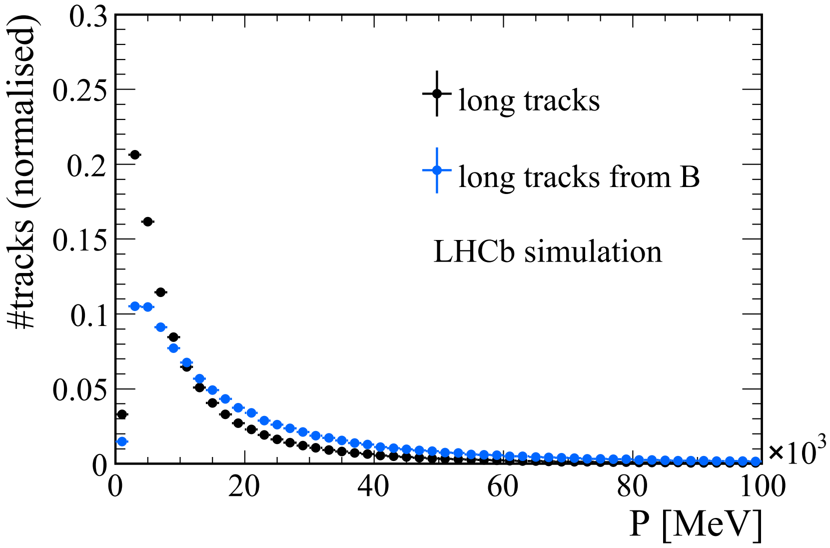

(b) Long Track Momentum Distribution

Figure 2.11 – (a) Simulated long track momentum resolution for different single hit spatial resolutions of the SciFi tracker. (b) Simulated momentum distribution of particles reconstructible as long tracks in $B_s^0 \to \phi\phi$ at $\sqrt{s} = 14$ TeV. Comparing the two figures, it can be observed that the momentum resolution is not improved by improving the hit resolution from 100 to 42 µm, as the majority of tracks have a momentum $p \leq 20$ GeV. [8].

3 Analysis Strategy and Methods

This chapter outlines the strategy and applied methods of the physic analysis conducted in the course of this thesis. The analysis aims at the determination of the branching ratio of $B_s^0 \to K_S^0 K_S^0$ decays normalised to the branching ratio of the decay $B^0 \to \phi K_S^0$. To minimize a potential bias of the experimenter, the analysis is performed blinded, i.e. the expected signal region in the distribution of the reconstructed B_s^0 meson mass was excluded on data, until every selection step was completely understood.
Section 3.1 introduces the general analysis strategy, Section 3.2 describes the overall approach for the selection of signal candidates, and Sections 3.3 to 3.4 give a short overview of two important statistical methods used in this analysis. The chapter concludes with a short discussion on the topic of differences between simulation and data.

3.1 Analysis Strategy & Data Samples

In general, the branching ratio $\mathcal{B}(B \to f)$ of a B meson decay to a final state f is defined through

$$\begin{aligned} N(B \to f) &= 2\,\sigma_{b\bar{b}}\,\mathcal{L}_{\text{int}} f_q\,\varepsilon_{\text{tot}}\,\mathcal{B}(B \to f) \\ \Leftrightarrow \mathcal{B}(B \to f) &= \frac{N(B \to f)}{2\sigma_{b\bar{b}}\mathcal{L}_{\text{int}} f_q \varepsilon_{\text{tot}}}. \end{aligned} \tag{3.1}$$

Here, $N(B \to f)$ denotes the number of signal candidates of the individual investigated signal decay, i.e. $B_s^0 \to K_S^0 K_S^0$ or $B^0 \to \phi K_S^0$. Furthermore, this number of signal candidates is governed by parameters describing the formation process of B mesons, i.e. the production cross section of $b\bar{b}$ quark pairs $\sigma_{b\bar{b}}$ (see Section 2.1.3), the integrated luminosity $\mathcal{L}_{\text{int}}$, and the probability for a b quark to hadronise with a s (d) quark f_q with $q = s$ (d) for B_s^0 (B^0) mesons. The number of observable signal candidates is diluted by the total selection efficiency ε_{tot}, which is a product of the individual efficiencies of each selection step, outlined in Section 3.2. By calculating the branching ratio of a decay relative to the branching ratio of another decay with similar decay properties and topology, i.e. $B^0 \to \phi K_S^0$, it is possible to reduce certain systematic effects in the measurement. For example, the external parameters $\sigma_{b\bar{b}}$ and $\mathcal{L}_{\text{int}}$ cancel completely in the ratio, while the systematics of individual selection steps may cancel partially for common stages. The ratio of the branching ratios for main and normalisation channel, each calculated after Eq. (3.1), is given as

$$\frac{\mathcal{B}(B_s^0 \to K_S^0 K_S^0)}{\mathcal{B}(B^0 \to \phi K_S^0)} = \left(\frac{2\mathcal{L}_{\text{int}}\sigma_{b\bar{b}}}{2\mathcal{L}_{\text{int}}\sigma_{b\bar{b}}}\right) \cdot \frac{\varepsilon_{\phi K_S^0}}{\varepsilon_{K_S^0 K_S^0}} \cdot \frac{f_d}{f_s} \frac{N_{K_S^0 K_S^0}}{N_{\phi K_S^0}} = \frac{\varepsilon_{\phi K_S^0}}{\varepsilon_{K_S^0 K_S^0}} \cdot \frac{f_d}{f_s} \frac{N_{K_S^0 K_S^0}}{N_{\phi K_S^0}}. \tag{3.2}$$

In the equation, $\varepsilon_{K_S^0 K_S^0/\phi K_S^0}$ is the total selection efficiency and $N_{K_S^0 K_S^0/\phi K_S^0}$ is the yield of signal candidates obtained in the specific decay channel.
In order to extract signal candidates for the main and normalisation channel, different selection steps are applied on data recorded in the years 2011 ($\mathcal{L}_{\text{int}} = 1\,\text{fb}^{-1}$, $\sqrt{s} = 7\,\text{TeV}$), 2012 ($\mathcal{L}_{\text{int}} = 2\,\text{fb}^{-1}$, $\sqrt{s} = 8\,\text{TeV}$), 2015 ($\mathcal{L}_{\text{int}} = 0.3\,\text{fb}^{-1}$, $\sqrt{s} = 13\,\text{TeV}$) and 2016 ($\mathcal{L}_{\text{int}} = 1.7\,\text{fb}^{-1}$, $\sqrt{s} = 13\,\text{TeV}$), with the integrated luminosity as well as the centre-of-mass energy of these years in parentheses. The selection strategy is further outlined in Section 3.2.2, while the specific steps are discussed in detail in Section 4.1.3 ff. for $B^0 \to \phi K_S^0$ and Section 5.1.2 for $B_s^0 \to K_S^0 K_S^0$, respectively.
In addition to recorded data samples, simulated samples of both channels are used as signal proxies for different studies and for the determination of selection efficiencies, see Section 3.2.3. The reason why simulated samples can be problematic is further elaborated in Section 3.5.
To account for the different centre-of-mass energies and resulting decay kinematics, the analysed datasets of the main channel, $B_s^0 \to K_S^0 K_S^0$, and the normalisation channel, $B^0 \to \phi K_S^0$, are each split into four total subsets based on the data taking period — Run I for 2011 & 2012 and Run II for 2015 & 2016 — and the track types of the pions from $K_S^0 \to \pi^+\pi^-$. A detailed description of the track types is given in Section 2.3.2, Page 38.
The track categories, i.e. the combination of track types, of the main channel used in this analysis are:

LL Both K_S^0 mesons are reconstructed from long track $\pi^\pm$ mesons.

LD One K_S^0 meson is reconstructed from downstream track $\pi^\pm$ mesons while the other one is reconstructed from long track $\pi^\pm$ mesons.

DD Both K_S^0 mesons are reconstructed from downstream track $\pi^\pm$.

Because of the very small trigger efficiency and the non-existence of a suitable normalisation channel, the last track category could not be considered for the calculation of the branching ratio [6]. For the normalisation channel $B^0 \to \phi K_S^0$ the track categories are defined as:

LL The K_S^0 meson is reconstructed from two long track $\pi^\pm$ mesons.

DD The K_S^0 meson is reconstructed from two downstream track $\pi^\pm$ mesons.

For the final determination of the relative branching ratio a "normalisation constant", α, which is defined from Eq. (3.2) as

$$\Rightarrow \mathcal{B}(B_s^0 \to K_S^0 K_S^0) = \underbrace{\frac{\varepsilon_{\phi K_S^0}}{\varepsilon_{K_S^0 K_S^0}} \cdot \frac{f_d}{f_s} \cdot \frac{\mathcal{B}(B^0 \to \phi K_S^0)}{N_{\phi K_S^0}}}_{\equiv \alpha} \cdot N_{K_S^0 K_S^0} \tag{3.3}$$

is computed for each subset of the data, i.e. Run I LL (LL), Run I LD (DD), Run II LL (LL), Run II LD (DD) for the main (normalisation) channel. For f_s/f_d and the branching ratio of $B^0 \to \phi K_S^0$, external inputs are used, as explained in Section 6.1. Because of its instantaneous decay, the ϕ is reconstructed from two long track $K^\pm$. Therefore, the result determined from the subset $\mathrm{LL}_{K_S^0 K_S^0}$ is normalised to the result obtained from the subset $\mathrm{LL}_{\phi K_S^0}$ while the the result for the subset $\mathrm{LD}_{K_S^0 K_S^0}$ is normalised to the result from the subset $\mathrm{DD}_{\phi K_S^0}$. The branching ratio is then determined from a simultaneous unbinned maximum likelihood fit (see Section 3.3) to the B_s^0 mass distributions in all four subsets, with a shared parameter $\mathcal{B}(B_s^0 \to K_S^0 K_S^0)_{\text{pred}}$, as

$$\mathcal{B}(B_s^0 \to K_S^0 K_S^0)_{\text{pred}} = \alpha_i \cdot N_{K_S^0 K_S^0, i} \tag{3.4}$$

with $i \in$ {Run I LL, Run I LD, Run II LL, Run II LD}. This approach is further explained in Section 6.3.

3.2 Selection and Reconstruction

In this section, the different steps performed in the selection of the main and the normalisation channel are outlined and explained in detail, where necessary.

3.2.1 Decay Tree Fit

The first step in the reconstruction of the decay is a common bottom-up fit of the decay chain, starting with the combination of final state candidates, e.g. $\pi^\pm$ & $K^\pm$ mesons, to intermediate candidates such as the K_S^0 meson that are then further combined to other intermediate or mother candidates, i.e. B^0/ B_s^0 mesons. This approach — referred to as `LoKi Vertex Fitter` (LVF), by its name in the LHCb software framework — is computing time efficient and allows for a reduction of combinatorial background without the need of a full decay chain reconstruction. Therefore, the LVF is the standard approach in the candidate reconstruction of the centralized stripping selection.

However, it may be beneficial to take advantage of correlations between different decay products. This is done by the so called *decay tree fit* (DTF) [100], which has the disadvantage of a higher computing time but on the other hand also offers the possibility to constrain particles of the decay chain to their origin vertex as well as their known mass, thus allowing for a more precise calculation of different decay chain observables. For this analysis, the DTF is used to obtain narrow B_s^0/ B^0 mass distributions with the highest possible resolution in order to maximize the sensitivity on the decays $B_s^0 \to K_S^0 K_S^0$ and $B^0 \to \phi K_S^0$. This is achieved with a DTF setup where the B_s^0/ B^0 candidates are constraint to a PV and the masses of the daughter K_S^0 mesons are constraint to their known masses, as was shown in a study performed in Ref. [6]. If not stated otherwise, the mass observables of the B_s^0/ B^0 mesons used throughout this thesis are a result of this DTF.

3.2.2 Selection Strategy

Signal candidates are selected in a sequence of individual steps, starting from the reconstruction with inputs from the tracking and PID systems of the LHCb detector. As introduced in Section 2.3.2, Page 38, so called ProtoParticles are built by combining tracks and clusters from the calorimeters with PID information. In the centralized stripping, these ProtoParticles are labelled with particle hypotheses and the full decay chain is constructed from bottom to top: at first, final state particles are combined to the intermediate $K_S^0 \to \pi^+\pi^-$ and $\phi \to K^+K^-$ candidates, which are then further combined to B_s^0 and B^0 candidates, respectively. All this is done while successive requirements are made to filter signal-like candidates to reduce background candidates while keeping a maximum signal efficiency. Since these steps are performed in a centralized effort, they are commonly referred to as *online selection*.

In contrast, the individually customized selection, referred to as *offline selection* further reduces background contributions while maximizing the signal to background ratio so that the best possible sensitivity is achieved. The ratio of signal to background candidates is always optimized with a so called *figure of merit* (FoM).

The offline selection itself comprises multiple steps. In a first step, a cut-based preselection is performed, which includes the requirement of DTF convergence and the omission of multiple candidates. The latter is needed because per bunch crossing, multiple proton-proton interactions can happen, which leads to more than one *primary vertex* (PV) per recorded event. A possible selection method for this is to choose the PV based on the fit quality of the corresponding DTF, the so called *best PV selection*. Furthermore, it can occur that more than one signal B_s^0 /B^0 candidate is reconstructed per event, even though this is not expected due to the low branching ratios of the investigated decays. These candidates are also selected by their DTF quality wrt. a given PV, which is referred to as *best candidate selection*. This analysis uses a joint selection of best PV and best B candidate selection. The higher fit quality yields a better mass resolution, which in turn can be exploited by the offline selection and improves the extraction of signal candidates in the final mass fit. After the preselection, the datasets are split according to the respective track categories and requirements on the trigger decisions are made.

The second major part of the offline selection consists of a multivariate classification

to reduce combinatoric background candidates and a cut-based selection to reduce background contributions from other b hadron decays with similar decay components or topologies, comprising cuts on PID observables as well as the separation between B and K^0_S meson vertices. The specific procedures for the second step of the offline selection is explained in detail in Sections 4.1.3 to 4.1.4 for $B^0 \to \phi K^0_S$ and Section 5.1.2 for $B^0_s \to K^0_S K^0_S$, respectively.
The final part of the signal selection involves fits to the distributions of the reconstructed masses from the B mesons as well as from the ϕ meson, in order to extract the number of signal candidates, which are an input for the calculation of the branching ratio, as explained in Section 3.1.

3.2.3 Selection Efficiencies

The accurate determination of the efficiency from each on- and offline selection step is crucial for the correct measurement of the branching ratio, as outlined in Section 3.1. Since it is not possible to distinguish signal from background candidates in the unselected data samples, the efficiencies are calculated from simulation and get assigned systematic uncertainties based on studies on data, see Section 6.2, Page 94. The total efficiency of one channel can be defined as follows:

$$\begin{aligned}\varepsilon_{\text{tot,i}} &= \varepsilon_{\text{gen,i}} \times \varepsilon_{\text{strip\&reco,i|gen,i}} \times \varepsilon_{\text{presel,i|strip\&reco,i}} \times \\ &\quad \varepsilon_{\text{trkcat,i|presel,i}} \times \varepsilon_{\text{trig,i|trkcat,i}} \times \varepsilon_{\text{sel,i|trig,i}} \times \varepsilon_{\text{mva,i|sel,i}}\end{aligned} \tag{3.5}$$

with $i \in \{\text{LL, LD}\}(\{\text{LL, DD}\})$, the track categories of the main (normalisation) channel. In this formula, the pipe in the subscripts outlines that the efficiency is calculated with regard to the latter subscript. Each efficiency is computed separately for each year $\in [2011, 2012, 2015, 2016]$. The efficiencies for Run I (Run II) that are needed for the computation of the normalisation constant, α, are obtained as a weighted mean of the efficiencies in 2011 & 2012 (2015 & 2016) with the integrated luminosity as weights:

$$\begin{aligned}\varepsilon_{\text{s,Run I,t}} &= \frac{\varepsilon_{\text{s,2011,t}} \cdot \mathcal{L}_{\text{int,2011}} + \varepsilon_{\text{s,2012,t}} \cdot \mathcal{L}_{\text{int,2012}}}{\mathcal{L}_{\text{int,2011}} + \mathcal{L}_{\text{int,2012}}} \\ \varepsilon_{\text{s,Run II,t}} &= \frac{\varepsilon_{\text{s,2015,t}} \cdot \mathcal{L}_{\text{int,2015}} + \varepsilon_{\text{s,2016,t}} \cdot \mathcal{L}_{\text{int,2016}}}{\mathcal{L}_{\text{int,2015}} + \mathcal{L}_{\text{int,2016}}}\end{aligned} \tag{3.6}$$

where the index “s” denotes the specific selection stage and the index “t” the track-category, i.e. LL or LD (DD). The individual efficiencies will be described in the following paragraphs.

Generator Level Cut Efficiency

Only a fraction of all signal candidates (either from $B^0 \to \phi K^0_\mathrm{S}$ or $B^0_s \to K^0_\mathrm{S} K^0_\mathrm{S}$ decays) lies within in the geometrical acceptance of the LHCb detector. In simulation, this effect is described by the efficiency ε_gen, which is computed in the centralized production of simulated samples by applying the so called Generator Level Cut and provided by the simulation group of the LHCb experiment.

On- and Offline Selection Efficiencies

In the centralized processing of recorded data, the reconstruction and stripping algorithms reconstruct and select only a certain fraction of signal candidates. This efficiency is denoted as $\varepsilon_\mathrm{reco\&strip}$.
The split into the LL and DD track category subsets is described by the efficiency $\varepsilon_\mathrm{trkcat}$. The cut-based offline selection as well as the multivariate classification applied to the pre-selected datasets in turn omits a certain amount of signal candidates. The corresponding efficiencies are denoted as $\varepsilon_\mathrm{cutsel}$ and ε_mva, respectively.

Trigger Efficiency

From the signal candidates measured in the detector, only a certain fraction leads to a decision of the hard- and software level triggers and is subsequently stored to disc. This is represented by the trigger efficiency $\varepsilon_\mathrm{trig}$. All trigger efficiencies are calculated on simulation. Since it is known, that the L0 efficiency, especially the trigger decision `L0_Hadron_TOS`, is not well described in the simulation, a data-driven approach is used to validate ε_L0, which is further discussed in Ref. [6]. The difference between both approaches is taken as systematic uncertainty, see Section 6.2.
For the Run II subsets of the normalisation channel $B^0 \to \phi K^0_\mathrm{S}$, a special approach is needed because cuts on HLT decisions are already applied at the stripping level, hence making determination of the trigger efficiency impossible. This is solved by computing a combined efficiency for the reconstruction, stripping and trigger step, which is denoted as $\varepsilon_\mathrm{reco\&strip\&trig}$.

3.3 Maximum Likelihood Estimation

The maximum likelihood estimation is a formalism that allows to estimate a set of parameters from an observed data sample by performing a fit of an assumed model to the data points. This is achieved my maximizing the likelihood $\mathcal{L}$ for the model parameters $\vec{\theta}$, given an observed data sample $\boldsymbol{X}$. The data sample consists of m observations, each with n observables, therefore $\boldsymbol{X}$ is an $m \times n$ matrix with $\boldsymbol{X} = [\vec{x}_1, \dots, \vec{x}_m]^T$. In this case, each data point corresponds to a reconstructed $B^0 \to \phi K^0_\mathrm{S}$ or $B^0_s \to K^0_\mathrm{S} K^0_\mathrm{S}$ candidate, respectively, that fulfils the selection criteria. By assuming that $\boldsymbol{X}$ can be described by a *probability density function* (PDF) $\mathcal{P}(\vec{x}|\vec{\theta})$, the likelihood can be written as

$$\mathcal{L}(\vec{\theta}) = \prod_{j}^{m} \mathcal{P}(\vec{x}_j|\vec{\theta})\,. \tag{3.7}$$

Hence, the likelihood describes the probability to observe the given data points, when assuming that $\mathcal{P}(\vec{x}|\vec{\theta})$ describes the distribution of the data points. The best estimators of the parameters $\vec{\theta} = [\theta_1, \dots, \theta_m]^T$ should maximize the likelihood. Thus, they are solutions of

$$\nabla\mathcal{L} = 0\,. \tag{3.8}$$

The resulting PDF $\mathcal{P}(\vec{x}|\vec{\theta}_f)$ represents a fit to the data points. Furthermore, it may be necessary to model different classes in a data sample, e.g. Signal and Background candidates. Then, $\mathcal{P}$ is composed of several individual PDFs $\mathcal{P}_i$, each describing the class i with a yield N_i. The total PDF is hence the superposition:

$$\mathcal{P}(\vec{x}|\vec{\theta}) = \frac{1}{\sum_i N_i} \sum_i N_i \mathcal{P}_i(\vec{x}|\vec{\theta}_i)\,. \tag{3.9}$$

In the case that it is necessary to describe multiple subsamples of one data sample, the PDFs, yields and parameters get an additional label s for the subsamples. Assuming that the individual observations are statistically independent, the extended likelihood function is defined as the probability product of all observations with a Poissonian term for each subset that contains n_s observations:

$$\begin{aligned}\mathcal{L}(\vec{\theta}|\mathbf{X}) &= \prod_s \frac{\mathrm{e}^{-\sum_i N_i^s}}{m_s!} \left(\sum_i N_i\right)^{m_s} \prod_j^{m_s} \frac{\sum_i N_i^s \mathcal{P}_i^s(\vec{x}_j|\vec{\theta}_i^s)}{\sum_i N_i^s} \\ &= \prod_s \frac{\mathrm{e}^{-\sum_i N_i^s}}{m_s!} \prod_j^{m_s} \sum_i N_i^s \mathcal{P}_i^s(\vec{x}_j|\vec{\theta}_i^s)\end{aligned} \tag{3.10}$$

In the analysis presented in this thesis, this extended maximum likelihood function is used in so called mass fits to the reconstructed B^0/ B_s^0/ ϕ mass, respectively, to extract the number of signal candidates in the main and normalisation decay channels.

Since for most cases the maximum of the likelihood cannot be derived analytically, a numerical alternative approach is necessary. A common procedure, which fits most problems, is to consider the logarithm of the likelihood. Then, the best estimators for the parameters can be found by searching a minimum of the negative logarithmic likelihood $-\ln\mathcal{L}(\vec{\theta}|\mathbf{X})$. This is achieved by using the `Minuit` function minimization package [101] that is implemented in the `RooFit` framework [102] and that is also capable of calculating the parameter uncertainties.

3.4 Background Subtraction through Statistical Unfolding

For some studies conducted for this analysis, it is necessary to fully separate signal from background candidates. This is achieved through statistical unfolding with the sPlot [103] technique. The general approach of this method is to find an observable x that can be used to discriminate between signal and background distributions through separate PDFs. Since it often has a distinct shape in the signal and background contributions, the distribution of the reconstructed signal B meson mass is a common choice for this observable. From the results of a preceding extended maximum likelihood fit with signal and background components, so called sWeights can be computed that are then used to unfold the n-th class (see Section 3.3). With the value of the discriminating observable x_i, the sWeights are computed from

$$w_n(x_i) = \frac{\sum_{j=1} V_{nj}\mathcal{P}_j(x_i)}{\sum_{k=1} N_k \mathcal{P}_k(x_i)}\,, \tag{3.11}$$

where the classes are indexed with j and k. The covariance matrix $\boldsymbol{V}$ comprises the covariances between the yields N_k of the classes. The sum of all weights for a given class equals the signal yield obtained in the preceding mass fit. For a background subtracted visualization of the distribution of an arbitrary observable, the sWeights are applied to the corresponding candidates that are then histogrammed. Each bin of the resulting histogram has an uncertainty of

$$\sigma_{\text{bin}} = \sqrt{\sum_{i\in\text{bin}} w_i^2}\,. \tag{3.12}$$

3.5 Simulation and Data Differences

Due to certain approximations in the simulation, some observables in b hadron decays, e.g. the B *transverse momentum* (p_{T}), the *pseudorapidity* (η), and the *track multiplicity* (`nTracks`), as well as detector responses, e.g. the ProbNN values from the PID system or the L0 response are not always accurately described. Although one could expect that discrepancies between simulation and data are similar in the main and the normalisation channel and therefore cancel in the ratio, they could still be worrisome. The effect on the computation of signal efficiencies of the selection steps, as discussed in Section 3.2.3 is estimated by several conservative systematics, see Section 6.2. The On the other hand, the simulation is used as a signal proxy in the training of *boosted decision tree* (BDT) classifiers, see Section 4.1.3, which could alter a classifier's behaviour. One possible solution to this problem is to re- weight the distributions of affected observables with corresponding distributions from signal candidates in real data.[1] These sWeighted distributions are then further used to reweight the distributions of those observables in the simulated datasets. This analysis uses the so called Gradient Boosting reweighting (GB reweighting) [104] for this task. This algorithm uses a *boosted decision tree* (BDT) to obtain weights that can be used for this reweighting by means of the *gradient boosting* [105, 106] algorithm (see Section 4.1.3).

However, the impact of using reweighted simulation for the BDT training turns out to be quite small, see Section 6.2.1. In addition, this approach could lead to additional systematic uncertainties, e.g. through low statistics leading to noticeable uncertainties on the sWeighted distributions which further lead to uncertainties in the kinematic reweighting with the GB reweighting. Therefore, the nominal approach, presented in Section 4.1.3, Page 62, uses the “raw” simulation for the BDT selection in order to avoid any uncertainties resulting from the sPlot and GB reweighting techniques.

In case of the PID observables, this analysis takes an approach common in the LHCb experiment and performs a resampling of the simulated $\pi^{\pm}$ and $K^{\pm}$ ProbNN distributions ProbNNand ProbNNK with the software package PIDGen provided by the LHCb working group PIDCalib [107]. It provides data calibration samples, from which the simulated ProbNN distributions can be resampled in dependency of the p_{T}, , and `nTracks`, which greatly improves the of the ProbNN distributions between simulation and data.

---

[1] As described in Section 3.4, the background subtracted distribution of an arbitrary observable can be obtained by applying per-event-weights, sWeights, which are extracted by means of the sPlot technique from a maximum likelihood fit to the invariant B^0 DTF mass distribution on data.

4 Signal Candidate Selection of $B \to \phi K^0_S$ Decays

This chapter presents the specific steps for the selection of signal candidates for the normalisation channel $B^0 \to \phi K^0_S$, which was the author's main contribution to the analysis. The following sections describe in detail the different stages of the on- and offline selection including the optimisation of selection cuts, see Section 4.1, and the calculation of the selection efficiencies, see Section 4.2. The chapter concludes with an essential result of this thesis, the signal yield extraction of $B^0 \to \phi K^0_S$ decays, shown in Section 4.3. Selection efficiencies and signal yields are a crucial input for the branching ratio determination, discussed in Chapter 6.

4.1 Selection Criteria

The following subsections provide descriptions of the selection criteria applied in the individual selection stages for the normalisation channel. Especially in the reconstruction and stripping steps, the number of possible signal candidates is reduced by requiring that combined intermediate particles are compatible with the physical properties listed in Table 4.1 within a certain range and that they can form common vertices.

Table 4.1 – Physical properties of the individual decay components of the decay $B^0 \to \phi K^0_S$, applied in the selection of the decay $B^0 \to \phi K^0_S$. While the ϕ meson decays instantaneously, the flight distances of the K^0_S and the B^0 meson are $\mathcal{O}(1\,m)$ and $\mathcal{O}(1\,cm)$, respectively. All values are taken from Ref. [20].

Particle	Mass m [MeV/c^2]	Lifetime τ [ps]	
K^0_S	497.614 ± 0.024	89.54 ± 0.04	
$\phi(1020)$	1019.461 ± 0.016	$\mathcal{O}(10^{-10})$	$(\Gamma = (4.249 \pm 0.013)$ MeV)
B^0	5279.63 ± 0.15	1.520 ± 0.004	

4.1.1 Stripping and Preselection

The stripping is the centralized, online preselection of events. Different stripping lines are employed to reflect the different possible track types of the $\pi^\pm$ mesons in the final state, in particular, version 20r1/20 (24r0p1/28) of the already existing Run I (Run II) $B^0 \to K^0_S h^+ h^-$ stripping line `StrippingB2KShh{LL,DD}` (`StrippingB2KShh_{LL,DD}_Run2_OS`). The output of these lines is used for a subsequent reconstruction of $\phi \to K^+K^-$ and a further combination with K^0_S candidates to $B^0 \to \phi K^0_S$ candidates. The specific criteria applied in these stripping lines are listed in Table 4.2 and Table 4.3, for Run I and Run II respectively.

$B^0 \to K^0_S h^+ h^-$ signal candidates are selected in two steps by using centrally preselected input pions: In a first step, K^0_S candidates are combined from input pions. The latter are required to have a χ^2_{IP} above a certain threshold, to minimize the probability that they originate from the PV instead of K^0_S meson decays, and are filtered by means of a minimum momentum. For long track pions, additional cuts on their LVF track fit quality $\chi^2_{\text{track}}/\text{ndf}$ and the probability of them being ghost tracks are made. The LL and DD K^0_S mesons reconstructed from the filtered pions are required to have reconstructed invariant masses in a certain window around the K^0_S *Particle Data Group* (PDG) mass and in addition have to pass LVF fit quality requirements like the χ^2_{vtx} from the K^0_S vertex reconstruction and the χ^2_{FD} of the *flight distance* (FD) reconstruction.

The second step comprises the combination of B^0 which again are required to have a combined invariant mass in a certain window around the B^0 PDG mass. Here, cuts on the χ^2 of the *distance of closest approach* (DOCA), and of the IP, as well as the χ^2_{vtx} of subsequent vertex fits increase the probability that tracks originate from a common vertex, while cuts on the IP make sure that subsidiary particles do not originate from the PV instead. Furthermore, requirements that involve the *transverse momentum* (p_{T}) and the direction angle (DIRA) ensure that particles originate from decays of heavy hadrons. In addition, a cut on the B^0 FD guarantees a good separation of PV and B^0 decay vertex, which helps to reconstruct its decay time e.g. for *CP* violation measurements. In each case, the cuts for the LL lines are tighter compared to the cuts for the DD lines, which corresponds to the better resolution of long tracks.

Table 4.2 – Cuts of the Run I stripping lines `StrippingB2KShh{LL,DD}` for the reconstruction of $B^0 \to K_\mathrm{S}^0 h^+ h^-$ decays, which are used as an input for the reconstruction of $B^0 \to \phi K_\mathrm{S}^0$ decays. The observables are the total momentum p, the *transverse momentum* (p_T), the *impact parameter* (IP). Further observables are the significances of the IP, of the *distance of closest approach* (DOCA), and of endvertex fits, χ^2_IP, χ^2_DOCA and χ^2_vtx, the reconstructed invariant masses of $\pi^+\pi^-$ and $K_\mathrm{S}^0 hh$, $\mathrm{m}_{\pi^+\pi^-}$ and $\mathrm{m}_{K_\mathrm{S}^0 hh}$, and the maximum of the absolute DOCA $\mathrm{max}_\mathrm{DOCA}$. dp stands for the "daughter particles" of the B^0, K_S^0 and $\pi^\pm$. In cases where different cuts are applied for long track or downstream reconstructed K_S^0 mesons, the value in parenthesis refers to the cut for downstream K_S^0's. For the units, $\hbar = c = 1$ is assumed.

Selection step	Particles	Observable	Cut	
$K_\mathrm{S}^0 \to \pi^+\pi^-$	$\pi^\pm$	p	> 2 GeV	
		χ^2_IP	> 9	(> 4)
		$\chi^2_\mathrm{track}/\mathrm{ndf}$	< 4	$(-)$
		ProbNN Ghost	< 0.5	$(-)$
	K_S^0	χ^2_vtx	< 12	
		χ^2_FD	> 80	(> 50)
		$\mathrm{m}_{\pi^+\pi^-}$	$[\mathrm{m}^\mathrm{PDG}_{K_\mathrm{S}^0} \pm 20(30)\ \mathrm{MeV}]$	
		p	–	$(> 6000\ \mathrm{MeV})$
$B^0 \to K_\mathrm{S}^0 h^+ h^-$	K_S^0, h^+, h^-	$\sum p_{\mathrm{T}i}$	$> 3000\ \mathrm{MeV}$	$(> 4200\ \mathrm{MeV})$
		$\mathrm{max}_{\chi^2_\mathrm{DOCA}}$	< 5	
		$\mathrm{m}_{K_\mathrm{S}^0 hh}$	$[\mathrm{m}^{\mathrm{PDG}+921}_{B^0\ \ -1279}\ \mathrm{MeV}]$	
	$\{\mathrm{dp} \mid p_\mathrm{T} > 800\ \mathrm{MeV}\}$	#	≥ 2	
	dp with $\mathrm{max}_{p_\mathrm{T}}$	IP	$> 0.05\,\mathrm{mm}$	
	B^0	p_T	$> 1500\ \mathrm{MeV}$	
		χ^2_vtx	< 12	
		DIRA	> 0.9999	
		χ^2_IP	< 8	(< 6)
		FD	> 1.0	(> 1.7)
		χ^2_FD	> 50	

Table 4.3 – Cuts of the Run II stripping lines `StrippingB2KShh_{LL,DD}_Run2_OS` for the reconstruction of $B^0 \to K^0_\mathrm{S} h^+ h^-$ decays, which are used as an input for the reconstruction of $B^0 \to \phi K^0_\mathrm{S}$ decays. The observables are the total momentum p, the *transverse momentum* (p_T), the *impact parameter* (IP). Further observables are the significances of the IP, of the *distance of closest approach* (DOCA), and of endvertex fits, χ^2_IP, χ^2_DOCA and χ^2_vtx, the reconstructed invariant masses of $\pi^+\pi^-$ and $K^0_\mathrm{S} hh$, $\mathrm{m}_{\pi^+\pi^-}$ and $\mathrm{m}_{K^0_\mathrm{S} hh}$, and the maximum of the absolute DOCA $\mathrm{max}_\mathrm{DOCA}$. dp stands for the "daughter particles" of the B^0, K^0_S and $\pi^\pm$. In cases where different cuts are applied for long track or downstream reconstructed K^0_S mesons, the value in parenthesis refers to the cut for downstream K^0_S's. For the units, $\hbar = c = 1$ is assumed.

Selection step	Particles	Observable	Cut	
$K^0_\mathrm{S} \to \pi^+\pi^-$	$\pi^\pm$	p	> 2 GeV	
		χ^2_IP	> 9	(> 4)
		$\chi^2_\mathrm{track}/\mathrm{ndf}$	$< 4\,\mathrm{mm}$	
		ProbNN Ghost	$< 0.5\,\mathrm{mm}$	$(-)$
	K^0_S	χ^2_vtx	< 12	
		χ^2_FD	> 80	(> 50)
		$\mathrm{m}_{\pi^+\pi^-}$	$[\mathrm{m}^\mathrm{PDG}_{K^0_\mathrm{S}} \pm 20(30)$ MeV$]$	
		p	$-$	$(> 6000$ MeV$)$
$B^0 \to K^0_\mathrm{S} h^+ h^-$	K^0_S, h^+, h^-	$\sum p_{\mathrm{T}i}$	> 3000 MeV	$(> 4200$ MeV$)$
		$\mathrm{m}_{K^0_\mathrm{S} hh}$	$[\mathrm{m}^{\mathrm{PDG}+921}_{B^0\quad -1279}$ MeV$]$	
	h^+, h^-	$\mathrm{max}_{\chi^2_\mathrm{DOCA}}$	< 25	
		$\sum \chi^2_\mathrm{IP}$	> 50	
	$h^\pm$, K^0_S	$\mathrm{max}_{\chi^2_\mathrm{DOCA}}$	< 25	
	K^0_S	ΔZ	> 15	
	$\{\mathrm{dp} \mid p_\mathrm{T} > 800$ MeV$\}$	#	≥ 2	
	B^0	p_T	> 1500 MeV	
		χ^2_vtx	< 12	
		DIRA	> 0.999	
		χ^2_IP	< 8	(< 6)
		χ^2_FD	> 50	

Reconstruction of $B \to \phi K^0_S$ Decays

The output particles of the $B^0 \to K^0_S h^+ h^-$ stripping lines serve as an input for a subsequent offline reconstruction of $B^0 \to \phi K^0_S$ decays. Since the two additional charged hadrons $h^\pm$ have no PID requirements in the preceding stripping, they can now be used to reconstruct $\phi \to K^+ K^-$. To increase the probability that its daughters originated from the same vertex, the resulting ϕ meson has requirements on its χ^2_{vtx} and its reconstructed invariant mass has to be within a certain window around the $\phi(1020)$ meson PDG mass. In addition, cuts on the p and p_{T} of the ϕ meson warrant that the reconstructed ϕ stems from the decay of a heavy mother particle. In a second step, K^0_S and ϕ, whose combined invariant mass lies within a broader window, are combined to B^0 candidates. The final constraint on the χ^2_{vtx} again ensures that daughter particles came from the same vertex. The specific cuts are provided in Table 4.4.

Table 4.4 – Cuts applied in the reconstruction of $B^0 \to \phi K^0_S$ from input particles filtered by the $B^0 \to K^0_S h^+ h^-$ stripping line. The K^0_S mesons are either long or downstream track reconstructed K^0_S mesons. For the units, $\hbar = c = 1$ is assumed.

Decay	Particles	Observable	Cut
$\phi \to K^+ K^-$	ϕ	p_{T}	> 900 MeV
		p	> 1.0 GeV
		χ^2_{vtx}	< 12
		$\text{m}_{K^+K^-}$	$969.445\text{ MeV} < \text{m}_{K^+K^-} < 1069.445\text{ MeV}$
$B^0 \to \phi K^0_S$	K^0_S, ϕ	$\text{m}_{K^0_S \phi}$	$\in [5000\text{ MeV}; 6200\text{ MeV}]$
	B^0	χ^2_{vtx}	< 12

Preselection

Before the actual offline selection, some simple rectangular cuts are applied to further reduce unambiguous background contributions and to make sure that the DTF converged. This includes requirements on the muon PID of the final state particles as well as the best PV and candidate selection explained in Section 3.2.2. The cuts are also listed in Table 4.5 for convenience.

4.1.2 Trigger Requirements

The specific requirements for decisions from the three trigger stages are inspired by trigger selections developed in other LHCb analyses involving ϕ mesons, e.g. the *CP* violation measurement in $B^0_s \to \phi\phi$ [47]. Worth mentioning are the special ϕ trigger lines, as well as the topological trigger lines which are specialized to efficiently trigger on any B meson decay with at least two charged final state particles with cuts on

Table 4.5 – Preselection and sanity cuts applied to candidates of the normalisation channel, $B^0 \to \phi K^0_S$, as well as to candidates of the main channel, $B^0_s \to K^0_S K^0_S$, ahead of the offline selection in order to reduce unambiguous background contributions.

Observable	Cut
isMuon	False for all final state particles ($\pi^\pm$, $K^\pm$)
DTF status	Converged
# PV from DTF	Best PV selection
# Candidates	Best candidate selection

Table 4.6 – Trigger lines and their decisions required in the $B^0 \to \phi K^0_S$ selection. Between the respective trigger stages, an AND operation is inserted. For Run II, the HLT trigger selection is required in the stripping and not offline.

<table>
<tr><th>Stage</th><th>Run I</th><th>Run II</th></tr>
<tr><td>L0</td><td colspan="2">HadronDecision_TOS OR Global_TIS</td></tr>
<tr><td>HLT1</td><td>TrackAllL0Decision_TOS</td><td>TrackMVADecision_TOS
OR TwoTrackMVADecision_TOS
OR IncPhiDecision_TOS
OR PhiIncPhiDecision_TOS</td></tr>
<tr><td>HLT2</td><td>IncPhiDecision_TOS
OR Topo2BodyBBDTDecision_TOS
OR Topo3BodyBBDTDecision_TOS
OR Topo4BodyBBDTDecision_TOS</td><td>IncPhiDecision_TOS
OR PhiIncPhiDecision_TOS
OR Topo2BodyDecision_TOS
OR Topo3BodyDecision_TOS
OR Topo4BodyDecision_TOS</td></tr>
</table>

topological observables like the p_{T}, FD, or IP as well as corresponding χ^2 values. By also allowing K^0_S mesons as input particles, the trigger efficiency of $B \to XK^0_S$ decays is increased by $\approx 5\,\%$ [108]. All triggers are required to have triggered only on signal candidates (TOS), the only exception being the global L0 decision which is required to trigger independently of signal candidates (TIS).

4.1.3 Multivariate Classification

For decays with a fully hadronic final state reconstructed in a hadronic environment, the separation of signal from combinatoric background is a crucial part in the selection. In this analysis, this is achieved by employing a *boosted decision tree* (BDT), which is able to predict the target category of an event by using a set of observables, so called *features*, and applying binary decision rules at each node of the decision tree, hereby performing a binary classification of the investigated candidates into the categories signal and background. In general, the rules for each node are inferred by providing category-labelled data to a supervised learning algorithm. The algorithm operates top-down and chooses in each step the feature that best separates the available set of events.

The *boosting* of decision trees is a way to greatly improve the classification accuracy and is based on the principle of an ensemble: boosting algorithms iteratively build an ensemble of decision trees by adding a new tree in each iteration that helps to improve the classification of items misclassified by the trees in previous iterations. The final BDT classifier is obtained from a weighted mean of all trained decision trees. There exist a number of different approaches to boosting algorithms, one example being *gradient boosting* [105, 106] that is based on the minimization of an arbitrary loss function with the gradient descent algorithm. In this analysis, the XGBoost library is used to perform the gradient boosting.

Following the logic behind the measurement of relative branching ratios, it would be a good thing to have the same BDTs for main and normalisation channel so that systematic uncertainties of this selection step cancel in the ratio. However, this is not possible in the case of this analysis. Because of the special decay topology of the $B_s^0 \to K_S^0 K_S^0$ decay — one neutral mother particle decaying into two neutral long-lived particles — the BDT trained for the main channel $B_s^0 \to K_S^0 K_S^0$ relies heavily on features that correlate different observables of the two K_S^0 so that the separation power is maximised. Since these features are not available for the $B^0 \to \phi K_S^0$ channel it is not possible to use the same BDT here.

In order to account for kinematic differences, separate BDTs are trained for the data subsets Run I LL/DD and Run II LL/DD, where corresponding simulation samples are used as a signal proxy while the background proxy consists of candidates from data with a reconstructed B^0 mass well above the signal region, $m > 5600\,\mathrm{MeV}/c^2$. This ensures that the background samples consist mainly of combinatoric background candidates with no underlying signature that could be learned by the BDT and hence disturb the classification.

Each BDT is constructed and trained after the following iterative approach to improve the classification accuracy and to minimize the probability of over- training:

1.) First, the set of features is chosen from kinematic / topological observables and their χ^2 values from the decay chain fits, e.g. χ^2_{FD} and χ^2_{IP}. In the process, it is ensured that none of the selected input features is correlated to the invariant mass of the B^0 meson because this would bias the classifier.

2.) For the chosen set of features, the optimal number of trees is determined.

3.) In this and the next step, the final set of input features is selected. First, the importance of each feature, i.e. the number of times a specific feature is used for a split normalised with the number of trees, is calculated.

4). Now, the optimal number of features can be determined in an iterative way.

5.) In the final step, the classifier for a given subset is trained with the parameters established in the previous steps, e.g. the number of trees and optimised list of features.

The optimal number of trees is computed by retraining the BDT ensemble iteratively with more and more trees, until no improvement in its performance is observed. A common way to quantify the performance is the area under the *receiver operating characteristic* (ROC) curve, abbreviated as ROC AUC. The ROC curve applies the true positive rate against the false positive rate or in other words the signal efficiency versus the background retention.
For the selection of the final input features, the subset is first divided into one testing sample and two training samples. After the training procedure, the feature importance is then calculated on the test sample. This procedure is performed ten times, each time with a new split of training and testing samples, to receive a robust decision. Afterwards, the whole set of features is ordered after their importance.
Now follows the iterative determination of the final set of input feature. In each iteration, a three-folding cross validation is applied: The subset is split into three equally sized folds. For each fold, a classifier is trained with one training sample and validated on the other two testing samples. The final classifier is obtained as the average of all three classifiers. Then, the ROC AUC score for each test sample is computed and the mean and its uncertainty is stored to a graph. The least important feature is removed from the list of input features. The iteration stops, when only two features are left. The optimal number of features can then be chosen from the complete graph at the point where the ROC AUC score does not improve significantly with a larger number of features. Section 4.1.3 illustrates the rising ROC AUC score for increasing number of input features and a saturation effect above a certain number of features. This leads to the conclusion to take into account 7 (5) and 9 (10) features for Run I (Run II) LL and DD, respectively. The final set of features for each subset is listed in Table 4.7.
For the training of the final BDT classifier, a three-folding cross validation combined with XGboost's *early stopping* function[1] is deployed in order to avoid over-fitting by using too many decision trees in the training.
Fig. 4.1 shows some examples of BDT features for the Run I LL subset. As discussed above, all features are of topological nature, including the B^0 p_{T}, B^0 decay time τ, B^0 pseudorapidity η, and the *flight distances* (FDs) as well as the *impact parameters* (IPs), both wrt. the PV, of multiple particles. Furthermore, the fit quality features IP χ^2, and the χ^2 value of the decay vertex (Endvertex) fit normalised to the number of degrees of freedom are features with a good separation between signal and background. The observable $\Delta Z \equiv \mathrm{Endvertex}_z(K^0_\mathrm{S}) - \mathrm{Endvertex}_z(B^0)$, which is also used for the

---

[1] The early stopping function prevents the boosting algorithm from adding more decision trees if there was no improvement in the ROC AUC score of the testing sample over the last 25 added trees.

reduction of physical background, see Section 4.1.4 is able to reject (combinatoric) background from hadrons that originate from the B^0 decay vertex and are misidentified as a long track K^0_{S}. Finally, the observable $\min\{\Delta\chi^2_{\text{vtx}}\}_{+1\text{ track}}$ describes the change in the χ^2_{vtx} when adding one additional long track before reconstructing the B^0 vertex.
As can be seen in Section 4.1.3 (and Appendix A.1), the trained classifiers succeed in the classification of signal and background candidates. The specific cut points for the classifiers are determined with an optimisation on the basis of the *figure of merit* (FoM)

$$\frac{S}{\sqrt{S+B}} \tag{4.1}$$

with the number of signal candidates, S, and the number of background candidates, B, which yields in an optimal signal-significance, see Section 4.1.3. To retain a minimum number of signal events after the cut, the cut point optimisation is performed with additional constraint of a minimum signal efficiency off $\varepsilon_{\text{sig}} \geq 0.8$ for the Run I DD subset. The final cut points for the classifiers (clf) are:

$$\begin{aligned} &\left.\begin{aligned} \text{clf}_{\text{LL}} &> 0.489 \\ \text{clf}_{\text{DD}} &> 0.466 \end{aligned}\right\}\text{Run1} \\ &\left.\begin{aligned} \text{clf}_{\text{LL}} &> 0.652 \\ \text{clf}_{\text{DD}} &> 0.596 \end{aligned}\right\}\text{Run2} \end{aligned} \tag{4.2}$$

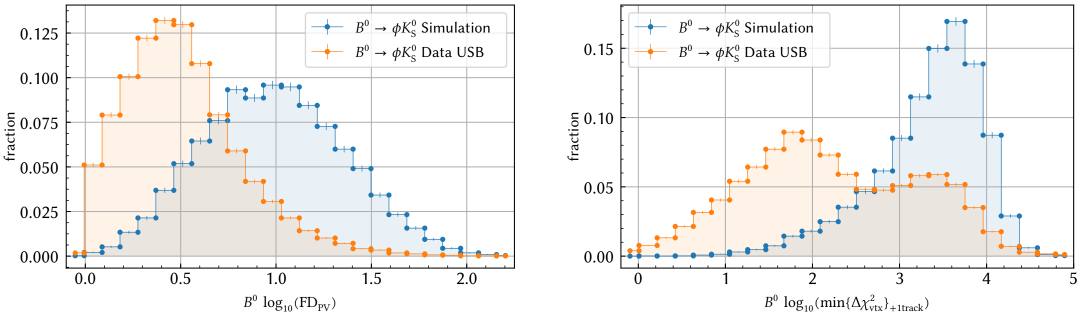

Figure 4.1 – Distributions of BDT input features for the Run I LL subset with a high separation power between simulated signal candidates (blue) and background candidates from the upper mass-sideband (USB), $m > 5600\,\text{MeV}/c^2$, of stripped data in (orange). The features shown are the B^0 FD wrt. the PV, and $\min\{\Delta\chi^2_{\text{vtx}}\}_{+1\text{ track}}$, which describes the change in the χ^2_{vtx} when adding one additional long track before reconstructing the B^0 vertex.

4.1.4 Physical Backgrounds and Particle Identification

After reducing combinatorial background to a minimum with the BDT selection, physical background contributions from decay channels like $B^0 \to K^0_S h^+ h^-$ could still be present.
In order to reduce physical background from PID misidentification, different distributions of PID observables were studied. The most effective has proven to be the maximum of the ProbNNπ values of the two kaons from $\phi \to K^+K^-$

$$\max\{K^{\pm}\text{ProbNN}\pi\} \equiv \max(K^{+}\text{ProbNN}\pi, K^{-}\text{ProbNN}\pi).$$

The upper plot in Fig. 4.3 shows the distributions of this observable in simulation on the one hand and upper and lower mass sidebands ($\text{m}_{B^0} < 5250\,\text{MeV}/c^2 \,||\, \text{m}_{B^0} > 5450\,\text{MeV}/c^2$), i.e. of background candidates. By cutting on this observable, all kaon pairs were even one of both might rather be a pion are sorted out. The optimal cut point is again found by means of an optimisation of the $S/\sqrt{S+B}$ FoM.
Since the classifier output and $\max\{K^{\pm}\text{ProbNN}\pi\}$ are uncorrelated (see Fig. A.5) the optimisations of the XGBoost classifiers and PID observables can be performed independently. Fig. 4.3, bottom, shows the PID cut point optimisation for the Run I LL subset. The determined cut points are:

$$\left.\begin{aligned} \max\{K^{\pm}\text{ProbNN}\pi\}_{\text{LL}} &< 0.40 \\ \max\{K^{\pm}\text{ProbNN}\pi\}_{\text{DD}} &< 0.24 \end{aligned}\right\} \text{Run I}$$

$$\left.\begin{aligned} \max\{K^{\pm}\text{ProbNN}\pi\}_{\text{LL}} &< 0.87 \\ \max\{K^{\pm}\text{ProbNN}\pi\}_{\text{DD}} &< 0.85 \end{aligned}\right\} \text{Run II}$$

Furthermore, background contributions from decays where two hadrons from the B^0 decay vertex are misidentified as a LL K^0_S can be rejected with a cut on the observable

$$\Delta Z \equiv \text{Endvertex}_z(K^0_S) - \text{Endvertex}_z(B^0), \tag{4.3}$$

since real K^0_S mesons have a certain separation from the B^0 decay vertex, see upper plot in Fig. 4.4. This cut is not necessary for K^0_S mesons that are reconstructed from downstream pions because they have a significant flight distance and therefore a large ΔZ compared to said background. In case of the Run II subsets, the ΔZ cut is already applied in the stripping step (see Table 4.3, Page 60) and is therefore not applied again in the offline selection. In this case too, the cut point for ΔZ is determined with an optimisation by means of the $S/\sqrt{S+B}$ FoM, which is shown in the lower plot of Fig. 4.4. The resulting cut for the Run I LL subset is:

$$(\Delta Z)_{\text{Run I LL}} > 23.82. \tag{4.4}$$

Table 4.7 – Features included in the multivariate classification process of $B^0 \rightarrow \phi K^0_\mathrm{S}$, split by dataset subsets. One result of the feature selection process is that a logarithmic transformation of some features improves their separation power. The features are the reconstructed *flight distances* (FDs) and *impact parameters* (IPs) wrt. the PV as well as the IP χ^2, the χ^2 value normalised to the number of degrees of freedom, χ^2/ndf of the decay vertex (Endvertex) fit and the kinematic observables of the B^0 meson: *transverse momentum* (p_T), *decay time* (τ) and the *pseudorapidity* (η). Furthermore, the observable $\Delta Z = \mathrm{Endvertex}_z(K^0_\mathrm{S}) - \mathrm{Endvertex}_z(B^0)$ is especially useful to reject (combinatoric) background from hadrons that originate from the B^0 decay vertex and are misidentified as a long track K^0_S. The last not yet mentioned observable, $\min\{\Delta\chi^2_\mathrm{vtx}\}_{+1\ \mathrm{track}}$ describes the change in the χ^2_vtx when adding one additional long track before reconstructing the B^0 vertex. The index PV denotes that the observable was calculated wrt. the primary vertex.

		Run I		Run II	
Feature	Particle	LL	DD	LL	DD
$\log_{10}(\mathrm{FD_{PV}})$	B^0	✓	✓	✓	✓
$\log_{10}(\mathrm{Endvertex}\ \chi^2/\mathrm{ndf})$	B^0	✗	✓	✓	✓
$\log_{10}(\chi^2_\mathrm{IP,PV}/\mathrm{ndf})$	B^0	✗	✓	✗	✓
$\log_{10}(\min\{\Delta\chi^2_\mathrm{vtx}\}_{+1\ \mathrm{track}})$	B^0	✓	✗	✗	✗
p_T	B^0	✓	✓	✗	✓
η	B^0	✓	✓	✓	✗
τ	B^0	✗	✗	✗	✓
ΔZ	B^0, K^0_S	✓	✗	✗	✗
$\log_{10}(\mathrm{Endvertex}\ \chi^2/\mathrm{ndf})$	ϕ	✓	✓	✓	✓
$\log_{10}(\mathrm{IP_{PV}})$	ϕ	✗	✓	✓	✓
$\log_{10}(\mathrm{FD_{PV}})$	ϕ	✗	✗	✓	✓
$\log_{10}(\chi^2_\mathrm{IP,PV}/\mathrm{ndf})$	ϕ	✓	✓	✗	✓
$\log_{10}(\mathrm{IP_{PV}})$	K^0_S	✗	✓	✗	✓
$\log_{10}(\chi^2_\mathrm{IP,PV}/\mathrm{ndf})$	K^0_S	✗	✓	✓	✗

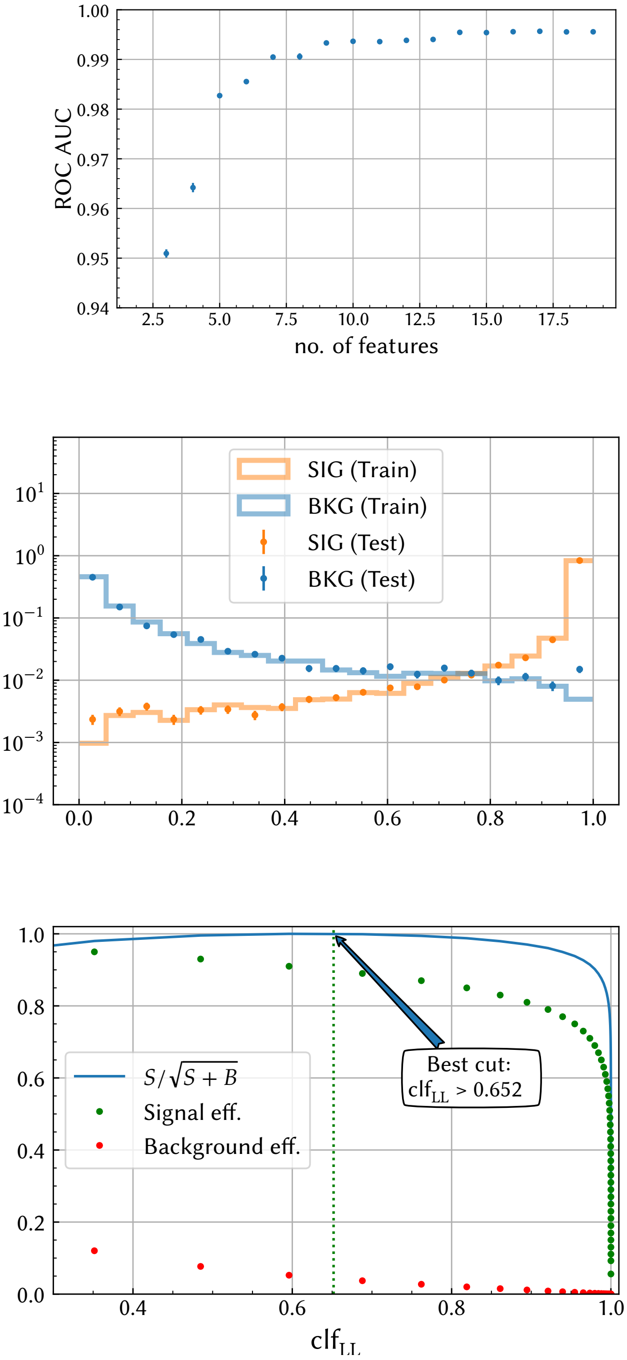

Figure 4.2 – Shown here are plots that outline the different stages of the multivariate selection, using the example of the Run II LL subset. Plots of the other subsets can be found in Appendix A.1. Top: The number of features taken from the ranked feature list vs. the ROC AUC score obtained with this set of features. Middle: The output of the XGBoost classifiers for training and testing datasets showing a good classification into signal (SIG) and background (BKG). Bottom: Cut point optimisation for the cut on the XGBoost classifier with a FoM.

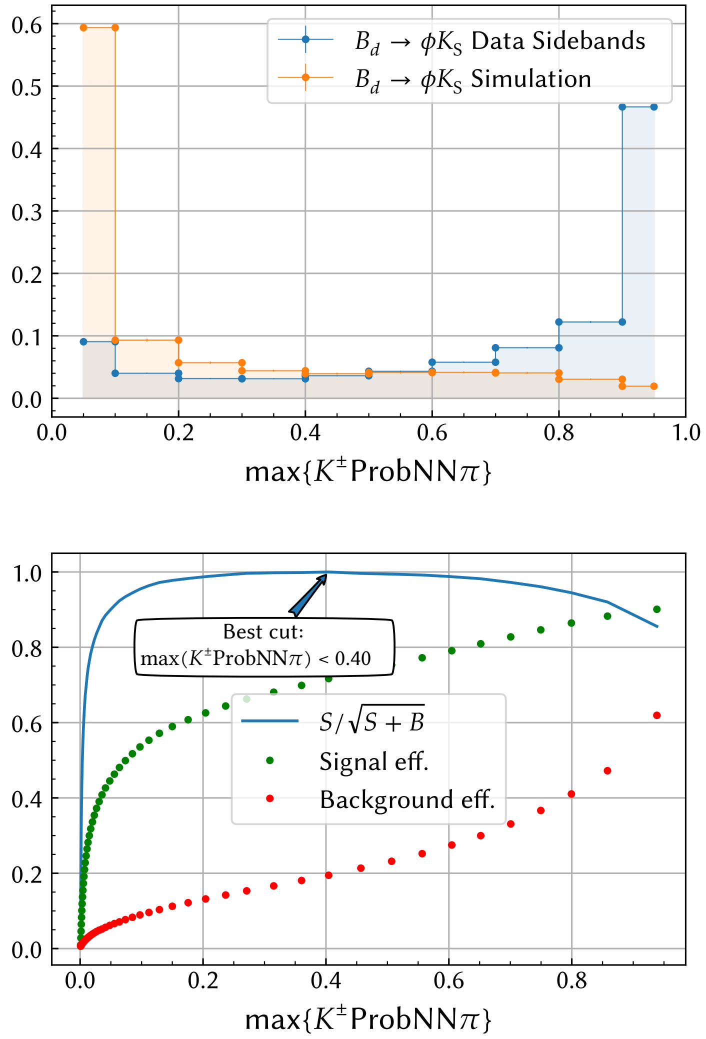

Figure 4.3 – PID selection plots using the example of the Run I LL dataset. Top: Distribution of the PID observable max{$K^{\pm}$ProbNNπ} in simulation (orange) and data sidebands ($m_{B^0} < 5250\,\text{MeV}/c^2 \,||\, m_{B^0} > 5450\,\text{MeV}/c^2$) (blue) for the Run I LL subset. Bottom: Cut point optimisation of the variable max{$K^{\pm}$ProbNNπ} on the Run I LL subset, by means of the $S/\sqrt{S+B}$ FoM.

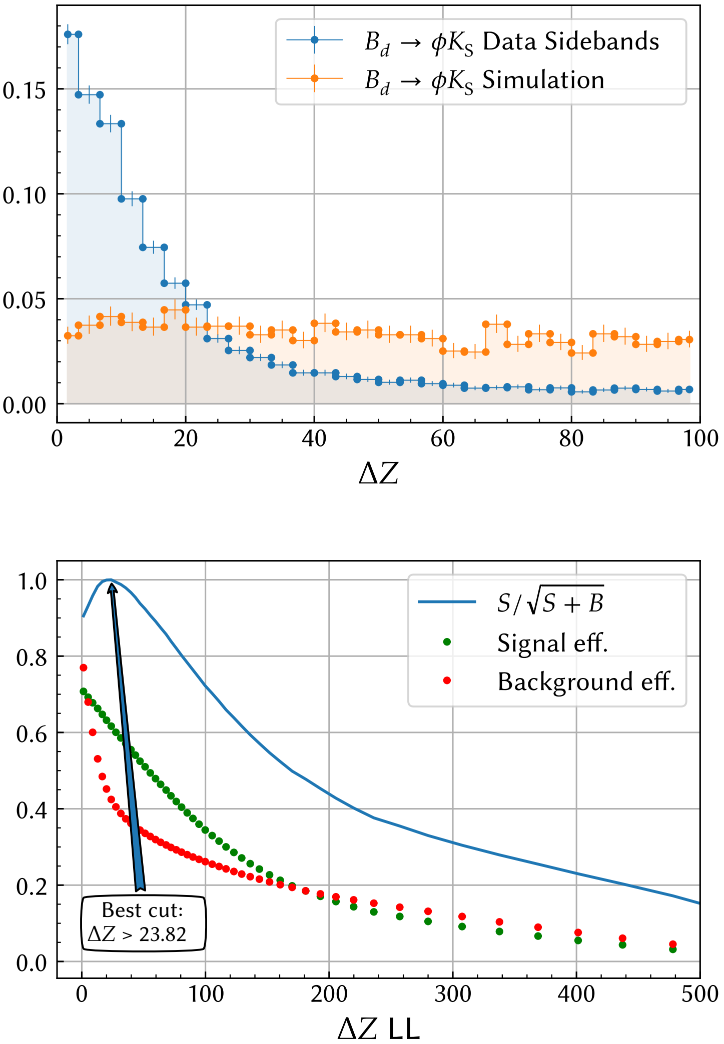

Figure 4.4 – Top: Distribution of the observable ΔZ for long track K^0_S mesons in Run I simulation (orange) and background data (blue). Bottom: Cut point optimisation of the observable ΔZ for the Run I LL dataset by means of a signal-significance FoM, $S/\sqrt{S+B}$.

4.2 Selection Efficiencies

As discussed in Section 3.1, the total selection efficiencies of the different subsets are needed as an input for the computation of the branching ratio $\mathcal{B}(B_s^0 \to K_S^0 K_S^0)$ normalised to the branching ratio $\mathcal{B}(B^0 \to \phi K_S^0)$. This section discusses the individual components as well as the results for the total selection efficiencies.
A list of all efficiencies of the individual selection steps is given in Table 4.8 for each subset of the normalisation channel. The notation for the efficiencies is described in Section 3.2.3, Page 51. The efficiencies for Run I (Run II) are computed as a weighted mean of the efficiencies in 2011 & 2012 (2015 & 2016) with the integrated luminosity of a given year as weights, as shown in Eq. (3.6), Section 3.2.3. When comparing the efficiencies of the individual selection steps for the Run I and Run II subsets, it becomes apparent that the offline selection efficiencies, i.e. the cut-based selection efficiency, $\varepsilon_{\text{cutsel}}$, and the efficiency for the multivariate classification, ε_{mva}, have been improved for the Run II subsets. However, this is outweighed by the 60–70 % lower $\varepsilon_{\text{reco\&strip\&trig}}$ efficiencies in Run II compared to Run I:

$$\frac{\varepsilon_{\text{reco\&strip\&trig,Run II LL}}}{\varepsilon_{\text{reco\&strip\&trig,Run I LL}}} = 0.603 \pm 0.007\,,$$
$$\frac{\varepsilon_{\text{reco\&strip\&trig,Run II DD}}}{\varepsilon_{\text{reco\&strip\&trig,Run I DD}}} = 0.728 \pm 0.006\,,$$

where $\varepsilon_{\text{reco\&strip\&trig,Run I}} = \varepsilon_{\text{reco\&strip,Run I}} \cdot \varepsilon_{\text{trig,Run I}}$. This effect can be explained by the fact that the cuts of the used `StrippingB2KShh_{LL,DD}_Run2_OS` stripping line (see Table 4.2 and Table 4.3) were not optimised to account for the different conditions prevailing in Run II. This effect is propagated to the total selection efficiencies, calculated after Eq. (3.5), which therefore show comparable results for the Run I and Run II efficiencies:

$$\begin{aligned}
\varepsilon_{\phi K_S^0,\text{Run I LL}} &= (2.922 \pm 0.029) \cdot 10^{-4}\,,\\
\varepsilon_{\phi K_S^0,\text{Run I DD}} &= (5.03 \pm 0.04) \cdot 10^{-4}\,,\\
\varepsilon_{\phi K_S^0,\text{Run II LL}} &= (2.600 \pm 0.027) \cdot 10^{-4}\,,\\
\varepsilon_{\phi K_S^0,\text{Run II DD}} &= (5.34 \pm 0.04) \cdot 10^{-4}. \qquad (4.5)
\end{aligned}$$

For a comparison of the LL and DD results, it has to be taken into account that the efficiencies $\varepsilon_{\text{trkcat}}$, describing the split into $\approx \frac{1}{3}$ LL candidates and $\approx \frac{2}{3}$ DD candidates, are included in these results. Overall, the total efficiencies are in good agreement with those obtained by other LHCb analyses that used the decay $B^0 \to \phi K_S^0$ as a normalisation channel, e.g. the observation of the decay $\Lambda_b^0 \to \Lambda\phi$ [109]. However, it can be concluded that future measurements in the decay $B^0 \to \phi K_S^0$ can profit from optimised stripping cuts, and moreover from specialized trigger lines, designed for the detection of long-lived neutral particles like the K^0_S.

Table 4.8 – All Run I and Run II selection efficiencies for the normalisation channel $B^0 \to \phi K^0_\mathrm{S}$. Note the different notations in the two tables due to the trigger filter in the Run II stripping lines (see Section 3.2.3).

Efficiencies	Run I	
ε_gen	0.2660	± 0.0004
$\varepsilon_\mathrm{reco\&strip}$	0.022 12	± 0.000 05
$\varepsilon_\mathrm{presel}$	0.9306	± 0.0006
$\varepsilon_\mathrm{trkcat,LL}$	0.3077	± 0.0011
$\varepsilon_\mathrm{trkcat,DD}$	0.6923	± 0.0011
$\varepsilon_\mathrm{trig,LL}$	0.2507	± 0.0019
$\varepsilon_\mathrm{trig,DD}$	0.2162	± 0.0012
$\varepsilon_\mathrm{cutsel,LL}$	0.7582	± 0.0033
$\varepsilon_\mathrm{cutsel,DD}$	0.7556	± 0.0025
$\varepsilon_\mathrm{mva,LL}$	0.9105	± 0.0021
$\varepsilon_\mathrm{mva,DD}$	0.8127	± 0.0020

Efficiencies	Run II	
ε_gen	0.2707	± 0.0007
$\varepsilon_\mathrm{reco\&strip\&trig,,LL}$	0.003 347	± 0.000 028
$\varepsilon_\mathrm{reco\&strip\&trig,,DD}$	0.003 479	± 0.000 021
$\varepsilon_\mathrm{presel}$	0.9316	± 0.0008
$\varepsilon_\mathrm{trkcat,LL}$	0.3347	± 0.0016
$\varepsilon_\mathrm{trkcat,DD}$	0.6653	± 0.0016
$\varepsilon_\mathrm{cutsel,LL}$	0.9765	± 0.0014
$\varepsilon_\mathrm{cutsel,DD}$	0.9742	± 0.0017
$\varepsilon_\mathrm{mva,LL}$	0.9453	± 0.0018
$\varepsilon_\mathrm{mva,DD}$	0.9381	± 0.0024

4.3 Mass Parametrisation and Signal Yield Extraction

The final step of the signal candidate selection is the parametrisation of the reconstructed B^0 DTF mass distribution with a *probability density function* (PDF) as described in Section 3.3, in order to extract the number of signal candidates present in the individual subsets. The complete PDF for the B^0 mass consists of one component to describe the signal and one to describe remaining combinatoric background contributions,

$$N_{\text{tot}}\mathcal{P}_{\text{tot}} = N_{\text{sig}}\mathcal{P}_{\text{sig}} + N_{\text{bkg}}\mathcal{P}_{\text{bkg}} \quad , \tag{4.6}$$

which are discussed in Section 4.3.1. Furthermore, the reconstructed B^0 mass might be polluted with contributions from the non-resonant decay channel $B^0 \to K^+K^-K^0_S$, as explained in Section 1.3.1, Page 22. This effect is described with an additional parametrisation of the reconstructed ϕ mass, comprising one PDF for the signal contribution and one PDF to describe the non-resonant K^+K^- contribution. The final signal yield of the normalisation channel is then retrieved as the signal yield corrected by the non-resonant yield.

A possible bias on the retrieved signal yields and the fit model itself are considered as a systematic uncertainties, see Section 6.2. They are studied in detail in Ref. [6].

4.3.1 Parametrisation of the Reconstructed B^0 Mass Distribution

The signal component of the B^0 DTF mass distribution is parametrised with a so called Hypatia PDF [110], which is a common choice in LHCb analyses nowadays. The Hypatia, which is marginalized over the unknown per-event resolution of the mass, is a generalized Crystal ball PDF [111], which was historically introduced to describe lossy processes, e.g. through photon emission.

The general form is:

$$\mathcal{P}_{\text{sig}}(m;\mu,\sigma,\lambda,\zeta,\beta,a_1,n_1,a_2,n_2) \propto \begin{cases} ((m-\mu)^2 + A_\lambda^2(\zeta)\sigma^2)^{\frac{1}{2}\lambda-\frac{1}{4}} e^{\beta(m-\mu)} K_{\lambda-\frac{1}{2}}\left(\zeta\sqrt{1+\left(\frac{m-\mu}{A_\lambda(\zeta)\sigma}\right)^2}\right) & , -a_1 < \frac{m-\mu}{\sigma} < a_2 \\ \frac{G(\mu-a_1\sigma,\mu,\sigma,\lambda,\zeta,\beta)}{\left(1-m/\left(n\frac{G(\mu-a_1\sigma,\mu,\sigma,\lambda,\zeta,\beta)}{G'(\mu-a_1\sigma,\mu,\sigma,\lambda,\zeta,\beta)}-a_1\sigma\right)\right)^{n_1}} & , -a_1 > \frac{m-\mu}{\sigma} \\ \frac{G(\mu-a_2\sigma,\mu,\sigma,\lambda,\zeta,\beta)}{\left(1-m/\left(n\frac{G(\mu-a_2\sigma,\mu,\sigma,\lambda,\zeta,\beta)}{G'(\mu-a_2\sigma,\mu,\sigma,\lambda,\zeta,\beta)}-a_2\sigma\right)\right)^{n_2}} & , \quad a_2 < \frac{m-\mu}{\sigma}, \end{cases} \tag{4.7}$$

where G' is the derivative of the generalized hyperbolic distribution

$$G(m;\mu,\sigma,\lambda,\zeta,\beta) = ((m-\mu)^2 + A_\lambda^2(\zeta)\sigma^2)^{\frac{1}{2}\lambda-\frac{1}{4}} e^{\beta(m-\mu)} K_{\lambda-\frac{1}{2}}\left(\zeta\sqrt{1+\left(\frac{m-\mu}{A_\lambda(\zeta)\sigma}\right)^2}\right), \tag{4.8}$$

containing the cylindrical harmonics K_λ, and

$$A_\lambda^2(\zeta) = \frac{\zeta K_\lambda(\zeta)}{K_{\lambda+1}(\zeta)}. \tag{4.9}$$

The hyperbolic core of the PDF is described by the mean, μ, the width, σ, and the additional parameter λ. It is extended by power-law- tails to both sides, which depend on the parameters a_1, a_2, n_1 , and n_2. The parameters ζ and β are set to zero. All shape parameters are determined from fits to the individual simulation subsets, which are scaled to 1000 (2000) candidates for LL (DD) in order to prevent over-fitting, see Fig. 4.5. The parameters are fixed in the fit to data, except for the width, in order to account for differences in the mass resolution between simulation and data. As discussed in Section 3.2.1, the fit observable is the B^0 DTF mass with additional constraints to the PV and the K^0_S PDG mass. Furthermore, by requiring $5150 < m(K^+K^-K^0_S) < 5600\,\text{MeV}/c^2$ partially reconstructed decays at lower masses are cut out.

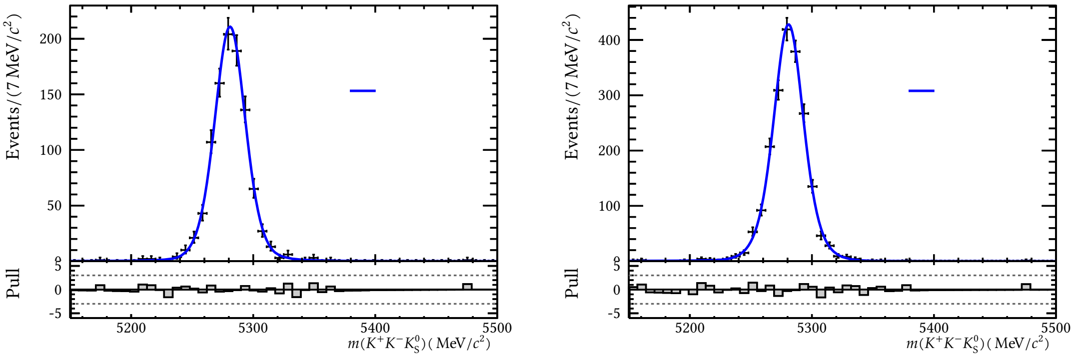

(a) Run I LL

(b) Run I DD

Figure 4.5 – Fit of the Hypatia PDF to the simulated B^0 mass distribution with DTF constraints on the K^0_S mass and the PV for the Run I LL (left) and DD (right) subsets. The candidates in the simulated dataset are scaled to 1000 (2000) candidates for the LL (DD) subset, in order to prevent over-fitting. For Run II LL/DD see Fig. A.7.

The background contributions remaining in the B^0 mass after applying the full selection chain is presumably of combinatoric nature. Hence, its shape is described with an exponential PDF of the form:

$$\mathcal{P}_{\text{bkg}} = \exp^{-\kappa m} . \tag{4.10}$$

The parameter κ is retrieved in the fit to the specific data subsets.
The final fit to the B^0 DTF mass distribution for the Run I LL data subset is shown in Fig. 4.6. Signal and background contributions are well modelled by the chosen PDF. Table 4.9 shows the obtained signal and background yields, N_{sig} and N_{bkg}, as well as the PDF parameters. This fit is also used to extract the sWeights, which are needed to correct for the non-resonant background contribution in the ϕ mass. This is discussed in the following subsection. Furthermore, Table 4.10 shows the ratio of widths, r_σ, from the fits on data and simulation subsets, which is used for the mass parametrisation of the B_s^0 meson in the main channel, $B_s^0 \to K_S^0 K_S^0$, for the fits on data, see Section 5.3.

Table 4.9 – Fit parameters of the B^0 mass PDF for the normalisation channel $B^0 \to \phi K_S^0$.

Parameter	Run I LL	Run I DD	Run II LL	Run II DD	Status
N_{sig}	140 ± 13	250 ± 27	156 ± 18	360 ± 32	free
a_1	2.1 ± 0.5	2.12 ± 0.25	1.2 ± 0.8	1.2 ± 0.8	fixed
a_2	3.2 ± 0.9	3.8 ± 0.5	2.1 ± 1.0	2.1 ± 1.0	fixed
λ	-0 ± 70	-2 ± 6	-2.0 ± 1.5	-2.0 ± 1.5	fixed
μ [MeV/c^2]	5281.0 ± 0.5	5280.80 ± 0.33	5280.6 ± 0.5	5280.6 ± 0.5	fixed
n_1	2.7 ± 1.6	3.8 ± 1.5	6 ± 4	6 ± 4	fixed
n_2	3.0 ± 2.8	0.9 ± 0.7	6 ± 6	6 ± 6	fixed
σ [MeV/c^2]	16.8 ± 1.5	23.7 ± 3.1	16.2 ± 2.2	25.2 ± 2.6	free
ζ	2.5 ± 1.2	3.9 ± 1.7	0 ± 5	0 ± 5	fixed
N_{bkg}	79 ± 11	508 ± 31	405 ± 24	1060.0 ± 40.0	free
κ_{bkg}	$-9 \pm 11 \cdot 10^{-4}$	$-9 \pm 11 \cdot 10^{-4}$	$-8 \pm 5 \cdot 10^{-4}$	$-8 \pm 5 \cdot 10^{-4}$	free

Table 4.10 – The ratio of Hypatia widths, r_σ, from the fits of the Hypatia PDF on data and simulation subsets.

	Run I LL	Run I DD	Run II LL	Run II DD
r_σ	1.14 ± 0.12	1.68 ± 0.23	0.94 ± 0.14	1.70 ± 0.20

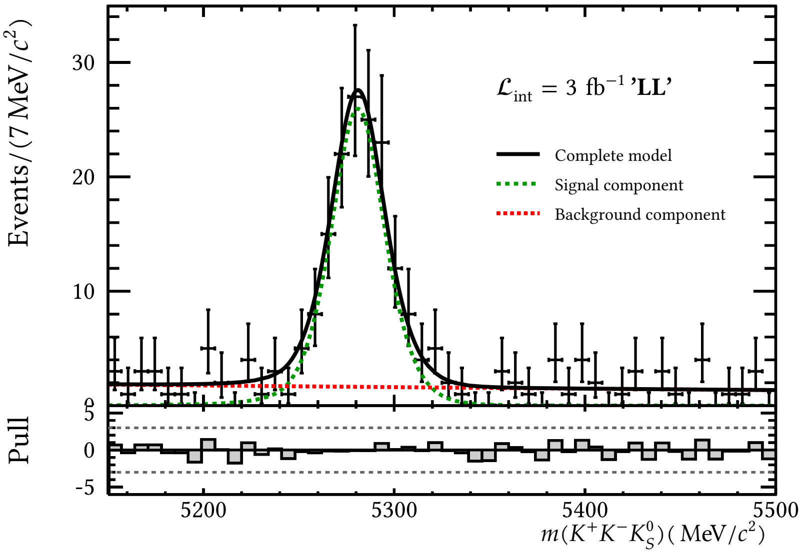

(a) Run I LL

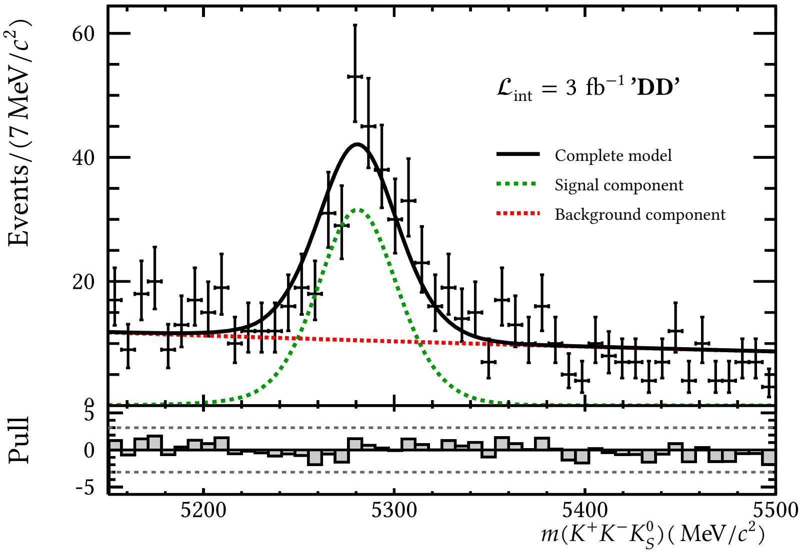

(b) Run I DD

Figure 4.6 – Fit to the B^0 DTF mass distribution with DTF K^0_S mass and PV constraints for the (a)/(b) Run I LL/DD subset.

4.3.2 Non-resonant Background Contributions

To correct for non-resonant K^+K^- contributions in the ϕ mass, a PDF consisting of two components is fitted to the sWeighted ϕ mass distribution, as was done before in LHCb analyses having dealt with ϕ mesons, e.g. Ref. [47]. The component for the signal shape is a relativistic Breit-Wigner [112] convoluted with a Gaussian resolution model, which has two parameters: a shift $\Delta\mu$ wrt. the Breit-Wigner mean μ and a width σ. The relativistic Breit-Wigner is defined as [112]:

$$F_{\mathrm{BW}}(\mathrm{m}_{K^+K^-}) = \frac{\mu \mathrm{m}_{\phi}\Gamma}{(\mathrm{m}_{\phi}{}^2 - \mu^2)^2 + \mathrm{m}_{\phi}{}^2\Gamma^2} \tag{4.11}$$

with

$$\Gamma = \Gamma_0 \frac{\mathrm{m}_\phi}{\mu} \left(\sqrt{\frac{\mathrm{m}_{K^+K^-}{}^2 - 4m_K^2}{\mathrm{m}_\phi{}^2 - 4m_K^2}} \right)^3 , \tag{4.12}$$

where m_K and m_ϕ denote the masses of the $K^\pm$ and the ϕ mesons, respectively, and Γ_0 the natural width of the resonance. The component for the non-resonant background is described with a phase-space of the form

$$\mathit{PS}(m) = \frac{m^2 - (2m_K)^2}{m^2} , \tag{4.13}$$

where m is the invariant K^+ K^- mass and m_K the $K^\pm$ mass. The complete PDF is first fitted to simulation, where the parameters m_K and Γ_0 are fixed to the PDG values of the $K^\pm$ mass and the ϕ meson width. The phase-space model parameters m and m_K are also fixed to the PDG values of the ϕ and $K^\pm$ masses, respectively. Fig. 4.7 shows the suitability of the chosen model. All PDF parameters are listed in Table 4.11. The retrieved shape parameters μ, $\Delta\mu$, and σ are fixed in the fit to sWeighted data. Hence, only the associated yields $N_{\mathrm{sig,corr}}$ and $N_{\mathrm{non-reso}}$ are left floating.
The fit to the sWeighted ϕ mass distribution is shown in Fig. 4.8 for the Run I subsets. The PDF is found to describe the distributions well. The corresponding fit parameters are given in Table 4.12. For the computation of the relative branching ratio, the corrected signal yield $N_{\mathrm{sig,corr}}$ is taken as an input in order to account for the contributions of non-resonant K^+K^- background:

$$\begin{aligned} N_{\text{sig,corr, Run I LL}} &= 122 \pm 16 \\ N_{\text{sig,corr, Run I DD}} &= 235 \pm 22 \\ N_{\text{sig,corr, Run II LL}} &= 134 \pm 17 \\ N_{\text{sig,corr, Run II DD}} &= 316 \pm 26 \,. \end{aligned} \tag{4.14}$$

Table 4.11 – Shape parameters of the PDF describing the reconstructed ϕ mass, obtained from fits to simulation subsets.

Parameter	Run I LL	Run I DD	Run II LL	Run II DD
μ [MeV/c^2]	1019.50 ± 0.26	1019.5 ± 0.9	1020.00 ± 0.11	1019.00 ± 0.07
$\Delta\mu$ [MeV/c^2]	−0.03 ± 0.25	−0.03 ± 0.25	0.05 ± 0.04	0.026 ± 0.007
σ [MeV/c^2]	1.16 ± 0.17	1.235 ± 0.021	1.006 ± 0.017	1.0070 ± 0.0013

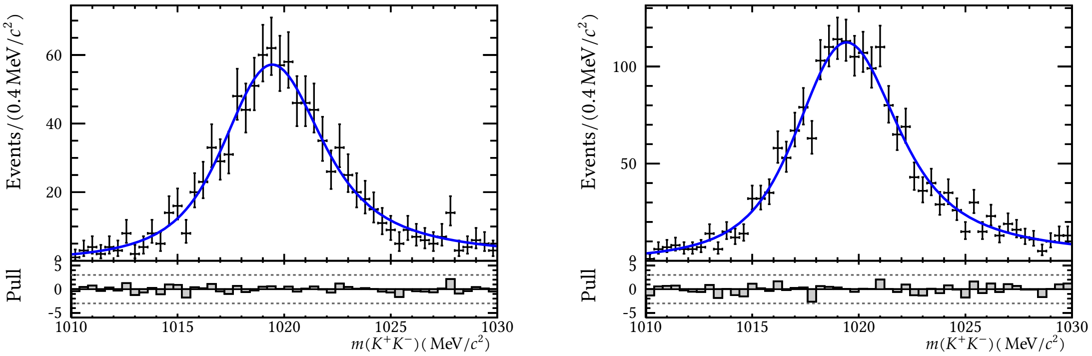

(a) Run I LL

(b) Run I DD

Figure 4.7 – Fit to the simulated invariant K^+K^- mass distribution for the (a)/(b) Run I LL/DD subset. The candidates in the simulated dataset are scaled to 1000 (2000) candidates for LL (DD), in order to prevent over-fitting. Figure A.9 shows the corresponding plots for the Run II subsets.

Table 4.12 – Fit parameters of the PDF describing the reconstructed ϕ mass, fitted to the sWeighted invariant K^+K^- mass distribution in the different data subsets.

Parameter	Run I LL	Run I DD	Run II LL	Run II DD	Status
$N_{\mathrm{sig,corr}}$	122 ± 16	235 ± 22	128 ± 17	270 ± 25	free
$N_{\mathrm{non-reso}}$	18 ± 13	14 ± 16	27 ± 13	90 ± 21	free
μ [MeV/c^2]	1019.50	1019.5	1020.00	1019.00	fixed
$\Delta\mu$ [MeV/c^2]	-0.03	-0.03	0.05	0.026	fixed
σ [MeV/c^2]	1.16	1.235	1.006	1.0070	fixed

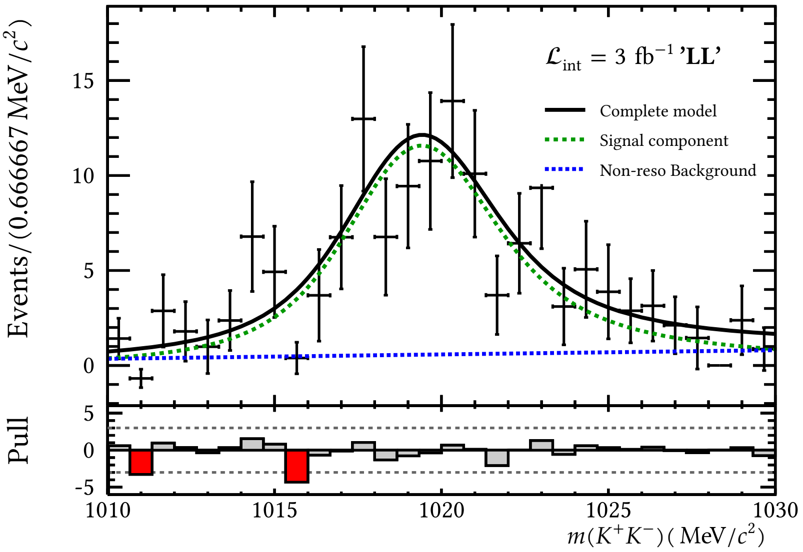

(a) Run I LL

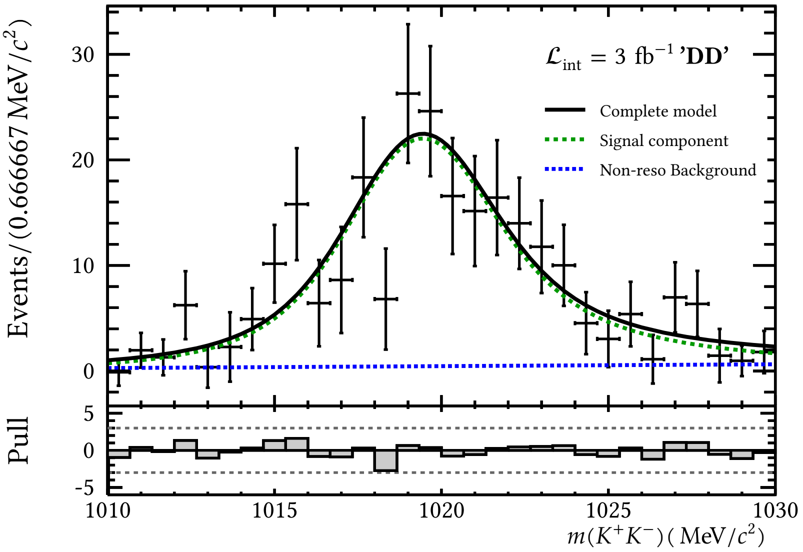

(b) Run I DD

Figure 4.8 – Fit to the sWeighted invariant K^+ K^- mass distribution for the (a)/(b) Run I LL/DD subsets. The corresponding plots for the Run II subsets can be found in Fig. A.10.

5 Signal Candidate Selection of $B_s^0 \to K_S^0 K_S^0$ Decays

This chapter summarises the selection steps for the selection of signal candidates of the main channel $B_s^0 \to K_S^0 K_S^0$ for a complete picture of the analysis. A more detailed discussion will be presented in Ref. [6]. The different stages of the on- and offline selection are shortly described in the following sections, see Section 5.1. The chapter concludes with the parametrisation of the reconstructed B_s^0 mass, see Section 5.3, in preparation of the branching ratio determination presented in the subsequent chapter.

5.1 Selection Criteria

The following subsections provide descriptions of the selection criteria applied in the individual selection stages for the main channel. In order to reduce systematic uncertainties, the selection is performed in a similar way as for the normalisation channel. However, the challenging decay topology of this decay, i.e. the decay into two neutral long-lived intermediate particles and the absence of a characteristic signature of the $\phi \to K^+K^-$ final state, leading to a lower expected signal yields, demands a more cautious approach in some cases.
In the first steps, the reconstruction and stripping, subsequent requirements on the physical properties of combined intermediate and mother particles, shown in Table 5.1, lower the number of possible signal candidates.

Table 5.1 – Physical properties of the individual decay components of the decay $B_s^0 \to K_S^0 K_S^0$, used in the selection of the decay $B_s^0 \to K_S^0 K_S^0$. While the ϕ meson decays instantaneously, the flight distances of the K_S^0 and the B_s^0 meson are $\mathcal{O}(1\,m)$ and $\mathcal{O}(1\,cm)$, respectively. All values are taken from Ref. [20].

Particle	Mass m [MeV/c^2]	Lifetime τ [ps]
K_S^0	497.614 ± 0.024	89.54 ± 0.04
B_s^0	5366.89 ± 0.19	1.527 ± 0.011

5.1.1 Stripping, Preselection and Trigger Requirements

As was done for the normalisation channel, different stripping lines, corresponding to the track categories LL, LD and DD (see Section 3.1) are used in the centralized preselection of the decay $B_s^0 \to K_S^0 K_S^0$, namely version 20r1/20 of the stripping line `StrippingBs2KSKS{LL,LD,DD}` for data recorded in 2011/2012 and versions 24r0p1/28 of the lines `StrippingBs2KSKS{LL,LD,DD}_Run2` for data recorded in 2015/2016. A detailed list of stripping cuts is given in Table 5.2 and Table 5.3, for Run I and Run II respectively. In addition to the observables and applied cuts that can also be found in the stripping selection of the normalisation channel, see Section 4.1.1, the $B_s^0 \to K_S^0 K_S^0$ stripping lines employ cuts on the maximum of the absolute *distance of closest approach* (DOCA) in the combination of K_S^0 and B_s^0 mesons. These cuts increase the probability that the tracks of their daughter particles originated from the same vertex. Furthermore, the main difference between the stripping lines for Run I and Run II is the employment of a BDT classifier the Run I stripping line cut. Since this was inefficient in terms of computing time and resources, the new self-made Run II stripping line refrained from the use of a BDT classifier.

Analogous to the normalisation channel, the same preselection cuts are applied before the offline selection to ensure the convergence of the DTF and to reduce unambiguous background contributions, see Table 4.5.

The required trigger decisions are also similar to the trigger selection applied in Section 4.1.2, but with the important difference that the efficient ϕ trigger lines cannot be used and that two different combinations of trigger lines are used: The trigger category T_L that triggers on long tracks and the loose category T_D, which is not optimised. The corresponding trigger requirements are listed in Table 5.4. However, a data-driven study conducted in Ref. [6] shows that the T_D trigger category and therefore the whole DD subset cannot be taken into account for the determination of the $B_s^0 \to K_S^0 K_S^0$ branching ratio for two reasons: The first one is the low trigger efficiency of 0.021 ± 0.005 / 0.0253 ± 0.0075 for the Run I/ 2016 subset, respectively. In addition, there exists no suitable normalisation channel for the DD subset, which should have two intermediate long-lived (neutral) particles that have the ability to be reconstructed from downstream tracks only and decay to hadronic final states in order to mimic the $B_s^0 \to K_S^0 K_S^0$ decay topology. This excludes decay channels like $B^0 \to K_S^0 h^+ h^-$ and $B^0 \to \phi K_S^0$.

Table 5.2 – Run I stripping line cuts for $B_s^0 \to K_S^0 K_S^0$ decays. The observables are the total momentum p, the transverse momentum p_T, the significance of the impact parameter (IP), distance of closest approach (DOCA) and end vertex fits χ^2_{IP}, χ^2_{DOCA} and χ^2_{vtx}, mass windows of the invariant $\pi^+ \pi^-$ and K_S^0 K_S^0 mass $m_{\pi^+\pi^-}$ and $m_{K_S^0 K_S^0}$, the maximum of the absolute DOCA $\max_{DOCA}$ and finally an output of a boosted decision tree. Some of these cuts are only applied on subsets of the data, split after the K_S^0 track categories. For the units, $\hbar = c = 1$ is assumed.

Decay	Particle	Observable	Cut
$K_S^0 \to \pi^+\pi^-$	$\pi^\pm$	p_T	> 250 MeV
(long track)		$\min_{\chi^2_{IP}}(PV)$	> 4
		p	$> 2,$ GeV
		χ^2_{IP}	> 9
	K_S^0	χ^2_{DOCA}	< 25
		χ^2_{vtx}	< 25
		$m_{\pi^+\pi^-}$	$[m^{PDG}_{K_S^0} \pm 35$ MeV$]$
		$\max_{DOCA}$	< 1 mm
$K_S^0 \to \pi^+\pi^-$	π^+	p	> 2 GeV
(downstream)		χ^2_{IP}	> 4
	K_S^0	χ^2_{DOCA}	< 25
		χ^2_{vtx}	< 25
		$m_{\pi^+\pi^-}$	$[m^{PDG}_{K_S^0} \pm 64$ MeV$]$
		$\max_{DOCA}$	< 4 mm
$B_s^0 \to K_S^0 K_S^0$	B_s^0	$m_{K_S^0 K_S^0}$	$[m^{PDG}_{B_s^0} \pm 600$ MeV$]$
(LL)		BDT output	> 0.5
		$\max_{DOCA}$	< 1 mm
$B_s^0 \to K_S^0 K_S^0$	B_s^0	$m_{K_S^0 K_S^0}$	$[m^{PDG}_{B_s^0} \pm 600$ MeV$]$
(LD/DD)		BDT output	> 0.5
		$\max_{DOCA}$	< 4 mm

Table 5.3 – Run II stripping line cuts for $B_s^0 \to K_S^0 K_S^0$ decays. The observable are the total momentum p, the transverse momentum p_T, the minimum impact parameter significance in respect to the primary vertex $\min_{\chi^2_\mathrm{IP}}(PV)$, the track significance over number of degrees of freedom $\chi^2_\mathrm{track}/\mathrm{ndf}$, the probability for a track to be just noise in the detector ProbNN Ghost, the significance of the impact parameter (IP), distance of closest approach (DOCA) and end vertex fits χ^2_IP, χ^2_DOCA and χ^2_vtx, mass windows of the invariant π^+ π^- and K_S^0 K_S^0 mass $\mathrm{m}_{\pi^+\pi^-}$ and $\mathrm{m}_{K_S^0 K_S^0}$, the maximum of the absolute DOCA $\max_\mathrm{DOCA}$. Some of these cuts are only applied on subsets of the data, split after the K_S^0 track categories. For the units, $\hbar = c = 1$ is assumed.

Decay	Particle	Observable	Cut
$K_S^0 \to \pi^+\pi^-$ (long track)	$\pi^\pm$	$\min_{\chi^2_\mathrm{IP}}(PV)$	> 4 MeV
		$\chi^2_\mathrm{track}/\mathrm{ndf}$	< 4
		p_T	> 250 MeV
		ProbNN Ghost	< 0.5
	π^+	p	> 2 GeV
		χ^2_IP	> 9
	K_S^0	χ^2_IP	> 5
		χ^2_DOCA	$< 25\,\mathrm{mm}$
		χ^2_vtx	< 25
		$\mathrm{m}_{\pi^+\pi^-}$	$[\mathrm{m}^\mathrm{PDG}_{K_S^0} \pm 35$ MeV$]$
$K_S^0 \to \pi^+\pi^-$ (downstream)	$\pi^\pm$	$\min_{\chi^2_\mathrm{IP}}(PV)$	> 4 MeV
		$\chi^2_\mathrm{track}/\mathrm{ndf}$	< 4
	π^+	p	> 2 GeV
		χ^2_IP	> 4
	K_S^0	χ^2_IP	> 5
		χ^2_DOCA	$< 25\,\mathrm{mm}$
		χ^2_vtx	< 25
		$\mathrm{m}_{\pi^+\pi^-}$	$[\mathrm{m}^\mathrm{PDG}_{K_S^0} \pm 64$ MeV$]$
$B_s^0 \to K_S^0 K_S^0$ (LL)	B_s^0	$\mathrm{m}_{K_S^0 K_S^0}$	$\in [4000$ MeV$; 6500$ MeV$]$
		$\max_\mathrm{DOCA}$	$< 1\,\mathrm{mm}$
$B_s^0 \to K_S^0 K_S^0$ (LD/DD)	B_s^0	$\mathrm{m}_{K_S^0 K_S^0}$	$\in [4000$ MeV$; 6500$ MeV$]$
		$\max_\mathrm{DOCA}$	$< 4\,\mathrm{mm}$

Table 5.4 – Trigger lines applied in the $B_s^0 \to K_S^0 K_S^0$ selection. The two trigger categories T_L and T_D are optimized on long track and downstream K_S^0, respectively. Between the individual trigger stages, an `AND` operation is inserted. Note that the HLT2 lines allow for at most one downstream K_S^0.

Conf.	Stage	Run I	Run II
T_L	L0	`HadronDecision_TOS OR Global_TIS`	
	HLT1	`TrackAllL0Decision_TOS`	`TrackMVADecision_TOS` `OR TwoTrackMVADecision_TOS`

	HLT2	`Topo2BodyBBDTDecision_TOS`
		`OR Topo3BodyBBDTDecision_TOS`
		`OR Topo4BodyBBDTDecision_TOS`
			`Topo2BodyDecision_TOS`
			`OR Topo3BodyDecision_TOS`
			`OR Topo4BodyDecision_TOS`

T_D	L0	`HadronDecision_TOS OR Global_TIS`	
	HLT1	`Phys_TIS`	`Phys_TIS`
	HLT2	`Phys_TIS`	`Phys_TIS`

5.1.2 Offline Selection

Physical Background Contributions

Because of the challenging decay topology, it is crucial to identify possible physical background contributions that could distort the signal yield. Physical background candidates are on the one hand decays where one or more particle is not reconstructed in the decay chain leading to the same final state as the signal decay and on the other hand decays were final state particles get assigned a wrong particle hypothesis, again leading to a final state equal to the signal decay final state. Fig. 5.1 shows an overview of possible background contributions that were reconstructed with a four pion mass hypothesis, simulated with the `RapidSim` software package [113], which uses a simplified model to quickly generate decay candidates without considering possible resonances. Of the shown decays, the decays $\Lambda_b^0 \to p K_S^0 \pi^-$ and $B_s^0 \to K_S^0 \pi^\pm K^\pm$ contribute to the signal through misidentification of the final state proton / kaon as a pion, respectively. By requiring that the combined invariant mass of the misidentified particle and the final state pion should be within a certain range around the K_S^0 mass under the pion-pion hypothesis suppresses both background contributions by a factor for $\sim$ 100. Figure 5.2 shows the reconstructed invariant masses for the two decays together with the applied K_S^0 mass window. Remaining background from the decays $B_s^0 \to K_S^0 \pi^\pm K^\pm$ and $B^0 \to K_S^0 h^+ h^-$ are further reduced by a cut on the observable

$$\Delta Z \equiv \mathrm{Endvertex}_z(K_S^0) - \mathrm{Endvertex}_z(B_s^0) > 5. \tag{5.1}$$

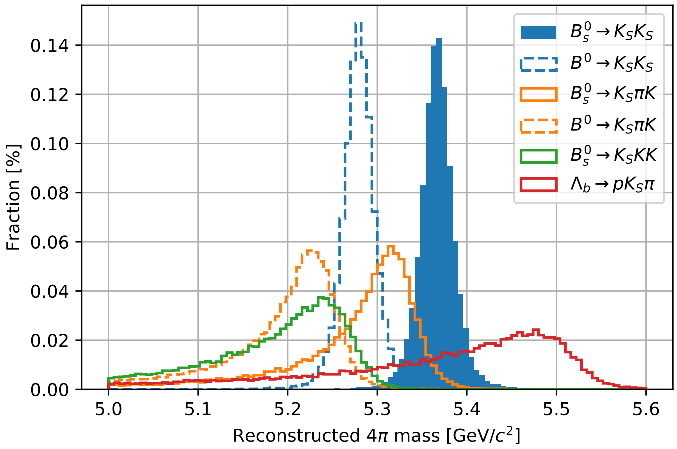

Figure 5.1 – Mass distributions of possible physical background contributions for the decay $B_s^0 \to K_S^0 K_S^0$, simulated with the `RapidSim` package [113]. The invariant masses have been calculated using a four pion mass hypothesis. Figure taken from Ref. [6].

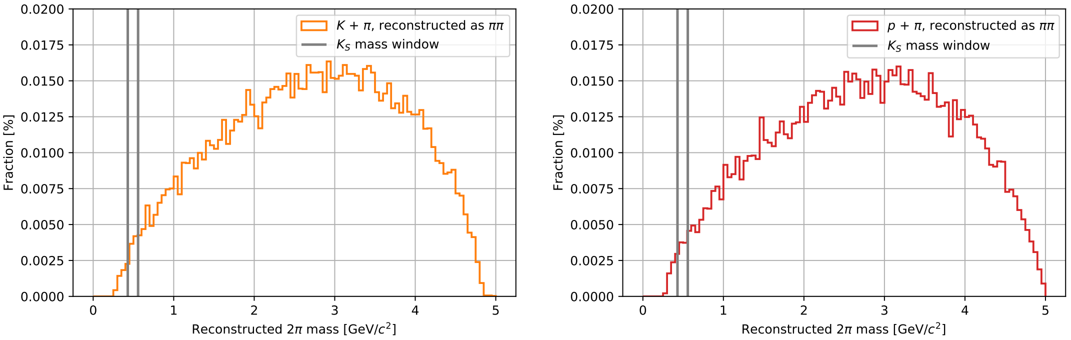

Figure 5.2 – Invariant masses of kaon-pion and proton-pion under the pion-pion mass hypothesis of the decays $B_s^0 \rightarrow K_S^0\pi^{\pm}K^{\pm}$ (left) and $\Lambda_b^0 \rightarrow pK_S^0\pi^-$ (right), respectively. Additionally, the K_S^0 mass window is added to these plots. Figure taken from Ref. [6].

Multivariate Classification

The reduction of combinatoric background is an important part for the main channel, due to its ambiguous decay topology and the four-pion final state. Analogous to the normalisation channel, this is achieved through a multivariate classification with gradient boosted decision tree which follows the same optimisation process for the BDT construction and training as presented in Section 4.1.3. The BDTs are trained on the track category subsets where simulation is used as the signal proxy while data from the upper mass side band ($5600 to 6000\,\mathrm{MeV}/c^2$) is used as a background proxy. The final set of features used for the classification are listed in Table 5.5. It becomes apparent that the BDTs for the individual subsets of the decay $B_s^0 \rightarrow K_S^0K_S^0$ rely heavily on topological observables like flight distance and impact parameter as well as features that correlate different observables of the two K_S^0's in order maximize the separation power.

PID Selection and Combined Cut Point Optimisation

For further reduction of physical background from PID misidentification, the minimum of the ProbNNvalue of the four final state pions,

$$\min\{\pi_1^{\pm}\mathrm{ProbNN}\pi, \pi_2^{\pm}\mathrm{ProbNN}\pi\}, \tag{5.2}$$

where $\pi_1^{\pm}$ ($\pi_2^{\pm}$) are the daughter particles of the first (second) K_S^0, is chosen as the discriminating observable. The cut points of each data subset are optimised together with the BDT classifier output in a two dimensional cut point optimisation. In contrast to the normalisation channel, the Punzi [114] figure of merit is used, which is defined

Table 5.5 – Features included in the multivariate classification process of $B_s^0 \to K_S^0 K_S^0$, split by dataset subsets. One result of the feature selection process is that a logarithmic transformation of some features improves their separation power. The features that apply a min or max operation on K_S^0 observables are only using K_S^0 pairs with the same track type, i.e. only LL. The listed features use the kinematic observables *total momentum* (p), *transverse momentum* (p_T), *decay time* (τ), and *pseudorapidity* (η) as well as the topological observables *impact parameter* (IP), *flight distance* (FD), and the corresponding χ^2 values. The index PV denotes that the observable was calculated wrt. the primary vertex.

		Run I		Run II	
Feature	Particle	LL	LD	LL	LD
η	B_s^0	✗	✗	✓	✓
τ	B_s^0	✓	✓	✓	✓
$\log_{10}(p)$	B_s^0	✗	✗	✓	✓
$\log_{10}(p_T)$	B_s^0	✓	✓	✗	✗
$\log_{10}(\max\{\chi^2_{\mathrm{IP,PV}}\})$	B_s^0	✓	✓	✓	✓
Endvertex χ^2/ndf)	B_s^0	✓	✓	✓	✓
$\mathrm{FD_{PV}}$	B_s^0, K_S^0 (LD)	✗	✓	✓	✓
$\mathrm{IP_{PV}}$	B_s^0, K_S^0 (LD)	✗	✗	✓	✓
$\log_{10}(\max\{\chi^2_{\mathrm{IP,PV}}\})$	K_S^0 (LL)	✗	✗	✓	✗
$\log_{10}(\chi^2_{\mathrm{IP,PV}})$	K_S^0 (LD)	✗	✓	✗	✓
$\max\{\chi^2_{\mathrm{FD,PV}}\}$	K_S^0 (LL)	✗	✗	✓	✗
$\max\{\mathrm{IP_{PV}}\}$	K_S^0 (LL)	✗	✗	✓	✗
$\min\{\mathrm{IP_{PV}}\}$	K_S^0 (LL)	✗	✗	✓	✗

as

$$\frac{\varepsilon_{\mathrm{sig}}}{3/2 + \sqrt{B}}, \tag{5.3}$$

with the signal efficiency, $\varepsilon_{\mathrm{sig}}$ and the number of background candidates, B. Since it takes into account the signal efficiency, this FoM is ideal for searches of rare decays. In the cut point optimisation an additional cut on the K_S^0 mass is applied to further reduce combinatorial background contributions. To guarantee a robust fit, a minimum of 10 background candidates outside the signal region have to pass the optimised cut points. The final cut points are listed in Table 5.6.

Table 5.6 – Optimised PID and BDT cut point values applied in the selection of the decay $B_s^0 \to K_S^0 K_S^0$.

Dataset	$\min\{\pi_1^{\pm}\text{ProbNN}\pi, \pi_2^{\pm}\text{ProbNN}\pi\}$ cut	Classifier cut
Run I LL	>0.15	>0.78
Run I LD	>0.30	>0.76
Run II LL	>0.15	>0.92
Run II LD	>0.16	>0.91

5.2 Selection Efficiencies

In addition to the selection efficiencies for the normalisation channel, the main channel's selection efficiencies are also included in the calculation of the branching ratio.
The individual efficiencies were also determined on simulation, with the only difference that the selection efficiencies for the stripping step could be evaluated separately from the reconstruction step. This is due to special simulation samples for the main channel, which are produced with a stripping filtering step in order to enrich the number of signal candidates in the simulation samples. Hence, it is possible to determine the number of candidates passing the stripping filter step that is equal to the stripping efficiency.
All selection efficiencies are listed in Table 5.7. Some major differences can be spotted between the efficiency for Run I and Run II. While the stripping efficiency $\varepsilon_{\text{strip}}$ drops due to the removal of the efficient BDT selection in the stripping line, the trigger efficiency $\varepsilon_{\text{trig}}$ rises because the rectangular cuts in stripping and trigger selection complement each other well. However, the product of $\varepsilon_{\text{strip}}$ and $\varepsilon_{\text{trig}}$ stays roughly the same. The total selection efficiencies are calculated to:

$$\begin{aligned}
\varepsilon_{K_S^0K_S^0,\text{Run I LL}} &= (0.680 \pm 0.023) \cdot 10^{-5}\,, \\
\varepsilon_{K_S^0K_S^0,\text{Run I LD}} &= (0.987 \pm 0.027) \cdot 10^{-5}\,, \\
\varepsilon_{K_S^0K_S^0,\text{Run II LL}} &= (2.324 \pm 0.020) \cdot 10^{-5}\,, \\
\varepsilon_{K_S^0K_S^0,\text{Run II LD}} &= (4.053 \pm 0.026) \cdot 10^{-5}. \qquad (5.4)
\end{aligned}$$

Overall, the total selection efficiencies profit from the increased fraction of LL and LD candidates in Run II, described by the track category efficiencies $\varepsilon_{\text{trkcat,\{LL,LD,DD\}}}$. From kinematic considerations, one would expect a larger number of downstream track K_S^0 mesons, due to the higher centre-of-mass energy. However, a study presented in Ref. [6] shows that the trigger selection plays an important role in the selection of long track and downstream particles, leading to the observed ratio of LL and LD candidates presented here.

Table 5.7 – All selection efficiencies for the main channel $B_s^0 \to K_S^0 K_S^0$ for Run I and Run II.

Efficiencies	Run1		Run2	
ε_{gen}	0.145 01	± 0.000 28	0.1586	± 0.0005
$\varepsilon_{\text{strip}}$	0.058 09	± 0.000 04	0.028 399	± 0.000 017
$\varepsilon_{\text{reco}}$	0.8596	± 0.0004	0.641 30	± 0.000 29
$\varepsilon_{\text{presel}}$	0.932 00	± 0.000 30	0.928 53	± 0.000 19
$\varepsilon_{\text{trkcat,LL}}$	0.041 01	± 0.000 24	0.114 57	± 0.000 25
$\varepsilon_{\text{trkcat,LD}}$	0.2907	± 0.0006	0.4712	± 0.0004
$\varepsilon_{\text{trkcat,DD}}$	0.6683	± 0.0006	0.4142	± 0.0004
$\varepsilon_{\text{trig,LL}}$	0.0515	± 0.0011	0.1039	± 0.0007
$\varepsilon_{\text{trig,LD}}$	0.007 68	± 0.000 17	0.068 05	± 0.000 28
$\varepsilon_{\text{cutsel,LL}}$	0.898	± 0.009	0.8963	± 0.0021
$\varepsilon_{\text{cutsel,LD}}$	0.723	± 0.010	0.8946	± 0.0012
$\varepsilon_{\text{mva,LL}}$	0.524	± 0.012	0.8362	± 0.0026
$\varepsilon_{\text{mva,LD}}$	0.765	± 0.012	0.5338	± 0.0019

5.3 Mass Parametrisation

The parametrisation of the reconstructed B_s^0 DTF mass follows the same approach that was pursued for the normalisation channel. The complete PDF comprises one component to model the signal and one to model remaining combinatoric background contributions,

$$N_{\text{tot}}\mathcal{P}_{\text{tot}} = N_{\text{sig}}\mathcal{P}_{\text{sig}} + N_{\text{bkg}}\mathcal{P}_{\text{bkg}}, \tag{5.5}$$

where $\mathcal{P}_{\text{sig}}$ and $\mathcal{P}_{\text{bkg}}$ are the Hypatia PDF and the exponential PDF defined in Eq. (4.7) and Eq. (4.10), respectively. The shape parameters of the Hypatia PDF are determined by fits to the respective simulation subsets and are fixed in the final fit to the data subsets. To account for differences between simulation and data concerning the mass resolution, the widths of the signal shapes are scaled with the width ratio between data and simulation obtained in the mass parametrisation of the normalisation channel, see Table 4.10. As shown in Fig. 5.3 the chosen PDF describes the B_s^0 DTF mass distribution well. On the other hand, the parameter of the background PDF is fixed to the value obtained from a fit to data with removed signal region, i.e. the mass sidebands, as shown in Fig. 5.4. The final simultaneous fit to all data subsets, with fixed parameters as described above, is performed during the branching ratio computation shown in Section 6.3.

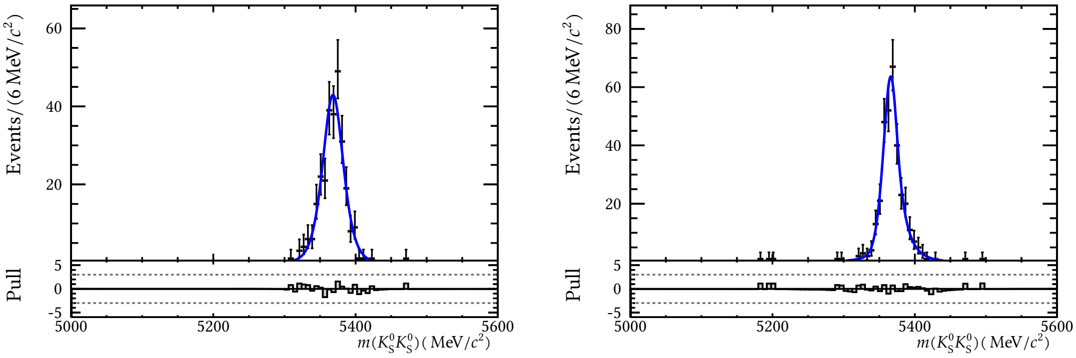

(a) Run I LL

(b) Run I LD

Figure 5.3 – Fit of the Hypatia PDF to the simulated B_s^0 mass distribution with DTF constraints on the K_S^0 masses and the PV for the Run I LL (left) and DD (right) subsets.

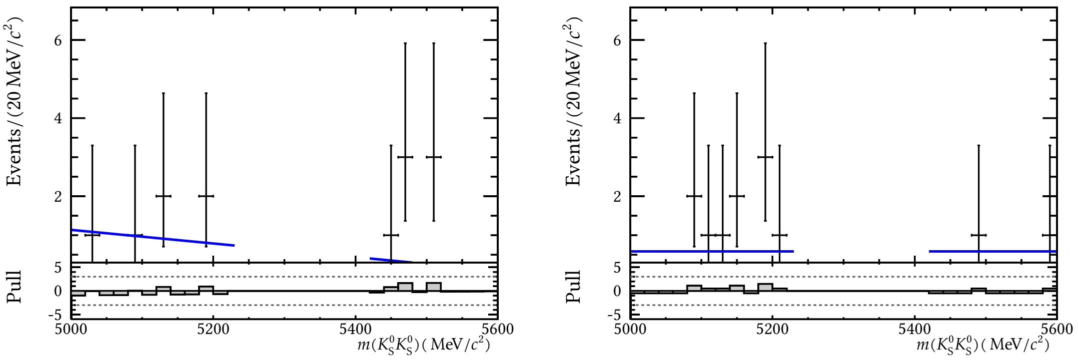

(a) Run I LL

(b) Run I LD

Figure 5.4 – Fit of the exponential PDF to the sidebands of the reconstructed B_s^0 mass distribution with DTF constraints on the K_S^0 masses and the PV for the Run I LL (left) and DD (right) subsets.

6 Measurement of the Branching Ratio $\mathcal{B}(B_s^0 \to K_S^0 K_S^0)$

This chapter discusses the computation of the branching ratio $\mathcal{B}(B_s^0 \to K_S^0 K_S^0)$ normalised to the branching ratio of the normalisation channel $B^0 \to \phi K_S^0$. As the LHCb internal review process has not yet been completed by the time this thesis is completed, only the result for the Run I data subsets is determined here. The measurement for the full dataset, comprising data recorded in the years 2011, 2012, 2015, and 2016, will be presented in Ref. [6].

Before the actual computation, Section 6.1 briefly describes the treatment of external inputs for the branching ratio calculation. In addition, Section 6.2 discusses systematic uncertainties studied by the author together with those investigated in Ref. [6].

6.1 External Inputs

For some parameters entering Eq. (3.3) external inputs are needed for the final computation of the branching ratio, since they cannot be computed in the course of this analysis.

Due to the different flavours of the signal B mesons in main and normalisation channel, the fragmentation fractions present in Eq. (3.1) do not cancel in the ratio. Hence, the ratio of the fractions, $\frac{f_s}{f_d}$, has to be taken from an external source. Here, the value obtained in Ref. [115] is used:

$$\frac{f_s}{f_d} = 0.259 \pm 0.015\,. \tag{6.1}$$

Furthermore, the total branching ratio of the normalisation channel, $\mathcal{B}(B^0 \to \phi K_S^0)_{\text{tot}} \equiv \mathcal{B}(B^0 \to \phi K_S^0 \to K^+K^-\pi^+\pi^-)$, including the branching ratios of the daughter decays are taken from external measurements [20]. The values used in the branching ratio computation are:

$$\begin{aligned}
\mathcal{B}(B^0 \to \phi K_S^0)_{\text{raw, PDG}} &= (7.3 \pm 0.7) \cdot 10^{-6}\,, \\
\mathcal{B}(\phi \to K^+ K^-)_{\text{raw, PDG}} &= 0.492 \pm 0.005\,, \\
\mathcal{B}(K_S^0 \to \pi^+ \pi^-)_{\text{raw, PDG}} &= 0.6920 \pm 0.0005\,, \\
\Rightarrow \mathcal{B}(B^0 \to \phi K_S^0)_{\text{tot}} &= (1.24 \pm 0.12) \cdot 10^{-6}\,.
\end{aligned} \tag{6.2}$$

For the computation of the normalisation constant α, see Eq. (3.3), only the nominal values of the external inputs are considered. Their uncertainties are considered as external systematic uncertainties, see Section 6.2.3.

6.2 Studies on Systematic Uncertainties

This section discusses the systematic uncertainties that were investigated by the author in the course of this analysis. At the end of this section, a summary of all systematic uncertainties entering the final value of the branching ratio is given, including those studied in Ref. [6]. For the final result of the branching ratio, internal systematic uncertainties, caused by detector effects and the selection of signal candidates, are separated from external systematic effects, i.e. external inputs from other measurements.

6.2.1 Multivariate Classification Systematic

In the determination of the branching ratio, the MVA selection efficiencies enter as the ratio

$$r_{\text{mva}} = \frac{\varepsilon_{\text{mva},\phi K_S^0}}{\varepsilon_{\text{mva},K_S^0 K_S^0}}. \tag{6.3}$$

To evaluate a systematic effect of the multivariate classifications for the two decay channels, the change of r_{mva} with varied classifier cuts of (± 0.01) is investigated for each subset, as depicted in Fig. 6.1. The systematic uncertainty of each subset is then calculated as the maximum of the relative deviation between nominal MVA selection efficiency ratio and the ratio with classifier cuts shifted to the right / left, respectively:

$$\Delta_{\text{mva,cat}} \equiv \max\left\{ \left(\frac{\left| r_{\text{mva, nom}} - r_{\text{mva, }-\text{shift}} \right|}{r_{\text{mva, nom}}} \right)_{\text{cat}}, \left(\frac{\left| r_{\text{mva, nom}} - r_{\text{mva, }+\text{shift}} \right|}{r_{\text{mva, nom}}} \right)_{\text{cat}} \right\}, \tag{6.4}$$

with cat $\in$ {Run I LL, Run I LD, Run II LL, Run II LD}. The results are shown in Table 6.1. To account for the individual subset sizes, the final systematic uncertainty is obtained as the track category and luminosity weighted mean of the systematic uncertainties for the four subsets:

$$\Delta_{\text{mva, Run i}} = \frac{\Delta_{\text{mva,LL}} \cdot \varepsilon_{\text{trkcat,LL}} + \Delta_{\text{mva,LD}} \cdot \varepsilon_{\text{trkcat,LD}}}{\varepsilon_{\text{trkcat,LL}} + \varepsilon_{\text{trkcat,LD}}}$$

$$\Rightarrow \Delta_{\text{mva}} = \frac{\sum_{i\in\{\text{I, II}\}} \Delta_{\text{mva, Run i}} \cdot \mathcal{L}_{\text{int, Run i}} \cdot \sigma_{b\bar{b},\text{Run i}}}{\sum_{j\in\{\text{I, II}\}} \mathcal{L}_{\text{int, Run j}} \cdot \sigma_{b\bar{b},\text{Run j}}} \tag{6.5}$$

$$= 1.62\,\%\,. \tag{6.6}$$

$$\Delta_{\text{mva}} = 1.62\,\%. \tag{6.7}$$

Table 6.1 – Systematic uncertainties for the MVA selection, calculated after Eq. (6.4) for each data subset.

	Run I LL	Run I DD	Run II LL	Run II DD
Δ_{mva}	0.008 ± 0.026	0.005 ± 0.018	0.012 ± 0.008	0.030 ± 0.008

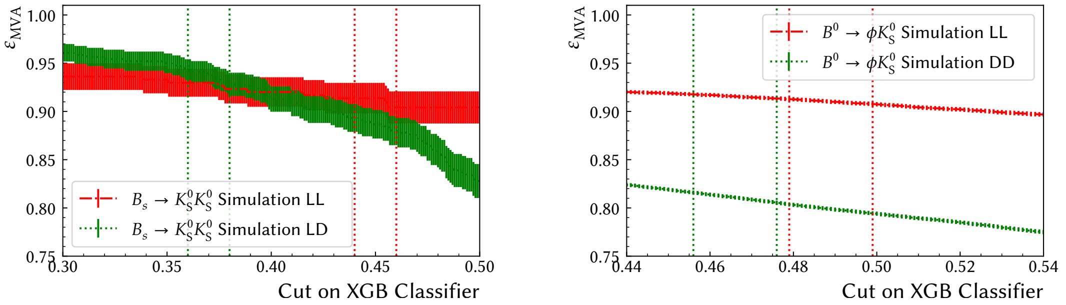

(a) $B^0_s \to K^0_S K^0_S$ Run I

(b) $B^0 \to \phi K^0_S$ Run I

Figure 6.1 – The progression of ε_{mva} in dependence of the classifier cut for the decay channels $B^0_s \to K^0_S K^0_S$ (left) and $B^0 \to \phi K^0_S$ (right) for both track categories. The shifted classifier cut points are marked by the vertical lines.

6.2.2 PID Selection Systematic

To study the systematic uncertainty of the PID selection, the PID selection efficiency is determined once on the nominal simulation subsets with the nominal resampled PID observables and once on simulation subsets were also the kinematic observables p_{T},

η, and `nTracks` are reweighted with corresponding distributions from sWeighted data (see Section 3.5) in addition to the PID resampling. The systematic uncertainty of each subset is then quantified as the relative deviation between the nominal and the altered PID selection efficiency ratio:

$$\Delta_{\text{PID, cat}} \equiv \left(\frac{\left| r_{\text{PID, nom}} - r_{\text{PID, alt}} \right|}{r_{\text{PID, nom}}} \right)_{\text{cat}} , \tag{6.8}$$

again with cat $\in$ {Run I LL, Run I LD, Run II LL, Run II LD}. Table 6.2 lists the result for each subset. The total systematic uncertainty of the PID selection is obtained following the same approach that was used for the MVA systematic, i.e. as the track category and luminosity weighted mean of the systematic uncertainties for the four subsets:

$$\Delta_{\text{PID}} = 1.09\,\% .$$

Table 6.2 – Systematic uncertainties for the PID selection, calculated after Eq. (6.8) for each data subset.

	Run I LL	Run I DD	Run II LL	Run II DD
Δ_{PID}	0.002 ± 0.006	0.0023 ± 0.0026	0.033 ± 0.004	0.0154 ± 0.0024

6.2.3 Other Systematic Uncertainties and Summary

Besides the systematic uncertainties studied in the previous subsections, some additional systematics have to be considered for the branching ratio. This includes systematics for the chosen fit models (Δ_{fitmodel}), for a potential bias of the extract signal yields (Δ_{fitmodel}), and for the discrepancy of the L0 trigger efficiency (Δ_{L0}). Furthermore, two systematic effects for the K_S^0 vertex resolution (Δ_{vtxres}), and for a potential misalignment of the downstream VELO stations (Δ_{VELO}) are taken into account. Finally, a systematic effect concerning the different hadronic interactions (Δ_{HI}) of the final state pions in the main channel compared to kaons in the normalisation channel final state is also considered. Ref. [6] provides studies and a detailed discussion of these systematic uncertainties, which are listed in Table 6.3. The total internal systematic uncertainty of is combined to:

$$\Delta_{\text{tot}} = 7.53\,\% . \tag{6.9}$$

As discussed in Section 6.1, the uncertainties of external inputs are also treated as systematic uncertainties:

$$\begin{aligned} \Delta_{B^0\to\phi K^0_\mathrm{S}} &= 9.7\,\%\,, \\ \Delta_{f_s/f_d} &= 5.8\,\%\,. \end{aligned} \tag{6.10}$$

Table 6.3 – Overview of the systematic uncertainties for the branching ratio computation. The individual systematics are discussed in the previous subsections.

Syst. Uncertainty	Value [%]
Δ_mva	1.62
Δ_PID	1.09
Δ_fitmodel	3.05
Δ_fitbias	1.97
Δ_L0	6.23
Δ_VELO	0.75
Δ_HI	0.52

6.3 Determination of the Branching Ratio

To determine the branching ratio of the decay $B_s^0 \to K_S^0 K_S^0$, a simultaneous unbinned maximum likelihood fit is performed to the reconstructed B_s^0 DTF mass in all four data subsets. As discussed in Section 5.3, the shape parameters of the signal and background PDFs are fixed to the values obtained from fits to simulation and data with excluded signal region, respectively, except the signal width, which is scaled according to Table 4.10, Page 75. Furthermore, an additional PDF with the same signal shape but a mean shifted to the B^0 mass is added to account for a potential contribution of $B^0 \to K_S^0 K_S^0$ candidates. Its signal yield is fixed to be a fraction, $f_{N_{\text{sig},\,B^0}/N_{\text{sig},\,B_s^0}}$, of the B_s^0 signal yield. The only shared parameter in the simultaneous fit is the predicted branching ratio, $\mathcal{B}_{\text{pred}}$, which is connected by Eq. (3.3) to the number of signal candidates, $N_{\text{sig},i}$, and the normalisation constants, α_i:

$$\mathcal{B}_{\text{pred}} = \alpha_i \cdot N_{\text{sig},i}\,, \tag{6.11}$$

with $i \in \{\text{Run I LL}, \text{Run I LD}\}$. In the simultaneous fit, the individual signal yields are fixed to the ratio $\mathcal{B}_{\text{pred}}/\alpha_i$ while the normalisation constants are constrained within their statistical uncertainties. The latter are calculated by combining the total selection efficiencies given in Eq. (4.5) and Eq. (5.4) for the normalisation and main channel, respectively, with the signal yield of the normalisation channel, see Eq. (4.14), and the external inputs shown in Eqs. (6.1) to (6.2). The parameters obtained in the simultaneous fit — shown in Fig. 6.2 — are listed in Table 6.4. The final result for the branching ratio of the decay $B_s^0 \to K_S^0 K_S^0$ is found to be

$$\mathcal{B}(B_s^0 \to K_S^0 K_S^0) = \left(22.9 \pm 7.3\,(\text{stat}) \pm 1.7\,(\text{syst}) \pm 2.2\,(\mathcal{B}(B^0 \to \phi K_S^0)) \pm 1.3\,({}^{f_d}\!/\!{}_{f_s})\right) \cdot 10^{-6}\,,$$

with a statistical significance of $3.7\,\sigma$ ($3.2\,\sigma$ including internal and external systematic uncertainties). No significant contribution from the decay $B^0 \to K_S^0 K_S^0$ can be observed.

Table 6.4 – Parameters obtained in the simultaneous unbinned maximum likelihood fit to the reconstructed B_s^0 mass in the two Run I data subsets.

	Run I LL	Run I LD
α	$(1.69 + / - 0.20) \cdot 10^{-6}$	$(1.05 + / - 0.10) \cdot 10^{-6}$
$N_{\text{sig},\,B_s^0}$	6.5 ± 2.2	10.5 ± 3.5
N_{bkg}	52 ± 7	21 ± 5
$f_{N_{\text{sig},\,B^0}/N_{\text{sig},\,B_s^0}}$	0.0 ± 0.5	

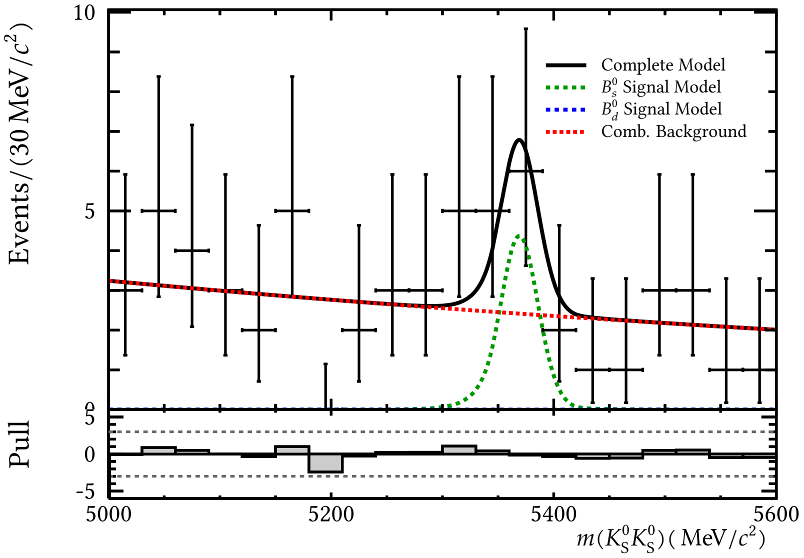

(a) Run I LL

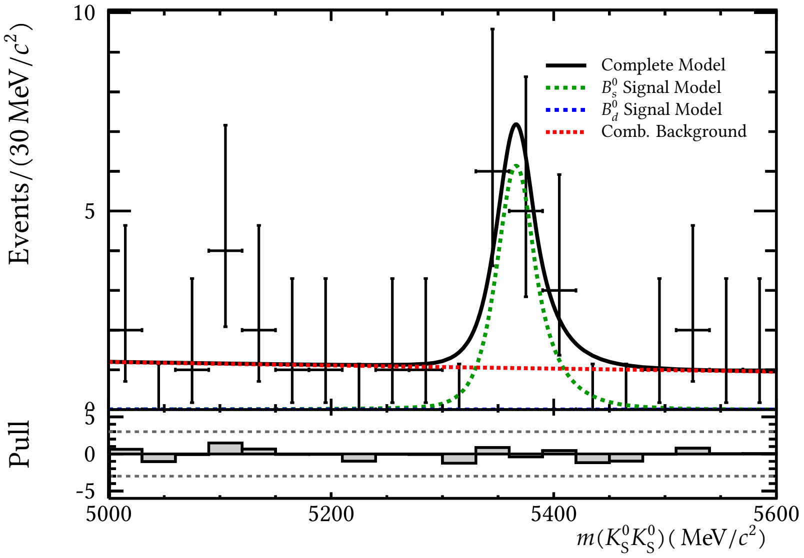

(b) Run I LD

Figure 6.2 – Simultaneous fit to the reconstructed $K_S^0K_S^0$ mass distribution for the determination of the branching ratio of the decay $B_s^0 \rightarrow K_S^0K_S^0$.

7 Simulation Studies for the Scintillating Fibre Tracker Upgrade of the LHCb experiment

An important part of this doctorate went into simulation studies for the upgrade of the tracking stations T1–T3 of the LHCb experiment, the *Scintillating Fibre* (SciFi) tracker. This chapter starts with an overview of the SciFi tracker layout and functionality. A motivation for the upgrade of the LHCb detector is given in Section 2.4, Page 41. After elaborating on the importance of simulation studies in the field of detector development, the chapter closes with a presentation and discussion of the results of the simulation studies of the light yield attenuation in the SciFi tracker and their use in the future detector simulation.

7.1 The LHCb Scintillating Fibre Tracker

The SciFi tracker consists of mats of scintillating fibres with a multichannel SiPM readout which has several important advantages for the third run period of the LHC: the propagation time of scintillation photons along the scintillating fibres, as well as the decay constant of the scintillation material are both in the range of 1 to 30 ns which allows to process the measured particle hits without overlapping of successive proton-proton collisions. Furthermore, a low energy loss of particles traversing the SciFi tracker is ensured since the excitation process inside the scintillating fibres only requires energies of $O(10)$ keV.
While Section 7.2 describes the basic mechanisms of scintillating fibres, this section focusses on the SciFi tracker layout. If not stated otherwise, the information given here is based on Refs. [8, 116].

Fig. 7.1 shows a schematic representation of a SciFi tracker station. Each of the stations is centred at the same z-position as the three old downstream tracking stations, located between the magnet and the second Ring-Imaging Cherenkov Detector, as shown in Fig. 7.2. A SciFi station consists of four detecting layers, each composed of ten (twelve for T3) identically constructed modules, with the exception of the modules enclosing the beam pipe. The layers are arranged in the known x-u-v-x geometry, where the modules in the second (third) layer are tilted by $-5°$ ($+5°$) wrt. the y-axis.

Each of the modules has a multilayer sandwich structure: the detecting fibre mats, each consisting of six staggered layers of 2.4 m long scintillating fibres with a diameter of 250 µm, are encased in supporting materials to provide stability, while also meeting the required low material budget. The modules are separated in upper and lower halves in order to reduce occupancies, thus lowering combinatorial background in the track reconstruction. To further increase the light yield, the fibre mats have mirrors at the height of the beam pipe. This is also shown in Fig. 7.1.

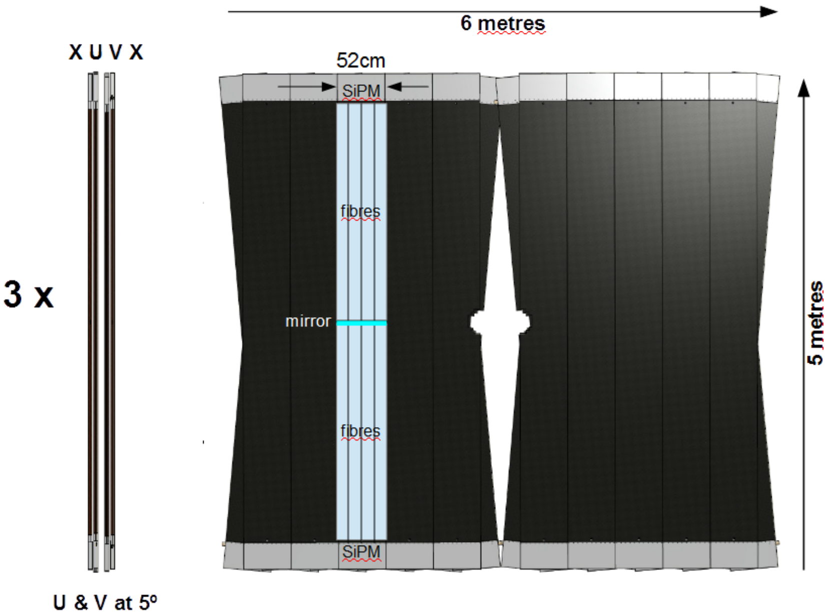

Figure 7.1 – Schematic representation of a SciFi tracker station in open position. A station consists of four detecting layers, arranged in the same x-u-v-x layout that was used for the old tracking stations. Each layer has ten to twelve modules, depending on the required acceptance, that are read out by SiPMs on the top and bottom. [117]

Ionizing particles passing the SciFi tracker deposit energy in the order of keV in the scintillating fibres, which triggers a scintillation process, further explained in Section 7.2.1. Due to the optical properties of the scintillating fibres (see Section 7.2.2), which enable total reflection, the produced photons propagate along the fibre, either straight to the photodetector read-out or with a detour over the mirror at the opposite end. The SciFi photomultipliers are 128-channel *silicon photomultipliers* (SiPMs) arrays, where each 96-pixel channel has a width of 250 µm in x and covers the six layers of the fibre mat in z. Since particles may produce signals in several SiPM channels, e.g. with a high p_x/p, this information cannot be used to process particle hit coordinates for the track reconstruction, as the amount of data would be too high for a full bunch crossing read-out with a rate of 40 MHz. Instead, the signals from adjacent channels are combined to clusters, so that the actual hit can be determined as its barycentre: Each pixel of the SiPM can detect one photon so that the processed signal amplitude

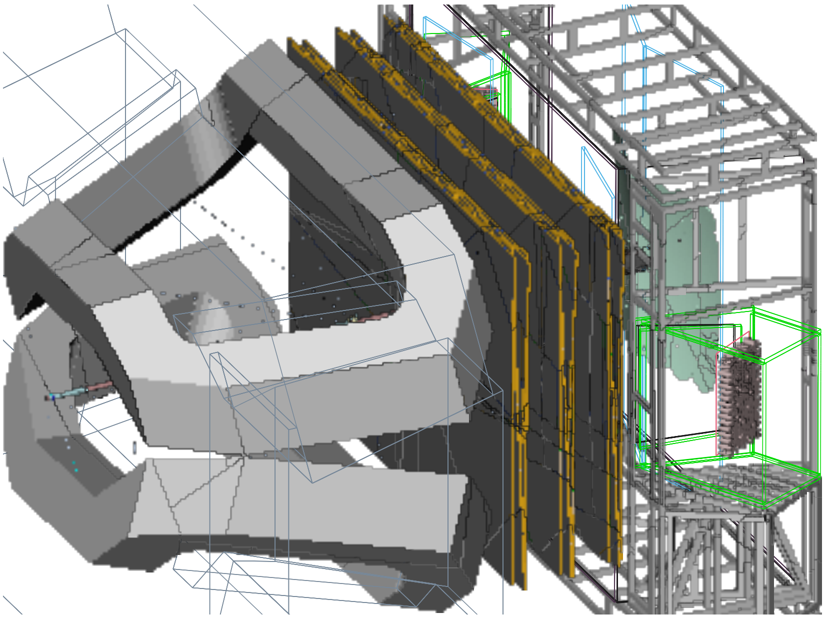

Figure 7.2 – The three stations of the SciFi tracker located between the dipole magnet on the left and the RICH2 detector on the right. [8]

per channel is proportional to the total number of pixels fired, as illustrated in Fig. 7.3. The hit position can then be calculated as a weighted mean.

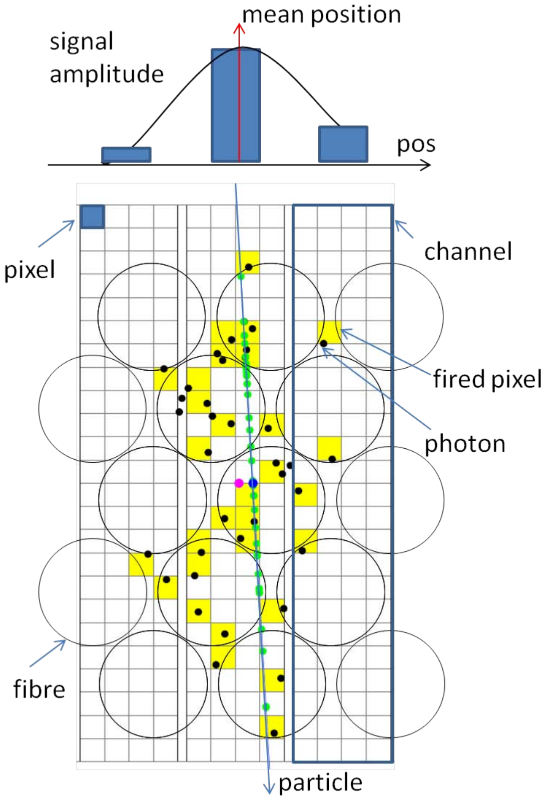

Figure 7.3 – Illustration of the particle hit determination in the SciFi tracker. [8]

7.2 Scintillating Fibres

This section aims to describe the basic mechanisms of the base technology of the SciFi tracker, from the production of light in the fibre core to the guidance and attenuation of light along the fibre.

7.2.1 Scintillation Process

The SciFi tracker's scintillating fibres are double-cladded plastic fibres from the Japanese manufacturer Kuraray. Figure 7.4 shows a schematic representation of a scintillating fibre. The fibre core consists mainly of polystyrene, an organic scintillator. An ionizing particle passing through the fibre core excites the valence electrons from so-called benzene rings in the orbitals of the polymer [118]. In the relaxation, those electrons then emit scintillation photons. Because the scintillation light yield — the number of scintillation photons per deposited energy — of pure polystyrene is low, a dopant is added to the fibre core material [119]. The fibres used for the SciFi tracker use a combination of p-Terphenyl and *tetraphenyl–butadiene* (TPB) [120]. As can be seen in Fig. 7.5, the TPB serves as a *wavelength shifter* (WLS), which absorbs the photons emitted by the first dopant p-Terphenyl and re-emitting them at higher wavelengths, where the scintillators are transparent. The exact concentrations of the two dopants is important to maximise the light yield. A high enough concentration of about 1 % p-Terphenyl enables a radiation-less energy transfer via the so-called Förster Transfer [121]. For the WLS, too low a concentration leads to some photons emitted by the first dopant to leave the fibre before they are re- absorbed by the TPB. On the other hand, a higher concentration causes an increased self- absorption. An alternative could be the dye 3-HF, shown in Fig. 7.5, which is even more transparent and also more radiation hard, due to its larger Stokes Shift: as discussed in Section 7.2.3, higher wavelengths are much less affected by radiation damage. However, its smaller light yield and higher decay time render it useless for the SciFi tracker.

7.2.2 Light Guidance and Attenuation

The scintillating fibres are designed to guide the photons — produced by the scintillation process explained in the previous subsection — along the fibre by total reflection. This is why the claddings have decreasing refraction indices, see Fig. 7.4. In principle, the WLS re-emits the photons isotropically, but only a small fraction is emitted under the correct angle for total reflections be able to happen. For one hemisphere, the trapping efficiency for photons emitted from the fibre axis is given by [119]:

$$\varepsilon_{\text{trap}} = \frac{1}{2}(1 - \frac{n_{\text{clad}}}{n_{\text{core}}}) \tag{7.1}$$

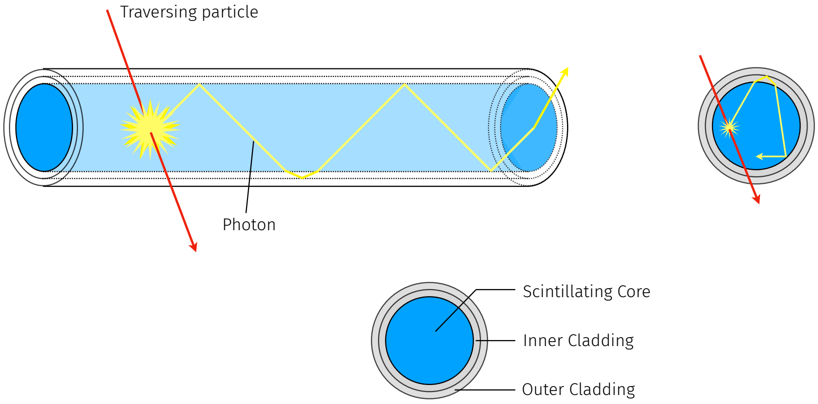

Figure 7.4 – Cross section and lateral schematic view of a double-cladded plastic fibre. The yellow line shows a possible path of photon, produced by the scintillation process from a ionizing particle, symbolized by the red line. The dimensions are not true to scale.

which yields about 5.3 %. In the cases where photons follow a helix path, the trapping efficiency increases ($\varepsilon_{\text{trap}} = \frac{1}{2}(1 - (\frac{n_{\text{clad}}}{n_{\text{core}}})^2)$ for photons emitted uniformly over the fibre cross section), but on the downside the attenuation of these photons is higher due the longer path through the fibre and the larger amount of reflections at the fibre boundary layers. The effective gain in trapping efficiency from helix light rays is expected to be in the order of 10 to 30 % [125].

Photons travelling alongside the fibre are attenuated by different processes: they are (re-)absorbed or scattered and can even get lost due to scattering at the boundary layers. Figure 7.6 shows the different intrinsic attenuation coefficients of the two fibre components polystyrene and the second dopant, the WLS TPB: Below photon wavelengths of 450 nm, the total attenuation of pure polystyrene is prevailed by electronic transitions and by Rayleigh scattering above. In the spectral range of the scintillation photons, defined by the emission and absorption spectra, shown in Fig. 7.5, molecular vibrations are of minor importance. Even though the concentration of TPB is quite low, compared to polystyrene, its re- absorption is the main source for light yield attenuation in scintillating fibres below photon wavelengths of 450 nm.

In addition to the intrinsic attenuation factors mentioned above, there are several extrinsic attenuation factors, which increase total light yield attenuation: Dust particles or water enclosed in the fibre material during production leads to additional photon scattering or absorption. Besides, non- perfect claddings lead to additional photon losses.

7.2.3 Light Yield Attenuation from Radiation Damage

A major extrinsic attenuation factor not yet discussed but quite important for a detector to be operated at a particle accelerator is the light yield attenuation induced

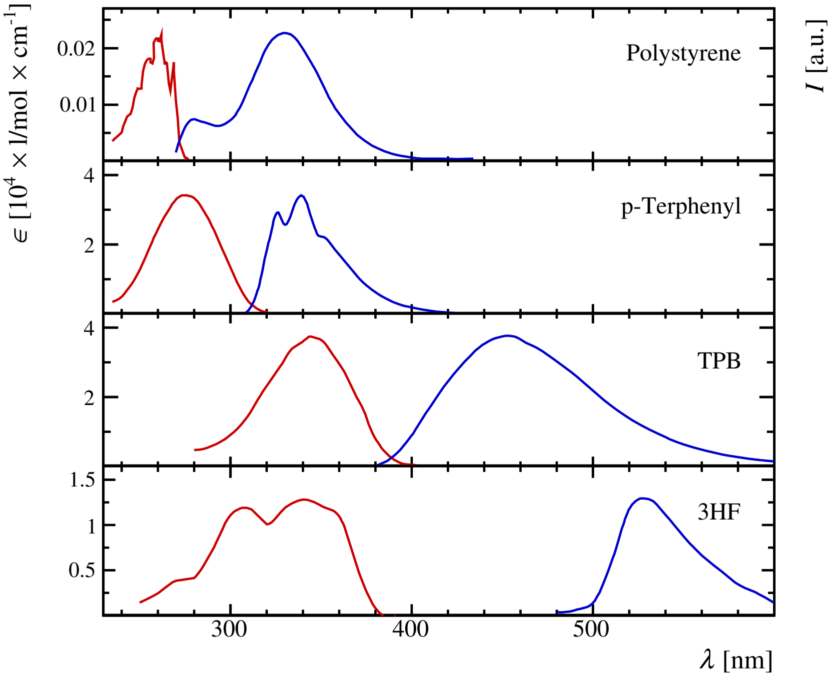

Figure 7.5 – Absorption (red) and emission (blue) spectra of different materials used in scintillating fibre cores. The absorption is shown as the molar attenuation coefficient and the emission as an intensity in arbitrary units. Polystyrene is the core material, p-Terphenyl and TPB are the primary and secondary dopants used in the fibres from Kuraray for the LHCb SciFi tracker, the data is taken from [122]. 3HF is an alternative dopant with a larger Stokes Shift (data from [123]). The figure is taken from [124].

by damage to the fibre materials through ionising radiation. Irradiation of the fibre material leads to a higher absorption, i.e. an overall lower transparency. As can be seen in Fig. 7.7, a simulation with the Monte Carlo generator FLUKA (see Section 7.3.2) shows an expected dose of up to 30 kGy around the beam pipe and around 1 kGy in the main parts of the tracking station, after data-taking of an integrated luminosity of $\mathcal{L}_{\text{int}} = 50\,\text{fb}^{-1}$ at the position of the Inner Tracker in tracking stations T1, z =760 to 780 cm.

One can distinguish between two categories of observed radiation damages, short-lived, annealing damages and permanent ones. Several studies with scintillating fibres having various dopants show the formation of short-lived absorption centres by free radicals, which absorb light at longer wavelengths (500 to 700 nm) [126–128]. The main radiation damage however stems from permanent absorption centres formed in the polystyrene core and is discovered to grow proportional with the applied dose. It is therefore taken into account as an additional attenuation per dose [m^{-1}kGy^{-1}]. The absorption spectra of those permanent radiation damages lie at shorter wavelengths of about 250 to 320 nm [129] but their tails are visible as exponential tails in the relevant

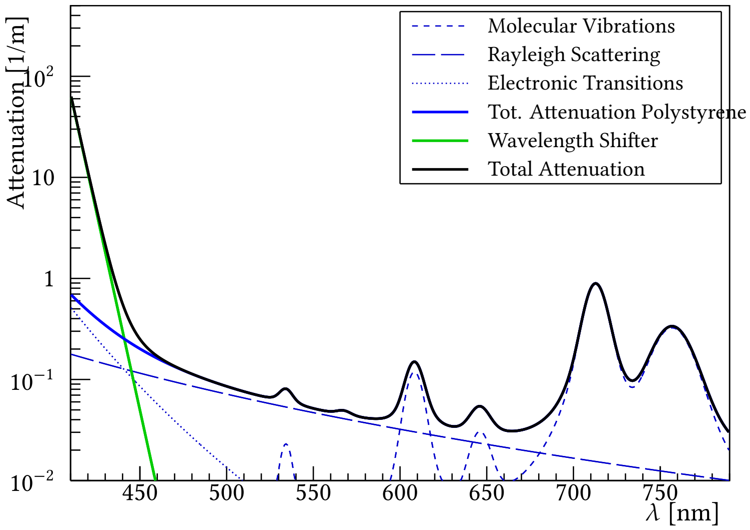

Figure 7.6 – The different intrinsic attenuation coefficients from polystyrene (blue) and the WLS TPB (green). Due to the wavelengths spectrum, shown in Fig. 7.5, the main source for light attenuation in scintillating fibres is the re-absorption of photons by TPB. Data from [124].

wavelength spectrum.

The exact process of radiation damage in scintillating fibres is quite complex and still not properly described. In general, an applied dose increases the light yield attenuation through the formation of scattering and absorption spots by free radicals like benzyl, cyclohexadienyl or others [129]. Over time, these radiation damages can anneal by (re-)combination of the free radicals with oxygen or themselves. This forming and annealing of absorption centres depends notably on the environment the fibre is in, e.g. the presence of oxygen evidently alters the effects of irradiation: At high dose rates, oxygen is utilized faster than it can propagate into the fibre while it is accessible during the whole process for lower dose rates [130]. Even though, the availability of oxygen enables annealing to happen during the irradiation, the long-term damage in fibres irradiated with smaller dose rates is higher, because more oxidation products are produced which in turn decrease the fibre transmittance [131]. Because of this, radiation induced damage is potentially underestimated when trying to extrapolate the expected damage after long-term irradiation at low dose rates from studies with short-term irradiation at high dose rates.

In order to better understand this effect, different irradiation campaigns at different doses / dose rates were performed by the LHCb SciFi group over the years [120]. Ref. [132] shows a combination and a corresponding analysis of their results. Furthermore,

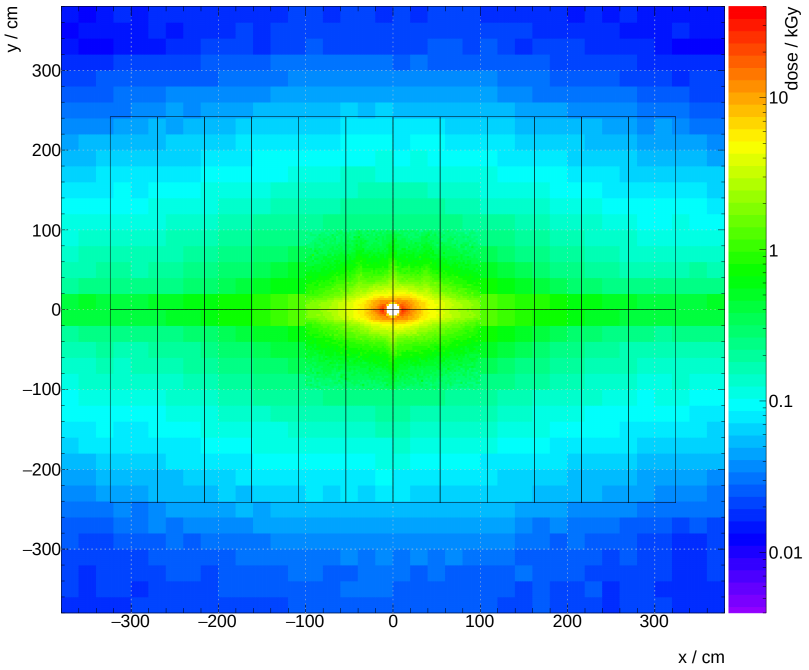

Figure 7.7 – Simulated expected dose for an integrated luminosity of $\mathcal{L}_{\text{int}} = 50\,\text{fb}^{-1}$ at the position of T1, z =760 to 780 cm.

it defines two models for the additional attenuation from radiation damage as a function of the wavelength of the photons and the applied dose. On the basis of fundamental considerations, the damage is expected to increase linear with the dose. However, the data from the different irradiation campaigns indicates, that the damage per dose is lower for higher doses. Since a saturation of the initial damage is not expected in the dose range investigated, one possible explanation for this effect could be an increased annealing yield. To describe this lower relative damage at high doses, a power law model

$$a_{\text{rad,pow}}(\lambda, D) = 0.4 \cdot D^{0.8} \cdot \mathrm{e}^{-3.01 \cdot 10^{-2} \cdot (\lambda - 450)} \tag{7.2}$$

with the attenuation a given in m^{-1}, the dose D in kGy and the wavelength λ in nm, was adapted to the data, see Fig. 7.8a. Alternatively, the effect could be explained with a systematically higher dose rate in the irradiation campaigns that contributed the data points for higher doses. To account for this, a linear model

$$a_{\text{rad,lin}}(\lambda, D) = 0.38 \cdot D \cdot \mathrm{e}^{-3.01 \cdot 10^{-2} \cdot (\lambda - 450)} \tag{7.3}$$

was fitted to the low dose rate data only, see Fig. 7.8b. The wavelength dependence is described by the same exponential decrease of the damage with increasing wavelength in both models. Both models fail to explain all the differences between the irradiation campaigns, which could have been caused by different particles used for the irradiation of the scintillating fibres. Additional irradiation measurements of scintillating fibre mats, performed in the LHCb cavern and therefore with the "correct" mixture of particles and a realistic dose rate, did not yield systematic differences to the two models [132, 133].

The radiation damage models are one of the inputs for the single fibre simulation (see Section 7.3.1) used in the simulation studies of the light yield attenuation in the SciFi tracker, see Section 7.3.2.

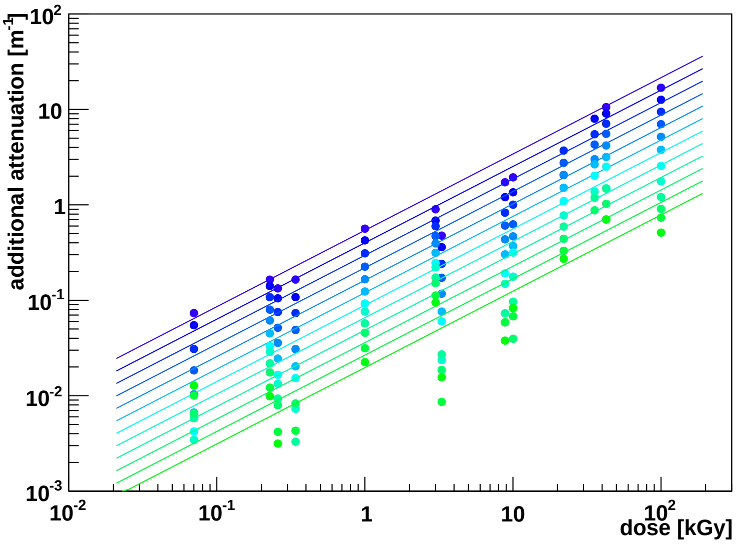

(a) Power law Model

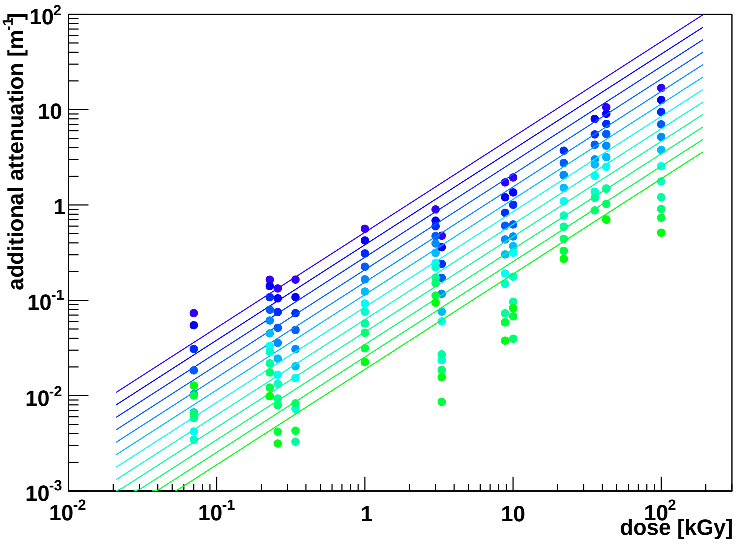

(b) Linear Model

Figure 7.8 – The (a) power law and (b) linear model for the radiation damage as a function of the dose. The colours correspond to different wavelength between 440 nm (violet, uppermost line) and 550 nm (neon green, bottom line). Plots from [132]

7.3 Light Yield Attenuation Map Simulation

This section describes the simulation studies performed by the author to investigate the expected light yield attenuation due to irradiation as well as the construction of a software framework for the production of lookup maps for the light yield attenuation as a function of the hit position, so called *light yield attenuation maps* (LYAMs). As mentioned in Section 7.2.3, radiation induced damage is potentially underestimated, when trying to extrapolate the expected damage after long-term irradiation at low dose rates from measurements with short-term irradiation at high dose rates. Furthermore, each measurement only provides a discrete data point for a given dose rate, while it is necessary to know the light yield attenuation at an arbitrary recorded integrated luminosity of the LHCb detector, which makes a simulation indispensable. In addition, a well described light yield attenuation is important for different studies investigating the long-term performance of the upgraded LHCb detector, e.g. studies of the tracking efficiency, and, after the LHCb Upgrade, also for the production of simulated events needed in physics analyses. All this leads to the conclusion, that the light yield attenuation maps are an important addition to the SciFi software framework.

The following subsections give a description of the underlying Single Fibre `Geant4` simulation and a detailed description of the design of the LYAM framework, and finally an overview of its results and application in the SciFi software framework and the detector simulation as a whole.

7.3.1 Single Fibre Simulation

The LYAM simulation framework is based on a single fibre simulation framework [124, 134]. As outlined in Section 7.2, the processes in a scintillating fibre, from energy deposition to light production and attenuation, are quite complex. Therefore, Monte Carlo methods are useful to study certain behaviours of scintillating fibres. The single fibre simulation is realised with the `C++` programming language and the `Geant4` [95, 135] framework.
The simulation, with all the input and output parameters, is explained in great detail in Ref. [134].

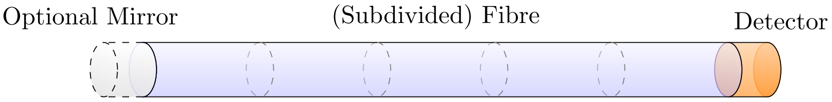

Figure 7.9 – Geometry used in the `Geant4` single fibre simulation, consisting of a fibre, a photodetector, and an optional mirror. For studies of radiation damage, the fibre can be subdivided into sections with different applied radiation doses. [124]

Fig. 7.9 depicts the experimental setup, realised in the single fibre simulation. At the fibre's right end, a detector is simulated to detect incoming photons. For the purpose of the LYAM simulation, the detector material is chosen to be polystyrene, to prevent effects like Fresnel reflection or refraction at the boundary between fibre core and detector. To study effects of photons traversing an air gap before reaching the detector, like an altered exit angle distribution, it is also possible to choose vacuum as the detector material.

An optional mirror with a variable reflectivity is placed on the opposite end of the fibre. Setting the reflectivity to 100 % and storing the number of reflections for every detected photon, enables an adjustment of the reflectivity in the analysis of the output, without having to rerun the simulation. The same holds for the reflectivity between fibre core and cladding, see Eq. (7.11).

To study the effect of a location-dependent dose profile along the fibre, as is the case for the SciFi tracker (see Fig. 7.7), the fibre can be subdivided into a certain number of equally-spaced sections, as shown in Fig. 7.9. For each section the dose level in units of kGy can be provided as a separate input file.

In short, the single fibre simulation program simulates the following processes:

- Generation of photons via scintillation or the Cherenkov effect.
- Absorption and re-emission of photons by the wavelength shifter.
- Rayleigh Scattering.
- Absorption processes in the core material.
- Boundary processes, like (Fresnel) reflection, Fresnel refraction and absorption.

The individual formulas and parameters, e.g. the formula for the attenuation, emission and absorption spectra of WLS and scintillation processes, are provided via a parameter file, see Ref. [134].

The output of the single fibre simulation contains many observables of produced and detected photons, respectively. They are stored in a `ROOT` file with separate containers (`TTree`) for produced, wavelength-shifted and detected photons.

The parameters and inputs used for the purpose of the LYAM simulation are further described in Section 7.3.2.

7.3.2 Simulation Inputs

This subsection describes the parameters and inputs for the single fibre simulation that were used for the light yield attenuation map simulation, provided either via the main parameter file or individual parameter files in the case of the dose profile.

The boundary, scattering, reflection, and absorption processes of the fibre material are included in the Single Fibre `Geant4` simulation. The losses due to non-perfect reflection

of the photons at the core-cladding boundaries are applied afterwards. As mentioned before, the number of reflections for every photon is stored by simulation, which supersedes rerunning the simulation for different reflectivity parameters. An equivalent approach is done for the mirror reflectivity. It is set to 100 % in the simulation and a lower reflectivity is applied afterwards, when using the light yield attenuation map in the simulation of the SciFi digitization process in `Boole`, see Section 7.3.4.
The light yield attenuation in the fibre in dependence of the wavelength is provided as a function $A(\lambda)$. In addition to the basic attenuation, the light yield attenuation due to radiation damage is provided as a function of the wavelength and the dose, $a_{\mathrm{rad}}(\lambda, D)$. They are both made available to the simulation program via the main parameter file. The dose profile is not given as a function, but with the help of binned values, which are in this special case retrieved from 2D FLUKA dose maps.

Attenuation Coefficients

The different effects explained in Section 7.2.2 lead to a total wavelength dependent attenuation in polystyrene of:

$$A(\lambda) = a_{\mathrm{e}}(\lambda) + a_{\mathrm{r}}(\lambda) + a_{\mathrm{v}}(\lambda) + a_{\mathrm{i}}(\lambda) \tag{7.4}$$

with the single attenuation coefficients describing the electronic transitions (a_{e}), the Rayleigh scattering (a_{r}), and the molecular vibrations (a_{v}). a_{i} is a constant and describes the light loss due to imperfections in the fibre material. The total attenuation, including the attenuation from the WLS is shown in Fig. 7.6. Ref. [124] shows the formulas and the determination of their parameters with the help of values from literature for pure polystyrene and the WLS. However, measurements of scintillating fibres used for the SciFi tracker showed a higher absorption. This can be explained by different effects, an additional absorption due to impurities in the core or by losses at imperfect core-cladding / cladding-cladding boundaries during total reflection. The second one has a strong effect on the angular dependence of the absorption and can therefore be addressed with the help of dedicated measurements. These are described in Refs. [132, 136].

Radiation Damage Models

The light yield attenuation is further enhanced by an additional attenuation from radiation damages $a_{\mathrm{rad}}(\lambda, D)$, as described in Section 7.2.3. This leads to an altered total wavelength dependent attenuation of:

$$A'(\lambda) = A(\lambda) + a_{\mathrm{rad}}(\lambda, D). \tag{7.5}$$

In order to simulate the long-term impact of the two radiation damage models, shown in Fig. 7.8 and defined in Ref. [132], simulations were performed with both models. The power law model, described in Eq. (7.2), is used as the standard description of additional attenuation due to radiation for the light yield attenuation maps, since it is designed to describe all the available data points without underestimating a single one. The linear model, defined in Eq. (7.3), is used as conservative alternative to study the case of a dose-rate-dependent radiation damage.

Dose Maps

The dose profiles, used as an input for the single fibre simulations, that are in turn needed for the generation of the radiation-induced light yield attenuation maps, are drawn from so called dose maps. They were produced with the FLUKA software package [137, 138] for an integrated luminosity of $50\,\mathrm{fb}^{-1}$ at different z positions in the LHCb detector: $z = 760 - -780\,\mathrm{cm}$, $z = 780 - -800\,\mathrm{cm}$, $z = 900 - -920\,\mathrm{cm}$ and $z = 920 - -940\,\mathrm{cm}$. Looking at Table 7.1, these positions correspond to the IT and OT positions in the tracking stations T1 and T3.

Table 7.1 – Nominal z positions of the LHCb tracking stations T1–T3. [8]

Station	Inner Tracker		Outer Tracker	
	z_{min}[cm]	z_{max}[cm]	z_{min}[cm]	z_{max}[cm]
T1	767.3	782.8	783.8	803.8
T2	836.0	851.5	852.5	872.5
T3	905.0	920.5	921.5	941.5

The dose maps were simulated [139, 140] by taking the current LHCb detector geometry and materials into account, especially the detector materials of the Inner and Outer Tracker [141]. The difference to the dose deposited in the detector material of the SciFi tracker is expected to be very low. Further, pp collisions with a centre-of-mass energy of 14 TeV and a collision angle of 180° were simulated.

The FLUKA dose maps are provided in bins of $2.5\,\mathrm{cm} \times 2.5\,\mathrm{cm}$ for up to $\pm 1\,\mathrm{m}$ in x and y. For the outer regions the binning changes to $20\,\mathrm{cm} \times 20\,\mathrm{cm}$, as can be seen in Fig. 7.7. To obtain a dose map with an overall granularity of $2.5\,\mathrm{cm} \times 2.5\,\mathrm{cm}$ a linear interpolation is performed for this outer region, as shown in Fig. 7.10. Therefore, the smallest binning of the FLUKA dose map defines the granularity of the overall dose maps as well as the granularity of the light yield attenuation maps. Only the upper right quarter ($x \in \{0 \ldots 3\}\,\mathrm{m}$; $y \in \{0 \ldots 2.5\}\,\mathrm{m}$) is used due to the symmetry of the LHCb detector.

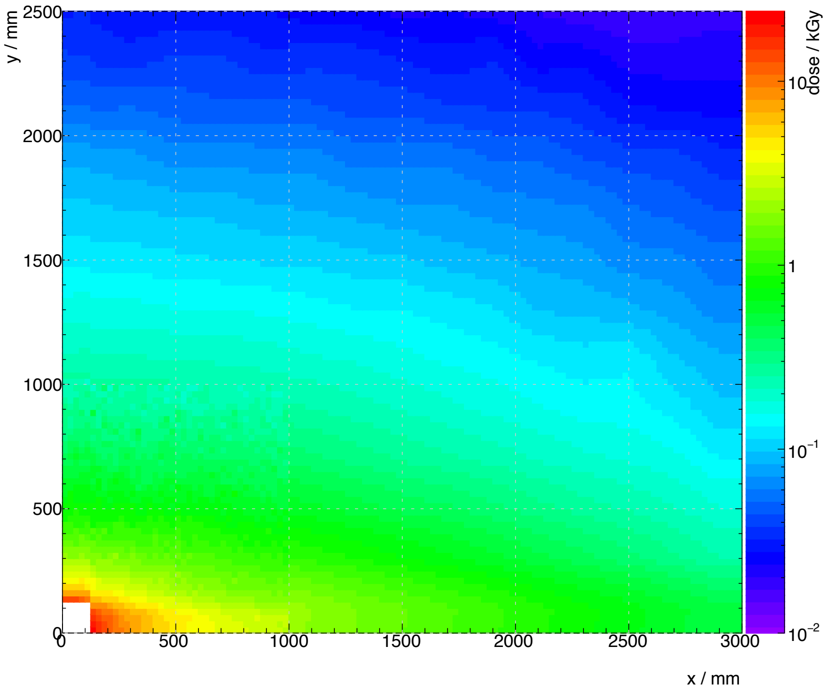

Figure 7.10 – FLUKA dose map with interpolation at $z = 760 - -780$ cm for $\mathcal{L}_{\text{int}} = 50\,\text{fb}^{-1}$ in the upper right quarter of the SciFi tracker.

7.3.3 From Single Fibre Simulations to Light Yield Attenuation Maps

The aforementioned Single Fibre `Geant4` simulation is used to calculate light yield attenuation coefficients by comparing the number of detected photons to the number of initially generated photons in a given excitation point. In order to obtain a whole map of attenuation coefficients, the LYAM, for different (x, y)-coordinates in the SciFi tracker, N_{sim} Single Fibre `Geant4` simulations are conducted. To save computing time, the simulations are set up to generate the scintillation photons isotropically on a plane in the fibre core, without the intermediate step of simulating an exciting particle traversing the fibre and therefore producing photons. Each simulation corresponds to an excitation with N_γ resulting photons at this (x, y)-coordinate and the measurement of the number of detected photons. If one assumes an irradiated SciFi tracker with a recorded luminosity of $50\,\text{fb}^{-1}$ the dose profile, given by the 2D FLUKA dose map, is also taken into account. Simulations which correspond to the same x-coordinate of the dose map can be considered simulations of an identical fibre with the same dose profile along y but different excitation points. Therefore, the required number of simulations is given by:

$$N_{\text{sim}} = N_{\text{fibres}} \cdot N_{\text{ex}} \tag{7.6}$$

with the number of fibres, N_{fibres}, and the number of excitations per fibre, N_{ex}. The number of fibres one has to simulate per quarter of the SciFi tracker, is given by the width of this quarter and the width of a LYAM bin, both in x:

$$N_{\text{fibres}} = \frac{x_{\text{quarter}}}{x_{\text{bin}}}. \tag{7.7}$$

As mentioned before, the width of a bin is determined by the granularity of the input FLUKA dose map. The number of excitations per fibre is further defined by the length of a fibre, l_{fibre}, and the height of a LYAM bin, both in y:

$$N_{\text{ex}} = \frac{l_{\text{fibre}}}{y_{\text{bin}}}. \tag{7.8}$$

For symmetry reasons, it suffices to simulate only one quarter of the SciFi tracker, which results in $x_{\text{quarter}} = 3000\,\text{mm}$. To account for the rectangular beam pipe hole [116] of 130.8 mm width and 115 mm height, the fibre length l_{fibre} is set to 2385 mm for $x \leq 130.8\,\text{mm}$ and to 2500 mm for $x > 130.8\,\text{mm}$. Considering the interpolated dose map bin sizes of $x_{\text{bin}} = y_{\text{bin}} = 25\,\text{mm}$ (see Section 7.3.2) this results in:

$$N_{\text{sim}} = 120 \cdot 101 = 12120.$$

In order to ensure a correct radiation induced attenuation of the photons, the excitation points $\{x_{\text{ex},i}; y_{\text{ex},i}\}$ are positioned in the middle of the lower edge of a dose map bin, so that on average the correct dose is applied:

$$x_{\text{ex},i} = 25\,\text{mm}/2 + i \cdot 25\,\text{mm} \qquad \text{with} \quad i = 0, 1, 2, \ldots 119 \tag{7.9}$$

$$y_{\text{ex},i} = \quad 0.5\,\text{mm} + i \cdot 25\,\text{mm} \qquad \text{with} \quad i = 0, 1, 2, \ldots 100. \tag{7.10}$$

The next step in the LYAMs production consists in the read-out and further processing of the results from the single fibre simulations. As mentioned in section Section 7.3.1, it is possible to change certain parameters of the simulation, especially the wavelength dependent *photon detection efficiency* (PDE) of the silicon photomultipliers or the reflection losses of photons at the core-cladding / cladding-cladding boundaries, without having to rerun the simulations. This is possible, because more information of the produced, wavelength-shifted and detected photons than just their quantities is stored, e.g. the output of each single fibre simulation contains the wavelength distributions and a reflection count of each photon. While reading out the single fibre simulations outputs and calculating the attenuation coefficients, the number of detected photons is further weighted with a reflection efficiency $\varepsilon_{\text{refl}}^{\text{fibre}}$, stemming from the photon loss from core-cladding and cladding-cladding reflections and the SiPM PDE $\varepsilon_{\text{PDE}}(\lambda_i)$, both on a per-event basis:

$$\varepsilon_{\text{refl}}^{\text{fibre}} = (1 - p_{\text{BL}})^{n_{\text{refl,i}}} \tag{7.11}$$

$$\varepsilon_{\text{PDE}}(\lambda_i) = p_3(\lambda_i - \lambda_{\text{max}})^3 + p_2(\lambda_i - \lambda_{\text{max}})^2 + \varepsilon_{\text{maxPDE}} \tag{7.12}$$

Here, $p_{\text{BL}} = 5 \cdot 10^{-5}$ is the photon loss probability, which is determined by comparing results from the single fibre `Geant4` simulation to measurements [136], and $n_{\text{refl,i}}$ is the number of reflections at the boundaries core-cladding and cladding-cladding for photon i. The PDE $\varepsilon_{\text{PDE}}(\lambda_i)$ for the newest model of the SiPM from 2017 [142] is obtained from a regression with a third-degree polynomial. The fit results for the parameters are:

$$\begin{aligned} p_3 &= 39.20 \cdot 10^{-9}\,\text{nm}^{-3} \\ p_2 &= -12.02 \cdot 10^{-6}\,\text{nm}^{-2} \\ \varepsilon_{\text{maxPDE}} &= 0.4216 \\ \lambda_{\text{max}} &= 479.1\,\text{nm} \end{aligned}$$

Fig. 7.11 show the measured PDE for the 2017 SiPM and the corresponding fit of $\varepsilon_{\text{PDE}}(\lambda_i)$.

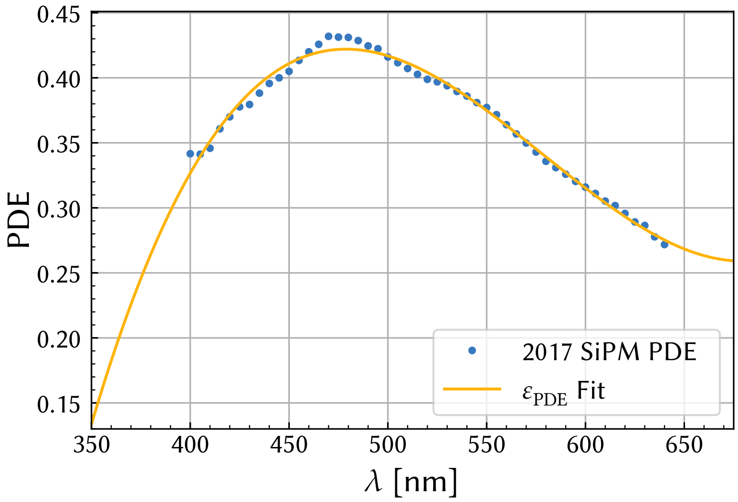

Figure 7.11 – SiPM photon detection efficiency as a function of the wavelength, which is applied in the attenuation map production. The function is a third-degree polynomial fitted to data from measurements [142].

In summary, one ends up with a lookup table which contains light yield attenuation coefficients $\varepsilon_{\mathrm{ly}}$ for every bin of the input dose map, separated by direct ($N_{\gamma,\mathrm{dir}}$) and mirror reflected ($N_{\gamma,\mathrm{refl}}$) photons:

$$\varepsilon_{\text{ly, direct photons}}(x,y) = \sum_{i}^{N_{\gamma,\mathrm{dir}}} \varepsilon_{\mathrm{refl}}^{\mathrm{fibre}}(x,y) \cdot \varepsilon_{\mathrm{PDE}}(x,y) \tag{7.13}$$

$$\varepsilon_{\text{ly, reflected photons}}(x,y) = \sum_{i}^{N_{\gamma,\mathrm{refl}}} \varepsilon_{\mathrm{refl}}^{\mathrm{fibre}}(x,y) \cdot \varepsilon_{\mathrm{PDE}}(x,y) \tag{7.14}$$

The work for the LYAM simulation was published as an LHCb internal technical note, see Ref. [143].

7.3.4 Implementation in the LHCb Software Framework

This subsection describes the integration of the LYAMs in the LHCb software framework. Together with their implementation in the LHCb software package `Boole`, the LYAM tools allow to produce different LYAMs with for different integrated luminosities, e.g. for studies of the LHCb upgrade and in the future also for the production of simulated decay samples for physics analyses.

In short, the energy deposited by a simulated particle hit is scaled with the value of the LYAM in the corresponding bin. Direct and reflected signal are treated separately and the latter is attenuated additionally by the value for the mirror reflectivity. The energy is converted to an expected mean number of photons by a global scaling factor. A Poisson random number is drawn for each fibre to get the number of photons seen by the SiPMs for the specific events. Each photon is assigned an arrival time, which is used to add the direct and the reflected photons respecting the time depended behaviour of the read-out electronics.

The complete simulation chain of the SciFi tracker is presented in detail in Ref. [144], the following paragraphs briefly describe the implementation of the LYAMs. The energy deposited in the tracker by a simulated particle hit (`MCHit`) is simulated by the `Gauss` application and distributed to different fibres in `Boole`. Here, the light yield attenuation maps are used to convert the deposited energy to an expected amount of detected photons. This is done for direct and reflected photons. The expected number of photons from a `MCHit` is given by

$$\overline{n}_p = s \cdot \varepsilon_{\mathrm{ly}} \cdot E_{\mathrm{hit}} \tag{7.15}$$

with $p \in \{\text{direct, reflected}\}$, the deposited energy, E_{hit}, and a constant scaling factor s. This factor is used to tune the overall light yield of the simulation to match the results from measurements in so called test beam campaigns, where SciFi fibre mats are irradiated with e.g. pions, to measure certain parameters, e.g. the light yield. The

Table 7.2 – Format and components of the `XML`-file for a light yield attenuation map. The length of the arrays is given in terms of the number of bins n in x and y direction.

Array	Length	Description
`x_edges`	$n_x + 1$	Bin boundaries in x direction
`y_edges`	$n_y + 1$	Bin boundaries in y direction
`eff_dir`	$n_x \cdot n_y$	Attenuation coefficients for direct photons
`eff_refl`	$n_x \cdot n_y$	Attenuation coefficients for reflected photons

attenuation coefficient $\varepsilon_{\text{ly}}(x_{\text{hit}}, y_{\text{hit}})$ is determined by a look-up operation on the corresponding light yield attenuation map at the hit coordinates $(x_{\text{hit}}, y_{\text{hit}})$. Reflected photons are attenuated additionally with the mirror reflectivity. Since the attenuation maps represent only the upper right quarter of the symmetrical SciFi tracker, the absolute values of the hit coordinates are used. No interpolation is performed between the bins of the map. Based on this expected value $\overline{n}_p$, the number of photons is drawn from a Poisson distribution.

The attenuation maps are stored in the so called *simulation conditions* (`SimCond`) database. This database is used to store different parameters, that are needed in the LHCb detector simulation and it is part of the LHCb *conditions database* (`CondDB`) [145, 146]. The values stored in these databases are static that means that they do not change between different events. The `CondDB` is based on `XML`-files, which are stored in several `Git` repositories. To be able to simulate the LHCb detector with different stages of an irradiated SciFi tracker, there are multiple attenuation maps stored in the `SimCond` database: the default map, corresponding to $50\,\text{fb}^{-1}$, as well as maps corresponding to $1\,\text{fb}^{-1}$, $10\,\text{fb}^{-1}$, $25\,\text{fb}^{-1}$ and $100\,\text{fb}^{-1}$. For a detector simulation at the start of Run III, it exists also an attenuation map with no irradiation.

The `XML`-file for the LYAM includes information about the binning scheme, as well as the attenuation coefficients from direct and reflected photons for each bin. The layout of the attenuation map bins is described by two arrays, which contain the bin edges in x and y direction. The two arrays that contain the attenuation coefficients for direct and reflected photons are produced by flattening the two-dimensional histograms of the LYAMs. In the area of the beam pipe hole the values of the attenuation coefficients are set to zero. The bins above the beam pipe at 100.5 mm are filled by the excitation points at 115.5 mm. Table 7.2 summarizes the values, which are read in from the conditions database.

In `Boole` the LYAMs are implemented by the so called `MCFTG4AttenuationTool`. The user can switch between the previously used parametric attenuation model and the new attenuation maps described here. A comparison between a parametric attenuation model and the LYAM approach is shown in Section 7.4.2. In course of a simulation of the detector response with `Boole`, the LYAMs are loaded into the random access memory, which avoids multiple queries to the `XML`-database for each simulated event.

7.4 Results

This section shows a discussion of the light yield attenuation maps as well as a comparison of an alternative parametric attenuation model with the newly introduced light yield attenuation maps.

7.4.1 LYAM Discussion

The *light yield attenuation maps* (LYAMs) show the light yield attenuation coefficients $\varepsilon_{\mathrm{ly}}$, which is calculated as the ratio of detected photons and the number of generated photons for different positions in the upper right quarter of the SciFi tracker. Figure 7.12 show the nominal LYAM of direct and mirror reflected photons for an irradiation corresponding to $50\,\mathrm{fb}^{-1}$ of data taking. The maps contain the light yield attenuation coefficients $\varepsilon_{\mathrm{ly}}$ calculated for every bin of the FLUKA dose map (see Section 7.3.3). Here, the additional attenuation from radiation damage was modelled with the power law model, as explained in Eq. (7.2), Section 7.2.3. The values for $\varepsilon_{\mathrm{ly}}$ range from 0.006 (0.002) in the vicinity of the beam pipe hole to 0.032 (0.009) for direct (mirror reflected) photons in the upper right region the SciFi tracker quarter.[1]
To be able to draw direct conclusions from these LYAMs without having values for the actual light yields, two ratios are calculated for further investigations.

Irradation Effects

In order to investigate the effect of the irradiation on the light yield, the ratio

$$r_{\mathrm{ly,irrad}} = \mathrm{LYAM}_{50\,\mathrm{fb}^{-1}}/\mathrm{LYAM}_{0\,\mathrm{fb}^{-1}} \tag{7.16}$$

is computed. Furthermore, the maps for direct and mirror reflected photons are combined bin-wise by taking into account a mirror reflectivity of 75 %:

$$r_{\mathrm{ly,irrad}} = r_{\mathrm{ly,irrad,direct}} + 0.75 \cdot r_{\mathrm{ly,irrad,reflected}} \tag{7.17}$$

In contrast to the combination performed in `Boole`, timing effects from the SiPM electronics, e.g. shaping and integration of the signal, cannot be considered. Therefore this approach will yield only approximate results.
Comparing Fig. 7.13a and Fig. 7.13b, one can see that the overall relative light yield is smaller for the power law model than for the linear model. The mean relative light

---

[1] The main diminishing factor for the low light yield is the low rate of total reflections due to the isotropic production of scintillation photons. Therefore, the next sections only consider ratios.

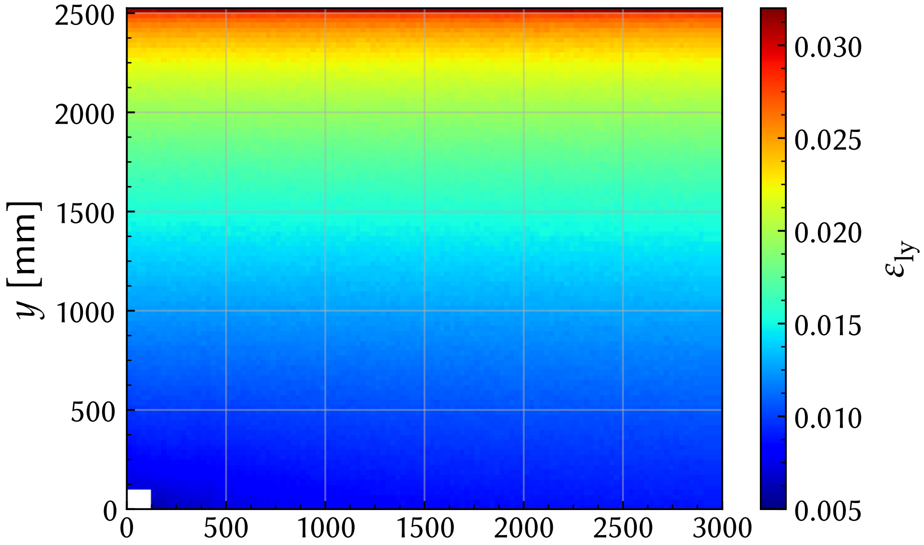

(a) Direct Photons

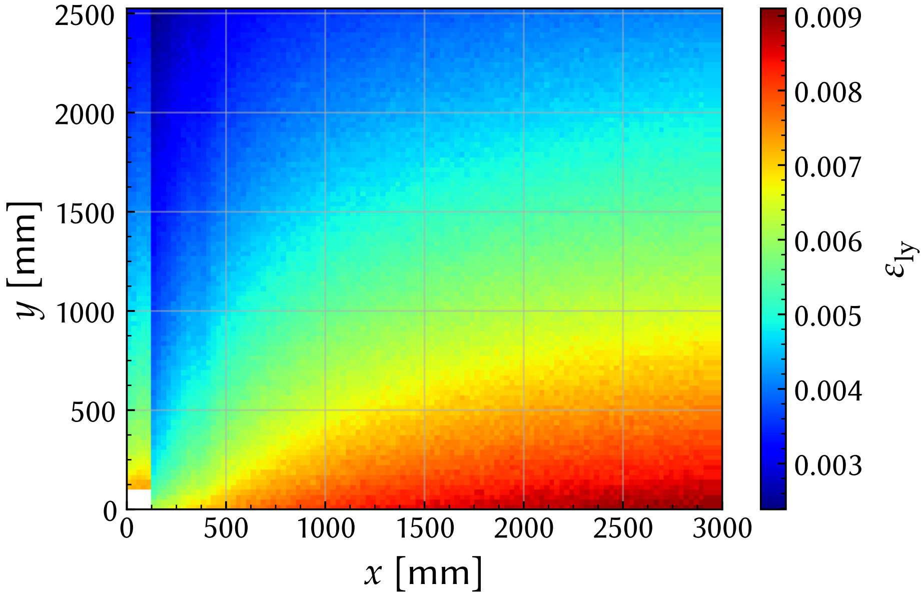

(b) Reflected Photons

Figure 7.12 – The light yield attenuation maps of (a) direct photons only and (b) mirror reflected photons only for an irradiation corresponding to 50 fb^{-1} of data taking.

yields for the whole quarter are calculated to

$$\begin{aligned}\bar{r}_{\text{ly,irrad,pow}} &= 0.90 \pm 0.07,\\ \text{and } \bar{r}_{\text{ly,irrad,lin}} &= 0.92 \pm 0.07\end{aligned}$$

which further decreases to 0.853 ± 0.020 and 0.879 ± 0.018 in the inner region $x, y \in [0, 1]$ m for the power law and linear model, respectively.
However, in direct proximity to the beam pipe, the linear model description yields lower relative light yields, which is shown in Fig. 7.14. While the "worst case" bin, closest to the beam pipe, has a relative light yield of 62 % for the power law model, it drops to 55 % for the linear model. The means of the relative light yields for the region $x, y \in [0, 500]$ mm are calculated to

$$\begin{aligned}&0.776 \pm 0.019,\\ \text{and } &0.782 \pm 0.021\end{aligned}$$

for the power law and the linear model respectively.
The on average reduced light yield is going to have a negative impact on the tracking efficiency of the SciFi tracker over its lifetime. The magnitude of this effect is the subject of current research from, among others, the Dortmund SciFi group. Generally speaking, due to the reduced light yield, particle hits in the SciFi tracker will produce more often too few photons below the SiPM threshold. This in turn leads to a decreased single hit efficiency which lowers the tracking efficiency of the SciFi tracker.

Model Comparison

The effect of a lower relative light yield close to the beam pipe for the linear model can also be observed by looking at the ratio

$$r_{\text{ly,models}} = \text{LYAM}_{\text{lin},50\,\text{fb}^{-1}} / \text{LYAM}_{\text{pow},50\,\text{fb}^{-1}}, \tag{7.18}$$

which compares the two damage models that can be used in the simulation of the LYAMs (see Section 7.3.2). Figure 7.15 shows deviations of ±10 % for direct photons (Fig. 7.15a) and ±20 % for reflected photons (Fig. 7.15b) between the light yield attenuation coefficients ε_{ly} of the two models, with an average ratio of 1.01 ± 0.04 (1.02 ± 0.06) for direct (mirror reflected) photons. This effect can be explained by the fact, that the linear model yields into higher additional attenuations for higher doses compared to the power law model, see Eqs. (7.2) to (7.3) and Fig. 7.8. For this very same reason, the deviation between the two models is highest for the mirror reflected photons in the vicinity of the beam pipe, $x \in [125, 250]$ mm, which can be observed in Fig. 7.15b.

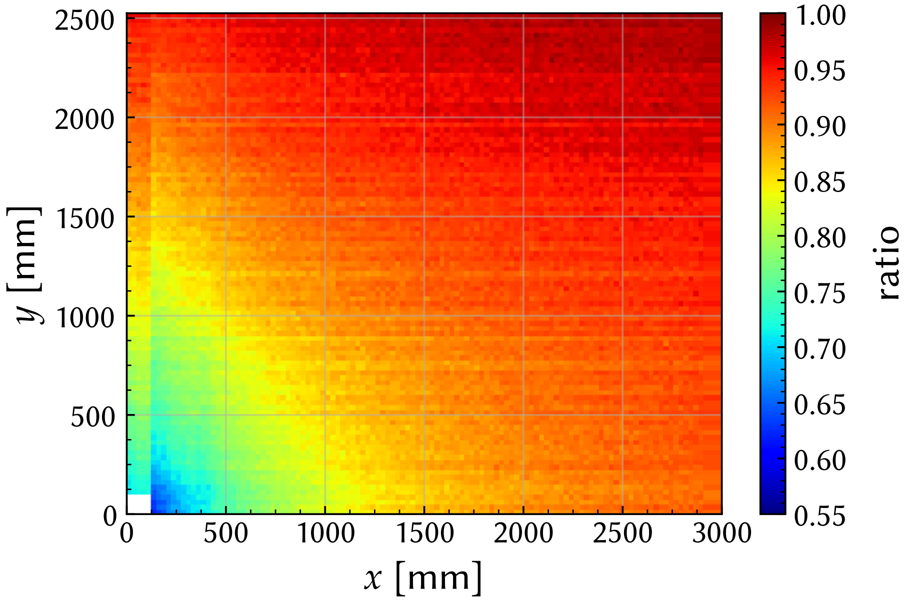

(a) Power Law Model

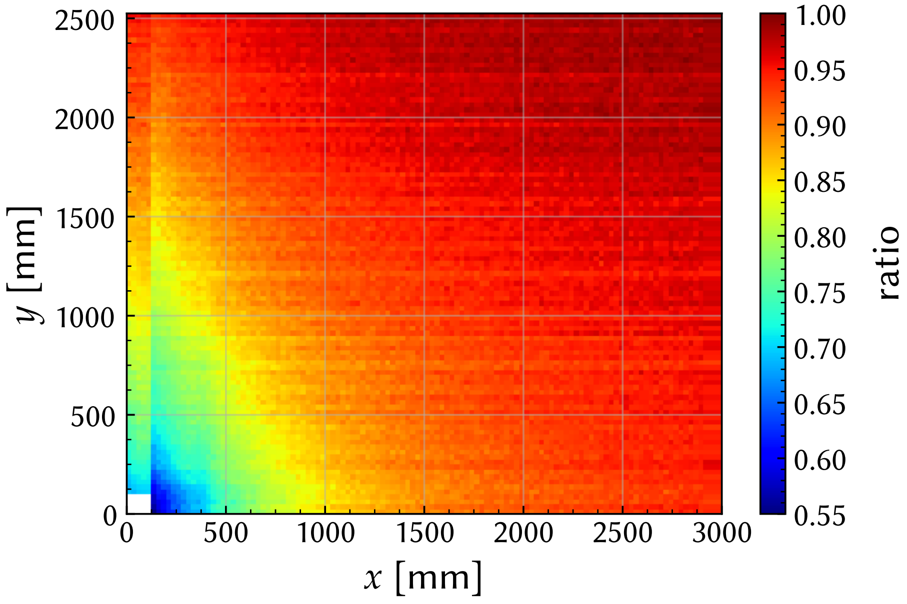

(b) Linear Model

Figure 7.13 – Ratios $\mathrm{LYAM}_{50\,\mathrm{fb}^{-1}}/\mathrm{LYAM}_{0\,\mathrm{fb}^{-1}}$ for (a) the power law model and (b) the linear model. The maps for direct and reflected photons were combined wrt. a mirror reflectivity of 75 % but without considering timing effects from the SiPM electronics, e.g. shaping and integration of the signal.

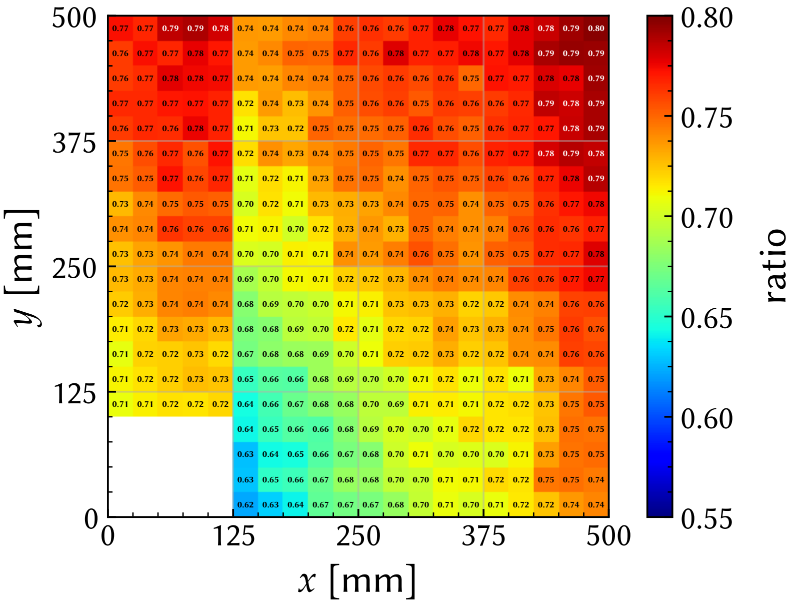

(a) Power Law Model, zoom

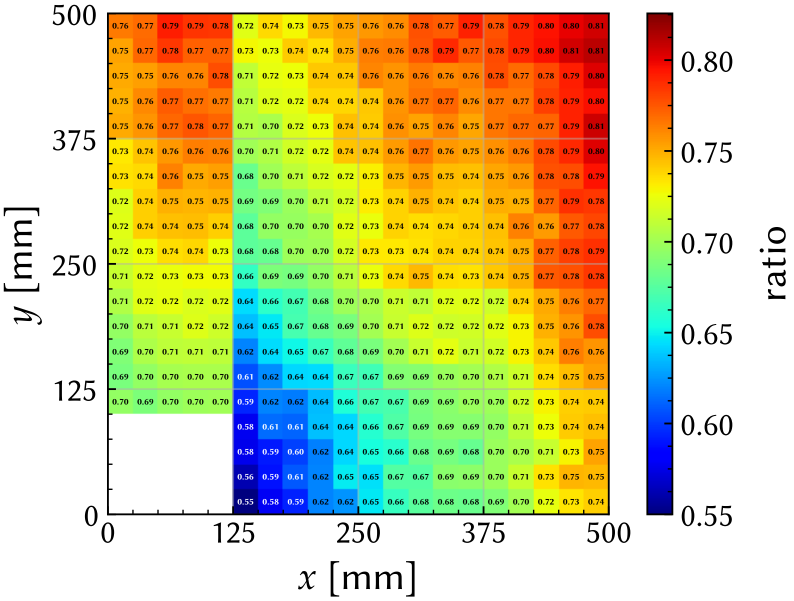

(b) Linear Model, zoom

Figure 7.14 – Zoom on the inner region, $x, y \in [0, 500]\,\mathrm{mm}$, with printed out ratios $\mathrm{LYAM}_{50\,\mathrm{fb}^{-1}}/\mathrm{LYAM}_{0\,\mathrm{fb}^{-1}}$ for (a) the power law model and (b) the linear model. The maps for direct and reflected photons were combined wrt. a mirror reflectivity of 75 % but without considering timing effects from the SiPM electronics, e.g. shaping and integration of the signal.

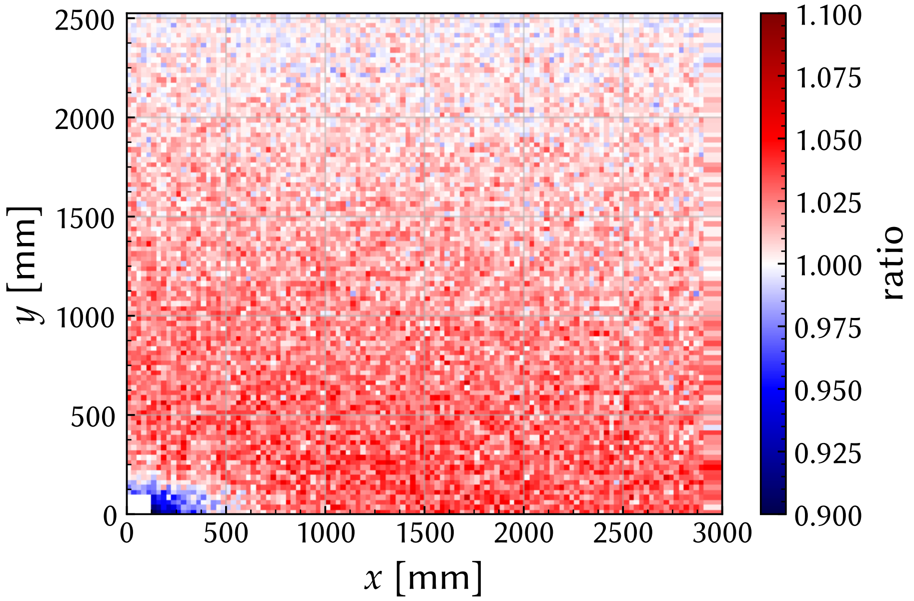

(a) Direct Photons

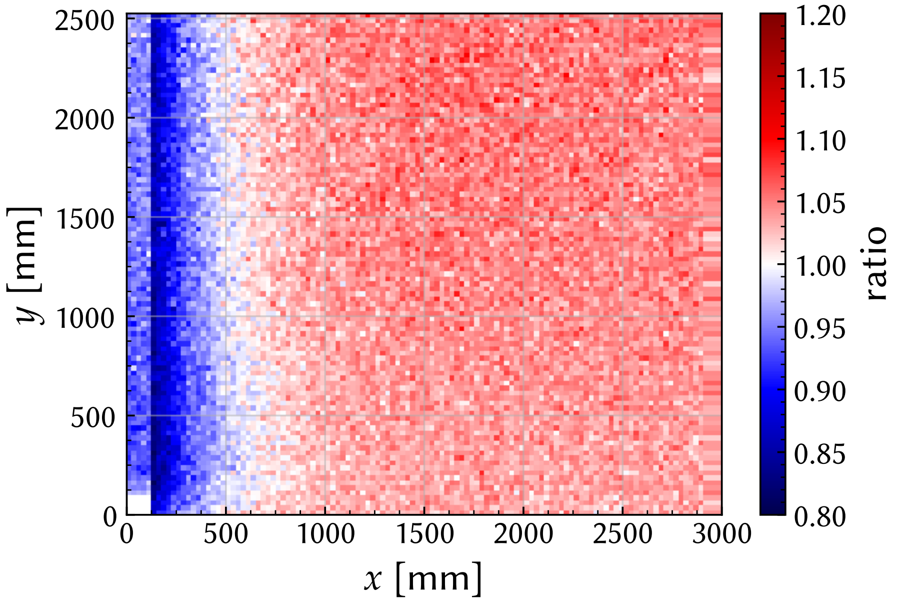

(b) Reflected Photons

Figure 7.15 – Ratios $\mathrm{LYAM}_{\mathrm{lin},50\,\mathrm{fb}^{-1}}/\mathrm{LYAM}_{\mathrm{pow},50\,\mathrm{fb}^{-1}}$ of the LYAMs simulated with the linear / power law model and an irradiation corresponding to $50\,\mathrm{fb}^{-1}$ of data taking: (a) direct photons only and (b) reflected photons only.

7.4.2 Comparison to Alternative Approaches

An alternative approach to include the additional light yield attenuation from radiation damage into the SciFi simulation was studied in Ref. [147]. When referring to a LYAM with no irradiation, it would be possible to calculate the additional attenuation from radiation damage from a theoretical model. Especially for the production of Signal Monte Carlo samples, this approach would save time and computing power, since it would no longer be necessary to simulate new attenuation maps for a given integrated luminosity.
Fig. 7.16 shows the ratios

$$r_{\mathrm{ly,theo}} = \mathrm{LYAM}_{\mathrm{theo},50\,\mathrm{fb}^{-1}} / \mathrm{LYAM}_{\mathrm{nom},50\,\mathrm{fb}^{-1}}, \tag{7.19}$$

of the nominal LYAM and the LYAM where the additional attenuation due to radiation was calculated with a theoretical model. While the overall agreement between the alternative approach and the nominal LYAM looks good for direct photons, see Fig. 7.16a, with only small areas of systematic deviations, the ratio for mirror reflected photons shows large areas which deviate systematically, see Fig. 7.16b. In fact, the theoretical model seems to underestimate the attenuation from irradiation for fibres in the vicinity of the beam pipe, which are affected by higher doses, while it overestimates the attenuation for fibres further away from the beam pipe. This effect is further verified when looking at the relative error

$$\sigma_{\mathrm{ly,theo}} = \frac{|\mathrm{LYAM}_{\mathrm{nom},50\,\mathrm{fb}^{-1}} - \mathrm{LYAM}_{\mathrm{theo},50\,\mathrm{fb}^{-1}}|}{\mathrm{LYAM}_{\mathrm{nom},50\,\mathrm{fb}^{-1}}}, \tag{7.20}$$

which is shown in Fig. 7.17. While the mean error is ~0.9 % for direct photons, it is calculated to ~3.2 % for mirror reflected photons. Since the deviations are higher for mirror reflected photons and direct photons produced close to the mirror, see Fig. 7.16a, it may be correlated with the travelled distance of the detected photons. Further studies will be required to understand these systematic differences between the two models.

In conclusion, the comparison of the LYAMs with the alternative approach of calculating the light yield attenuation from a theoretical model shows that the latter is no suitable alternative to the LYAMs concerning the simulation of light yield attenuation coefficients for the simulation of the LHCb detector.

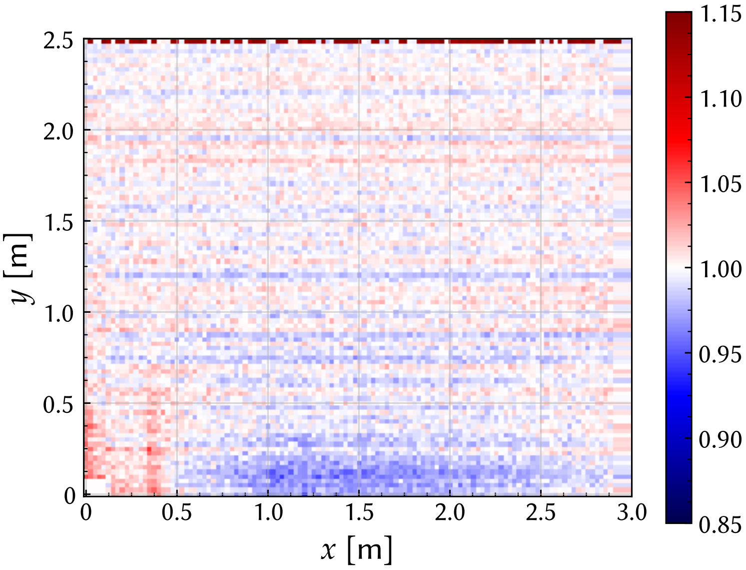

(a) Direct photons

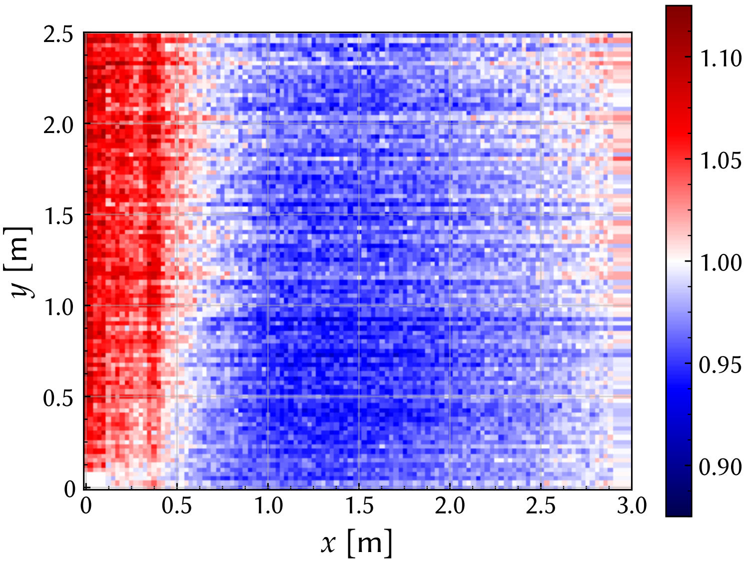

(b) Reflected photons

Figure 7.16 – Ratio $\mathrm{LYAM}_{\mathrm{theo},50\,\mathrm{fb}^{-1}}/\mathrm{LYAM}_{\mathrm{nom},50\,\mathrm{fb}^{-1}}$ of the nominal LYAM and light yield calculated with the alternative approach for (a) direct photons and (b) mirror reflected photons. Plots from [147].

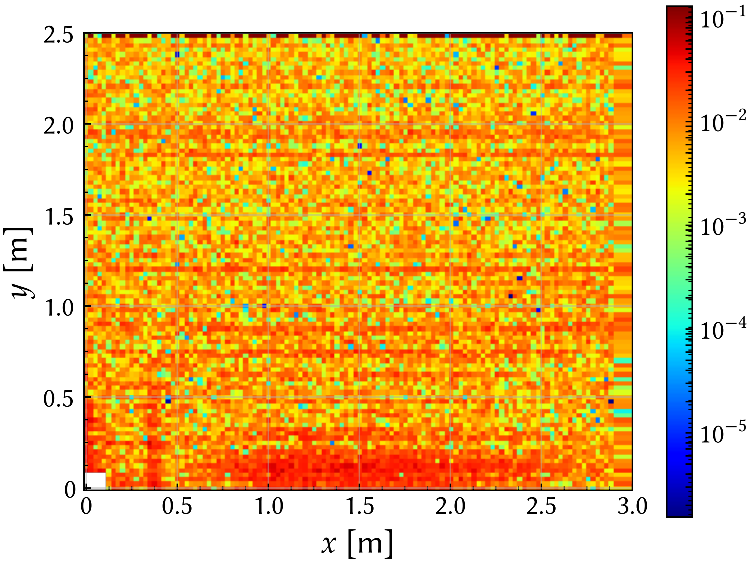

(a) Direct photons

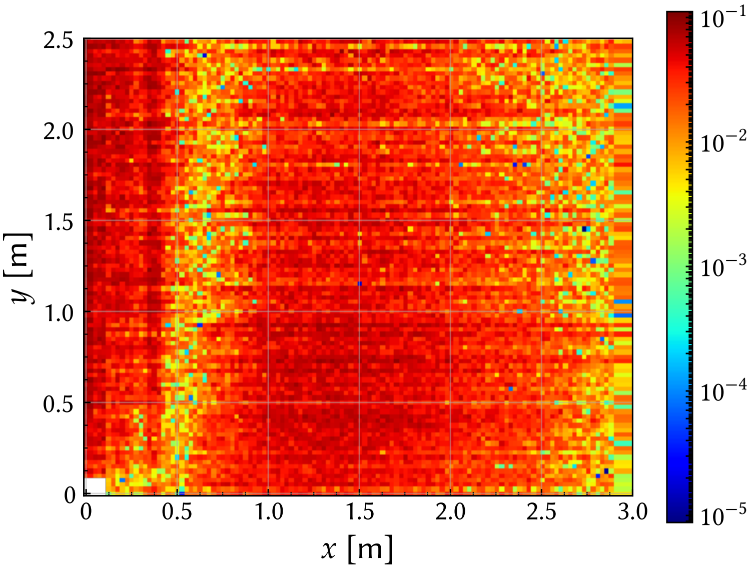

(b) Reflected photons

Figure 7.17 – Relative error of the light yield calculated with the alternative approach for (a) direct photons and (b) reflected photons. While the mean error is only 0.9 % for direct photons, it is higher for reflected photons with 3.2 %. Plots from [147].

Conclusion

Even though the measurements published by the collaborations of the LHC experiments in the last years confirm the success of the Standard Model of Particle Physics, the important open questions remain unanswered, which renders the existence of new physics beyond the SM undeniable. One example is that the current theory of $\mathcal{CP}$ violation and its observed magnitude are insufficient to explain the asymmetry of matter and antimatter in the universe.
The work presented in this thesis comprises two different fields of particle physics: The first part of the thesis examines the analysis of the decays $B^0 \to \phi K^0_S$ and $B^0_s \to K^0_S K^0_S$, and provides a branching ratio computation of the latter decay relative to the first one. The second part of the thesis is dedicated to the author's contribution for the simulation of the SciFi tracker, which is foreseen for the upgrade of the LHCb detector during the Long Shutdown 2 of the LHC. Both parts of the thesis are summarised separately in the following paragraphs.

Measurement of the Branching Ratio $\mathcal{B}(B^0_s \to K^0_S K^0_S)$

This thesis presents a measurement of the branching ratio of the decay $B^0_s \to K^0_S K^0_S$, normalised to the branching ratio of the decay $B^0 \to \phi K^0_S$ in order to reduce systematic uncertainties. The absence of a characteristic signature as well as the decay topology of this decay, i.e. the decay of a neutral particle into two neutral long-lived intermediate particles, make this task challenging.
The first and to date only published analysis of the decay $B^0_s \to K^0_S K^0_S$ is the measurement of the branching fraction $\mathcal{B}(B^0_s \to K^0 \bar{K}^0)$ that has been accomplished in 2015 by the Belle experiment [53, 54]:

$$\mathcal{B}(B^0_s \to K^0 \bar{K}^0) = \left(19.6^{+5.8}_{-5.1}\,(\text{stat}) \pm 1.0\,(\text{syst}) \pm 2.0\, \left(N_{B^0_s \bar{B}^0_s}\right)\right) \cdot 10^{-6}\,.$$

With data recorded by the LHCb experiment in 2011–2012, the work presented in this thesis leads to a branching ratio for $B^0_s \to K^0_S K^0_S$ decays of

$$\begin{aligned} \mathcal{B}(B^0_s \to K^0_S K^0_S) &= \left(22.9 \pm 7.3\,(\text{stat}) \pm 1.7\,(\text{syst}) \pm 2.2\,(\mathcal{B}(B^0 \to \phi K^0_S)) \pm 1.3\,({}^{f_d}\!/\!{}_{f_s})\right) \cdot 10^{-6}\,, \\ \Rightarrow \mathcal{B}(B^0_s \to K^0 \bar{K}^0) &= \left(45.9 \pm 14.5\,(\text{stat}) \pm 3.5\,(\text{syst}) \pm 4.5\,(\mathcal{B}(B^0 \to \phi K^0_S)) \pm 2.7\,({}^{f_d}\!/\!{}_{f_s})\right) \cdot 10^{-6}\,. \end{aligned}$$

With a statistical significance of 3.7 σ (3.2 σ including internal and external systematic uncertainties) this result is dominated by its statistical uncertainty. However, it is compatible within 1.7 σ with the measurement from Belle, as well as theory predictions for $\mathcal{B}(B_s^0 \to K^0\bar{K}^0)$ from different theoretical models (see Table 1.1), which are all in the order of $20 \cdot 10^{-6}$. Due to improved selection efficiencies, an increased fraction of candidates reconstructed in the LL and LD subsets, and a Run II dataset with ~ 1.5 the amount of B mesons, the statistical error is expected to drop by ∼50 % of its current value for the final measurement with the combined dataset of Run I and Run II. The final result will be published by the co-author of this analysis [6]. Even more improvement can be expected by including the data recorded in 2017–2018. Because of the introduction of a specialised trigger line, the fully downstream reconstructed subset is added to the signal yield, leading to a 40 % increase in signal candidates.
Another promising outlook can be given for a potential standalone analysis of the decay $B^0 \to \phi K_S^0$, when also including the data recorded in 2017–2018. Assuming constant selection efficiencies, an additional 1648 ± 159 signal candidates can be expected, leading to a total of 2455 ± 164 signal candidates. This should allow for a time dependent analysis of $\mathcal{CP}$ violation, providing an interesting probe for physics beyond the SM, because the FCNC process of this decay may be sensitive to possible new physics contributions, thus enhancing the $\mathcal{CP}$ parameter measured in this decay.

Light Yield Attenuation Maps

The work presented in the second part of this thesis was the main contribution for the construction of a software framework that allows to simulate lookup maps for the light yield attenuation in scintillating fibres as a function of the hit position, so called *light yield attenuation maps* (LYAMs). Since the performance of the SciFi tracker depends mainly on the light yield, it is necessary to know the correct light yield attenuation in scintillating fibres as a function of the integrated luminosity. However, the radiation induced damage of scintillating fibres is underestimated, when trying to extrapolate the expected damage after long-term irradiation at low dose rates from measurements with short-term irradiation at high dose rates. Furthermore, each measurement only provides a discrete data point for a given dose rate. Thus, rendering the simulation of these maps indispensable. The light yield attenuation maps show the relative number of detected photons divided by the number of generated photons, the light yield attenuation coefficients, for different positions in the SciFi tracker. As inputs, the simulation of the LYAMs uses simulated dose maps from the MC generator FLUKA, a wavelength dependent photon detection efficiency for the photon detectors (SiPMs), as well as a wavelength dependent model for the description of light yield attenuation in the scintillating fibres. The later comprises an empirical model for the additional attenuation from radiation damage that was fitted to measured data points. In summary, the computed light yield attenuation coefficients are the result of the efficiency of photons being caught by the wavelength shifter, the trapping efficiency of the wavelength-shifted photons in the fibre, the attenuation along the fibre from intrinsic and extrinsic effects, and the photon detection efficiency of the silicon photomultipliers. The modular design of the LYAM simulation enables to change certain parameters to account for e.g. unexpected radiation levels, and altered parameters of the detectors, or the scintillating fibres, one example being that a change of the wavelengths dependence of the photon detection efficiency of the SiPMs would be described correctly by newly simulated LYAMs. In conclusion, the LYAM tools together with the implementation in `Boole` allow for an easy simulation of the correct light yield attenuation for different integrated luminosities in the LHCb detector. In addition to studies for the LHCb upgrade, e.g. the precise tuning of new tracking algorithms, this also enables the LHCb collaboration to use the light yield attenuation maps for the production of simulated decay samples for physics analyses in the upcoming third running period of the LHC.

As a final summary, it can be concluded that the work presented in this thesis makes important contributions for current and future measurements of decay channels with purely hadronic final states at the LHCb experiment: by investigating the decay channels $B_s^0 \to K_S^0 K_S^0$ and $B^0 \to \phi K_S^0$, and furthermore contributing to the upgrade of the LHCb tracking system.

A Supplementary Material

A.1 Signal Candidate Selection of $B \to \phi K^0_S$ Decays

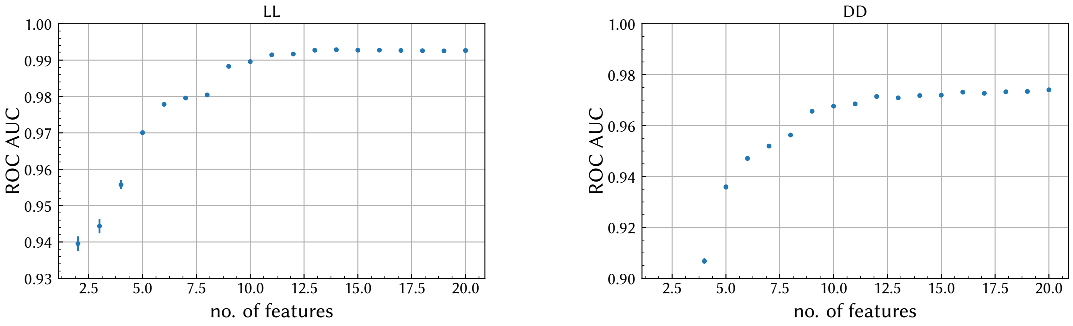

(a) Run I LL **(b)** Run I DD

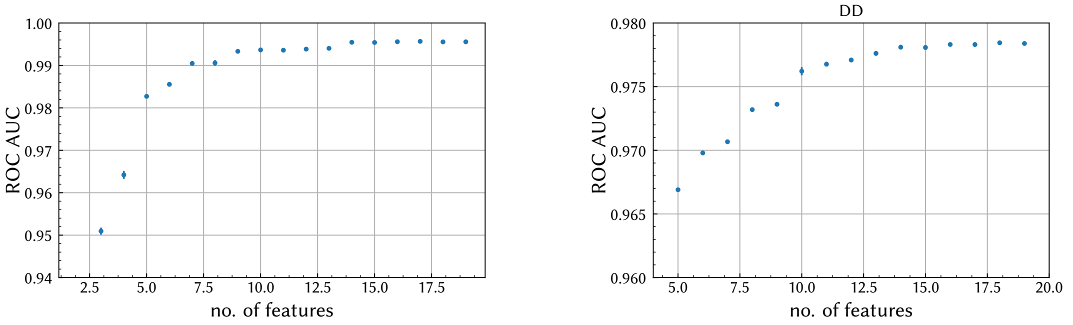

(c) Run II LL **(d)** Run II DD

Figure A.1 – The number of features taken from the ranked feature list vs. the obtained ROC AUC score with this set of features, shown for (a)/(b) Run I LL/DD and (c)/(d) Run II LL/DD.

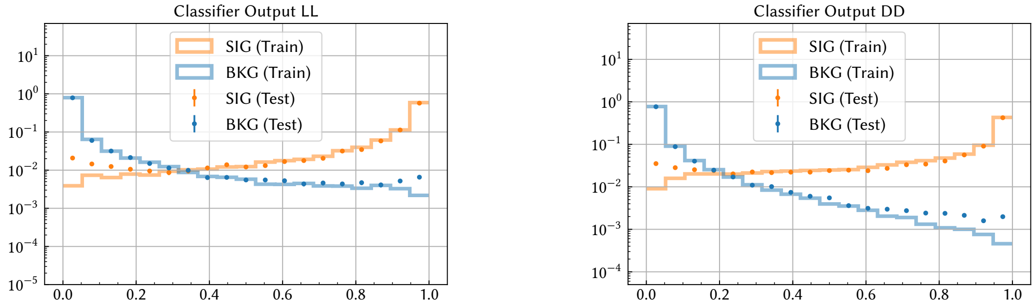

(a) Run I LL **(b)** Run I DD

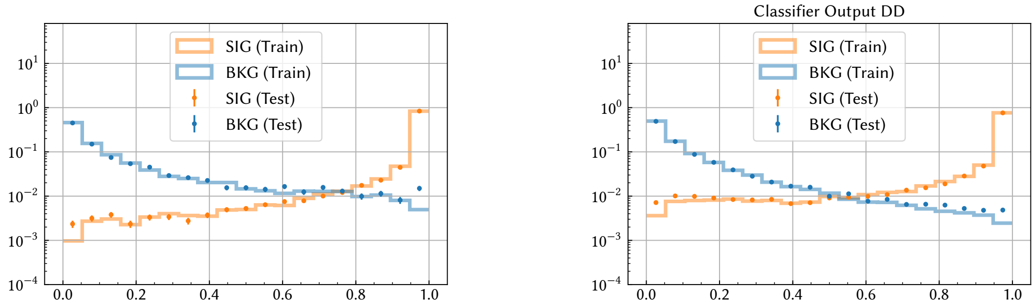

(c) Run II LL **(d)** Run II DD

Figure A.2 – The output of the XGBoost classifiers for training and testing datasets, shown for (a)/(b) Run I LL/DD and (c)/(d) Run II LL/DD. Note that events are split into two thirds for training and one third for testing and the number of Signal MC events (SIG) is limited, even more so for the LL subset.

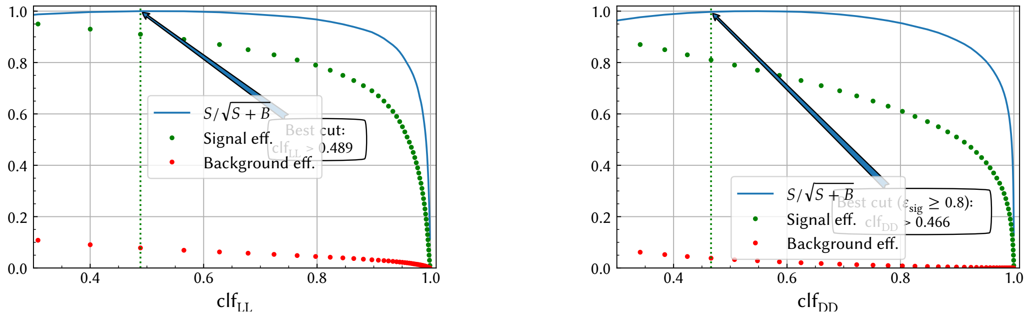

(a) Run I LL **(b)** Run I DD

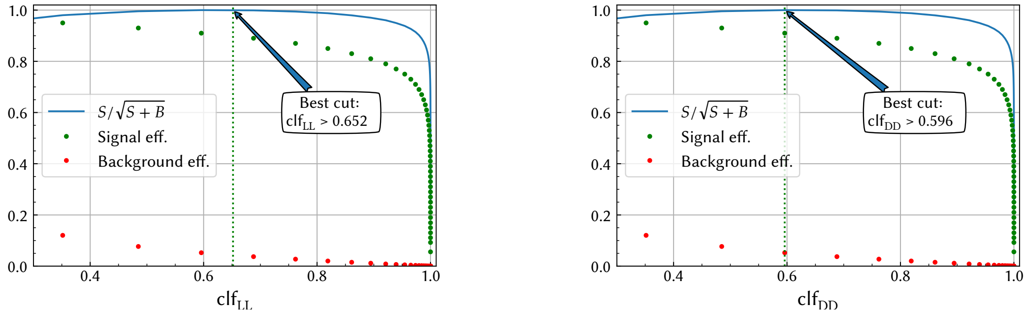

(c) Run II LL **(d)** Run II DD

Figure A.3 – Cut point optimisations for the two classifiers for (a)/(b) Run I LL/DD and (c)/(d) Run II LL/DD.

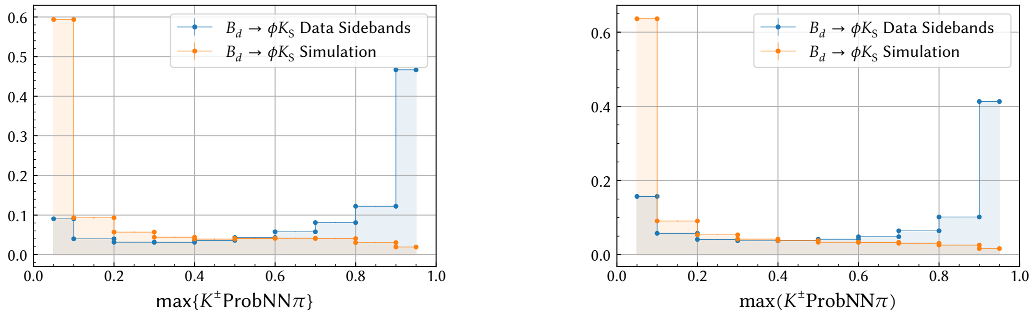

(a) LL **(b)** DD

Figure A.4 – Comparison of the variable $\max(K^{+}\mathrm{ProbNN}\pi, K^{-}\mathrm{ProbNN}\pi)$ in simulation (orange) and mass sidebands (blue) for Run I (a) LL and (b) DD.

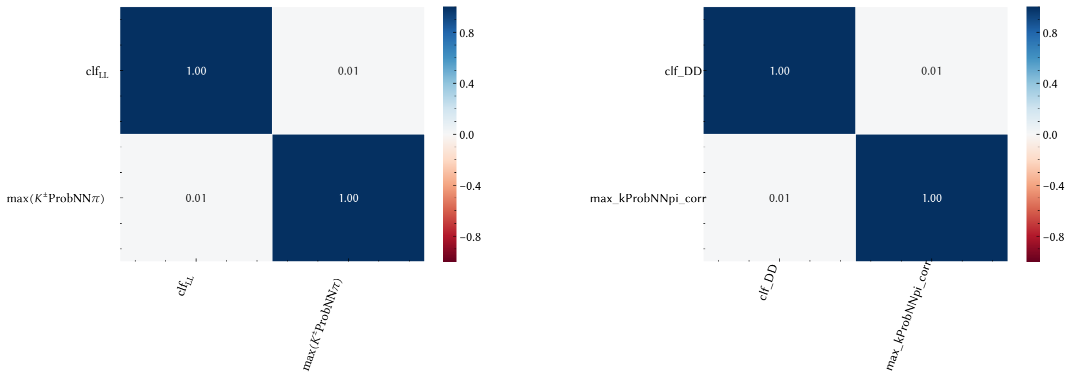

(a) Run I LL **(b)** Run I DD

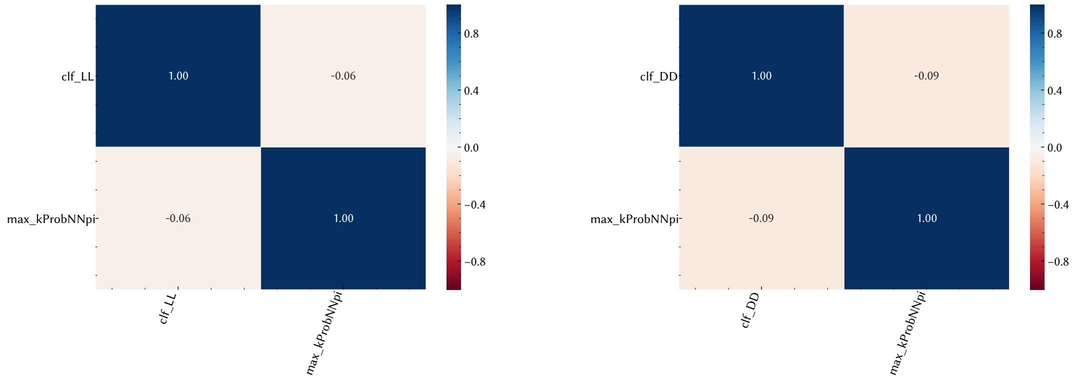

(c) Run II LL **(d)** Run II DD

Figure A.5 – Correlation between the variable max(K^+ProbNNπ, K^-ProbNNπ) and the classifier output (a)/(b) Run I LL/DD and (c)/(d) Run II LL/DD.

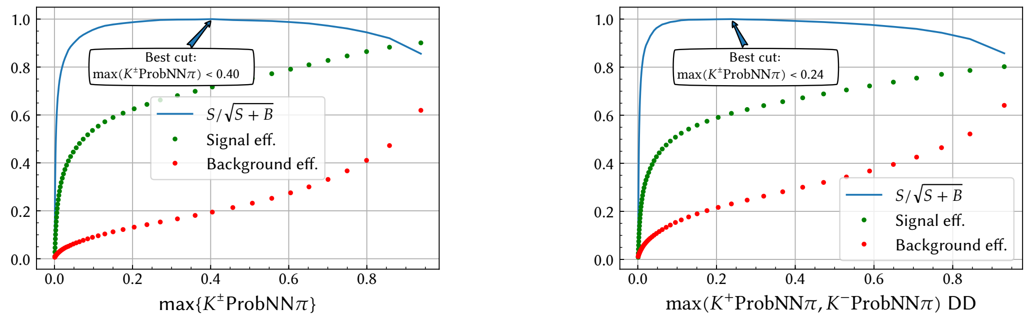

(a) Run I LL

(b) Run I DD

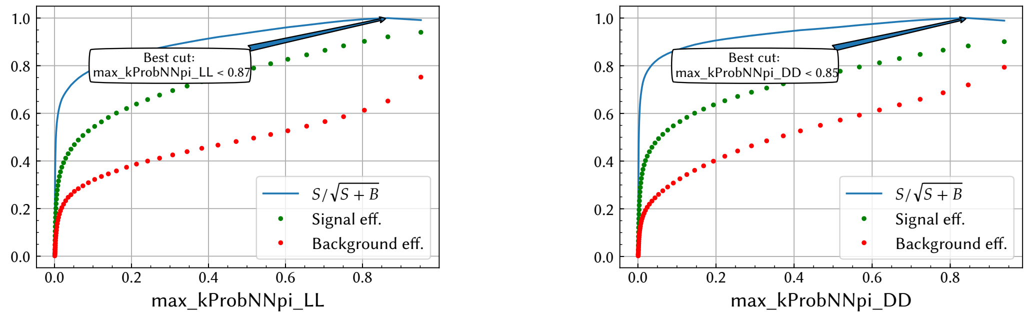

(c) Run II LL

(d) Run II DD

Figure A.6 – Cut point optimisation of the variable max(K^{+}ProbNNπ, K^{-}ProbNNπ) for (a)/(b) Run I LL/DD and (c)/(d) Run II LL/DD.

A.2 Mass Parametrization and Signal Yield Extraction – $B \to \phi K^0_S$

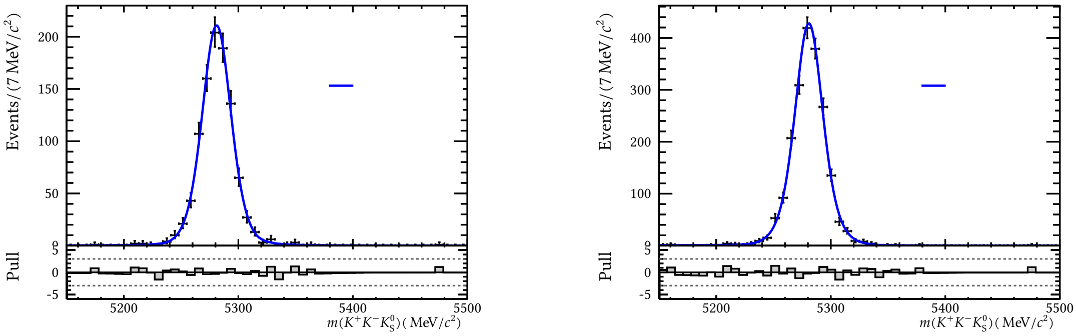

(a) Run I LL

(b) Run I DD

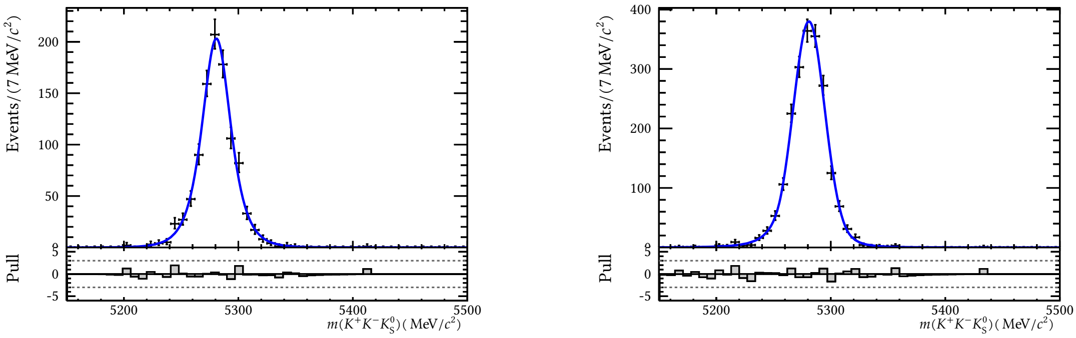

(c) Run II LL

(d) Run II DD

Figure A.7 – Fit of the Hypatia PDF to the simulated B^0 mass distribution with DTF constraints on the K^0_S mass and the PV for (a)/(b) Run I LL/DD and (c)/(d) Run II LL/DD. The events in the simulated dataset are scaled to 500 (1000) events for LL (DD), in order to prevent over-fitting.

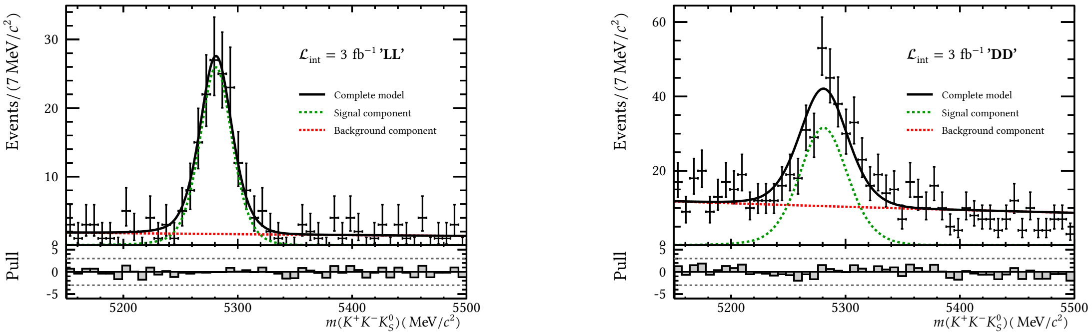

(a) Run I LL

(b) Run I DD

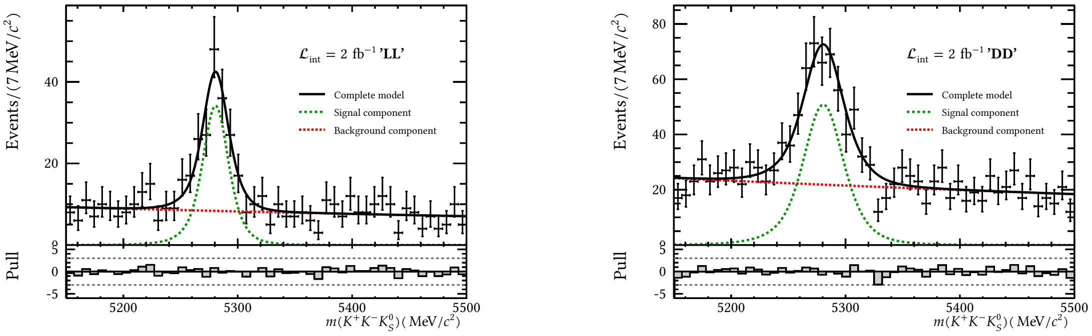

(c) Run II LL

(d) Run II DD

Figure A.8 – Fit to the B^0 mass distribution with DTF $K^0_{\rm S}$ mass and PV constraints for (a)/(c) Run I/Run II LL and (b)/(d) Run I/Run II DD.

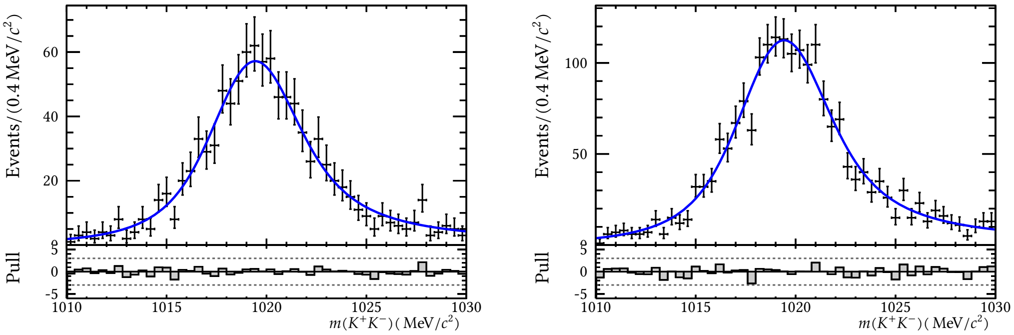

(a) Run I LL

(b) Run I DD

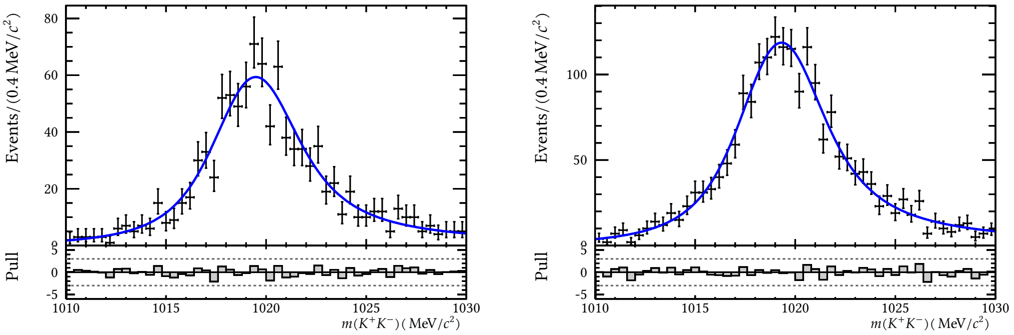

(c) Run II LL

(d) Run II DD

Figure A.9 – Fit to the simulated invariant K^+K^- mass distribution for (a)/(c) Run I/Run II LL and (b)/(d) Run I/Run II DD. The events in the simulated dataset are scaled to 1000 (2000) events for LL (DD), in order to prevent over-fitting.

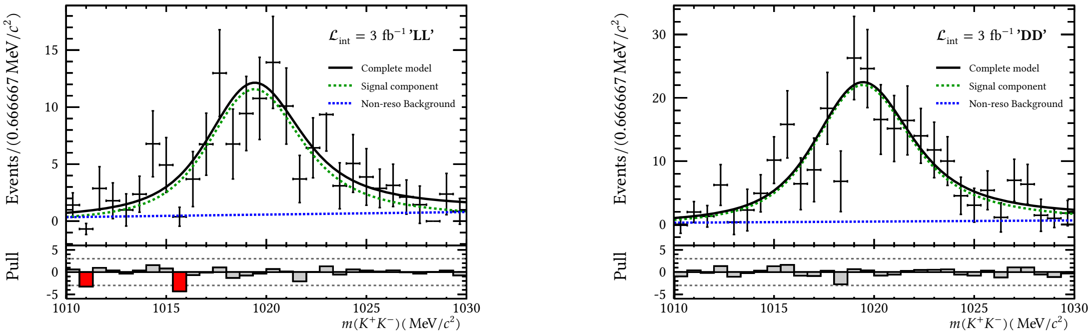

(a) Run I LL **(b)** Run I DD

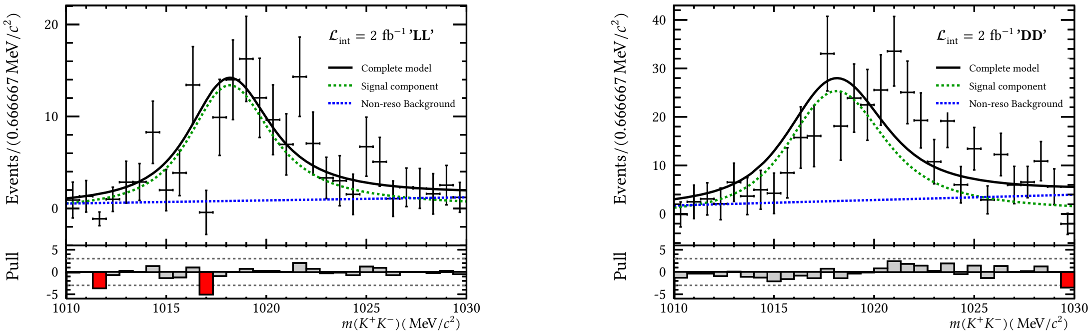

(c) Run II LL **(d)** Run II DD

Figure A.10 – Fit to the sWeighted invariant K^+K^- mass distribution for (a)/(c) Run I/Run II LL and (b)/(d) Run I/Run II DD.

Bibliography

[1] S. Glashow, *Partial Symmetries of Weak Interactions*, Nucl. Phys. **22** (1961) 579–588, DOI: `10.1016/0029-5582(61)90469-2`.

[2] A. Salam and J. Ward, *Electromagnetic and weak interactions*, Physics Letters **13**.2 (1964) 168–171, ISSN: 0031-9163, DOI: `https://doi.org/10.1016/0031-9163(64)90711-5`, `http://www.sciencedirect.com/science/article/pii/0031916364907115`.

[3] S. Weinberg, *A Model of Leptons*, Phys. Rev. Lett. **19** (21 1967) 1264–1266, DOI: `10.1103/PhysRevLett.19.1264`.

[4] A. Sakharov, *Violation of CP Invariance, C Asymmetry, and Baryon Asymmetry of the Universe*, Pisma Zh. Eksp. Teor. Fiz. **5** (1967) 32–35, DOI: `10.1070/PU1991v034n05ABEH002497`.

[5] J. Christenson *et al.*, *Evidence for the 2π Decay of the K_2^0 Meson*, Phys. Rev. Lett. **13** (1964) 138–140, DOI: `10.1103/PhysRevLett.13.138`.

[6] T. Schmelzer, *Observation of the Decay $B_s^0 \to K_S^0 K_S^0$ at the LHCb Experiment*, PhD thesis, TU Dortmund University, in preparation.

[7] R. Aaij *et al.*, *Letter of Intent for the LHCb Upgrade*, tech. rep. CERN-LHCC-2011-001. LHCC-I-018, Geneva: CERN, 2011, `https://cds.cern.ch/record/1333091`.

[8] R. Aaij *et al.*, *LHCb Tracker Upgrade Technical Design Report* (2014), `http://cds.cern.ch/record/1647400`.

[9] P. Ade *et al.*, *Planck 2013 results. I. Overview of products and scientific results* (2013), `arXiv:1303.5062 [astro-ph.CO]`.

[10] M. Aaboud *et al.*, *Observation of Higgs boson production in association with a top quark pair at the LHC with the ATLAS detector*, Phys. Lett. **B784** (2018) 173–191, DOI: `10.1016/j.physletb.2018.07.035`, `arXiv:1806.00425 [hep-ex]`.

[11] A. M. Sirunyan *et al.*, *Observation of $t\bar{t}H$ production*, Phys. Rev. Lett. **120**.23 (2018) 231801, DOI: `10.1103/PhysRevLett.120.231801,10.1130/PhysRevLett.120.231801`, `arXiv:1804.02610 [hep-ex]`.

[12] M. Aaboud *et al.*, *Observation of $H \to b\bar{b}$ decays and VH production with the ATLAS detector* (2018), `arXiv:1808.08238 [hep-ex]`.

[13] A. M. Sirunyan *et al.*, *Observation of Higgs boson decay to bottom quarks*, Phys. Rev. Lett. **121**.12 (2018) 121801, DOI: `10.1103/PhysRevLett.121.121801`, `arXiv:1808.08242 [hep-ex]`.

[14] M. Aaboud *et al.*, *Cross-section measurements of the Higgs boson decaying to a pair of τ leptons in proton–proton collisions at $\sqrt{s} = 13$ TeV with the ATLAS detector* (2018).

[15] A. M. Sirunyan *et al.*, *Observation of the Higgs boson decay to a pair of τ leptons with the CMS detector*, Physics Letters B **779** (2018) 283–316, ISSN: 0370-2693, DOI: `https://doi.org/10.1016/j.physletb.2018.02.004`, `http://www.sciencedirect.com/science/article/pii/S0370269318301035`.

[16] D. Griffiths, *Introduction to Elementary Particles*, 2nd, Wiley-VCH, 2011, ISBN: 3527406018.

[17] G. Branco, L. Lavoura, and J. Silva, *CP Violation*, Oxford Science Publications, 1999.

[18] D. Boutigny *et al.*, *The Babar physics book: Physics at an asymmetric B factory* (1998).

[19] E. Kou *et al.*, *The Belle II Physics Book* (2018), `arXiv:1808.10567 [hep-ex]`.

[20] M. Tanabashi *et al.*, *Review of Particle Physics*, Phys. Rev. **D98**.3 (2018) 030001, DOI: `10.1103/PhysRevD.98.030001`.

[21] R. Niet, *Measurement of CP Violation in in $B^0 \to [c\bar{c}]K^0_S$ Transitions at LHCb*, PhD thesis, TU Dortmund University, 2018, DOI: `10.17877/DE290R-19128`.

[22] G. Aad *et al.*, *Combined Measurement of the Higgs Boson Mass in pp Collisions at $\sqrt{s} = 7$ and 8 TeV with the ATLAS and CMS Experiments*, Phys. Rev. Lett. **114** (2015) 191803, DOI: `10.1103/PhysRevLett.114.191803`, `arXiv:1503.07589 [hep-ex]`.

[23] H. Georgi and S. L. Glashow, *Unified Weak and Electromagnetic Interactions without Neutral Currents*, Phys. Rev. Lett. **28** (22 1972) 1494–1497, DOI: `10.1103/PhysRevLett.28.1494`.

[24] D. J. Gross and F. Wilczek, *Asymptotically Free Gauge Theories I*, Phys. Rev. D **8** (10 1973) 3633–3652, DOI: `10.1103/PhysRevD.8.3633`, `http://link.aps.org/doi/10.1103/PhysRevD.8.3633`.

[25] H. D. Politzer, *Asymptotic freedom: An approach to strong interactions*, Physics Reports **14**.4 (1974) 129–180, ISSN: 0370-1573, DOI: `http://dx.doi.org/10.1016/0370-1573(74)90014-3`.

[26] M. Gell-Mann, *A Schematic Model of Baryons and Mesons*, Phys. Lett. **8** (1964) 214–215, DOI: `10.1016/S0031-9163(64)92001-3`.

[27] R. Aaij *et al.*, *Observation of $J/\psi\phi$ structures consistent with exotic states from amplitude analysis of $B^+ \to J/\psi\phi K^+$ decays*, Phys. Rev. Lett. **118**.2 (2017) 022003, DOI: `10.1103/PhysRevLett.118.022003`, `arXiv:1606.07895 [hep-ex]`.

[28] R. Aaij *et al.*, *Amplitude analysis of $B^+ \to J/\psi\phi K^+$ decays*, Phys. Rev. **D95**.1 (2017) 012002, DOI: `10.1103/PhysRevD.95.012002`, `arXiv:1606.07898 [hep-ex]`.

[29] R. Aaij *et al.*, *Observation of $J/\psi p$ resonances consistent with pentaquark states in $\Lambda_b^0 \to J/\psi K^- p$ decays*, Phys. Rev. Lett. **115** (2015) 072001, DOI: `10.1103/PhysRevLett.115.072001`, `arXiv:1507.03414 [hep-ex]`.

[30] F. Englert and R. Brout, *Broken Symmetry and the Mass of Gauge Vector Mesons*, Phys. Rev. Lett. **13** (9 1964) 321–323, DOI: `10.1103/PhysRevLett.13.321`, `http://link.aps.org/doi/10.1103/PhysRevLett.13.321`.

[31] P. W. Higgs, *Broken Symmetries and the Masses of Gauge Bosons*, Phys. Rev. Lett. **13** (16 1964) 508–509, DOI: `10.1103/PhysRevLett.13.508`, `http://link.aps.org/doi/10.1103/PhysRevLett.13.508`.

[32] G. S. Guralnik, C. R. Hagen, and T. W. B. Kibble, *Global Conservation Laws and Massless Particles*, Phys. Rev. Lett. **13** (20 1964) 585–587, DOI: `10.1103/PhysRevLett.13.585`, `http://link.aps.org/doi/10.1103/PhysRevLett.13.585`.

[33] M. Kobayashi and T. Maskawa, *CP-Violation in the Renormalizable Theory of Weak Interaction*, Progress of Theoretical Physics **49**.2 (1973) 652–657, DOI: `10.1143/PTP.49.652`, eprint: `http://ptp.oxfordjournals.org/content/49/2/652.full.pdf+html`, `http://ptp.oxfordjournals.org/content/49/2/652.abstract`.

[34] L.-L. Chau and W.-Y. Keung, *Comments on the Parametrization of the Kobayashi-Maskawa Matrix*, Phys. Rev. Lett. **53** (19 1984) 1802–1805, DOI: `10.1103/PhysRevLett.53.1802`, `https://link.aps.org/doi/10.1103/PhysRevLett.53.1802`.

[35] L. Wolfenstein, *Parametrization of the Kobayashi-Maskawa Matrix*, Phys. Rev. Lett. **51** (21 1983) 1945–1947, DOI: `10.1103/PhysRevLett.51.1945`, `https://link.aps.org/doi/10.1103/PhysRevLett.51.1945`.

[36] C. Jarlskog, *Commutator of the Quark Mass Matrices in the Standard Electroweak Model and a Measure of Maximal CP Violation*, Phys. Rev. Lett. **55** (1985) 1039, DOI: `10.1103/PhysRevLett.55.1039`.

[37] J. Charles *et al.*, *CP violation and the CKM matrix: Assessing the impact of the asymmetric B factories*, Eur. Phys. J. **C41** (2005) 1–131, DOI: `10.1140/epjc/s2005-02169-1`, `arXiv:hep-ph/0406184 [hep-ph]`, updated results and plots available at: `http://ckmfitter.in2p3.fr`.

[38] V. Weisskopf and E. P. Wigner, *Berechnung der natürlichen Linienbreite auf Grund der Diracschen Lichttheorie*, Z. Phys. **63** (1930) 54–73, DOI: `10.1007/BF01336768`.

[39] V. Weisskopf and E. Wigner, *Über die natürliche Linienbreite in der Strahlung des harmonischen Oszillators*, Z. Phys. **65** (1930) 18–29, DOI: `10.1007/BF01397406`.

[40] B. Winstein and L. Wolfenstein, *The Search for direct CP violation*, Rev. Mod. Phys. **65** (1993) 1113–1148, DOI: `10.1103/RevModPhys.65.1113`.

[41] K. G. Wilson and W. Zimmermann, *Operator product expansions and composite field operators in the general framework of quantum field theory*, Commun. Math. Phys. **24** (1972) 87–106, DOI: `10.1007/BF01878448`.

[42] G. Buchalla, A. J. Buras, and M. E. Lautenbacher, *Weak decays beyond leading logarithms*, Rev. Mod. Phys. **68** (1996) 1125–1144, DOI: `10.1103/RevModPhys.68.1125`, `arXiv:hep-ph/9512380 [hep-ph]`.

[43] A. J. Buras, *Flavor dynamics: CP violation and rare decays*, Subnucl. Ser. **38** (2002) 200–337, DOI: `10.1142/9789812778253_0005`, `arXiv:hep-ph/0101336 [hep-ph]`.

[44] K. G. Wilson, *Nonlagrangian models of current algebra*, Phys. Rev. **179** (1969) 1499–1512, DOI: `10.1103/PhysRev.179.1499`.

[45] M. Ciuchini, M. Pierini, and L. Silvestrini, *$B_{(s)} \to K^{(*)0}\bar{K}^{(*)0}$ Decays: The Golden Channels for New Physics Searches*, Phys. Rev. Lett. **100** (2008) 031802, DOI: `10.1103/PhysRevLett.100.031802`, `arXiv:hep-ph/0703137 [HEP-PH]`.

[46] B. Bhattacharya *et al.*, *Measuring β_s with $B_s \to K^{0(*)}\bar{K}^{0(*)}$ – a Reappraisal*, Phys. Lett. **B717** (2012) 403–408, DOI: `10.1016/j.physletb.2012.09.054`, `arXiv:1203.3435 [hep-ph]`.

[47] R. Aaij *et al.*, *Measurement of CP violation in $B_s^0 \to \phi\phi$ decays*, Phys. Rev. **D90**.5 (2014) 052011, DOI: `10.1103/PhysRevD.90.052011`, `arXiv:1407.2222 [hep-ex]`.

[48] H.-Y. Cheng, C.-K. Chua, and A. Soni, *Effects of final-state interactions on mixing-induced CP violation in penguin-dominated B decays*, Phys. Rev. **D72** (2005) 014006, DOI: `10.1103/PhysRevD.72.014006`, `arXiv:hep-ph/0502235 [hep-ph]`.

[49] R. Aaij *et al.*, *Measurement of CP violation in $B^0 \to J/\psi K_S^0$ decays*, Phys. Rev. Lett. **115** (2015) 031601, DOI: `10.1103/PhysRevLett.115.031601`, `arXiv:1503.07089 [hep-ex]`.

[50] R. Aaij *et al.*, *Measurement of CP violation in $B^0 \to J/\psi K_S^0$ and $B^0 \to \psi(2S)K_S^0$ decays*, JHEP **11** (2017) 170, DOI: `10.1007/JHEP11(2017)170`, `arXiv:1709.03944 [hep-ex]`.

[51] J. P. Lees *et al.*, *Study of CP violation in Dalitz-plot analyses of $B^0 \to K^+K^-K^0_{(S)}$, $B^+ \to K^+K^-K^+$, and $B^+ \to K^0_{(S)}K^0_{(S)}K^+$*, Phys. Rev. **D85** (2012) 112010, DOI: `10.1103/PhysRevD.85.112010`, `arXiv:1201.5897 [hep-ex]`.

[52] M. Beneke, *Corrections to* $\sin(2\beta)$ *from CP asymmetries in* $B^0 \rightarrow (\pi^0, \rho^0, \eta, \eta', \omega, \phi) K^0_S$ *decays*, Phys. Lett. **B620** (2005) 143–150, DOI: `10.1016/j.physletb.2005.06.045`, `arXiv:hep-ph/0505075 [hep-ph]`.

[53] A. Abashian *et al.*, *The Belle detector*, Nuclear Instruments and Methods in Physics Research Section A: Accelerators, Spectrometers, Detectors and Associated Equipment **479**.1 (2002), Detectors for Asymmetric B-factories 117–232, ISSN: 0168-9002, DOI: `https://doi.org/10.1016/S0168-9002(01)02013-7`.

[54] B. Pal *et al.*, *Observation of the decay* $B^0_s \rightarrow K^0\overline{K}^0$, Phys. Rev. Lett. **116**.16 (2016) 161801, DOI: `10.1103/PhysRevLett.116.161801`, `arXiv:1512.02145 [hep-ex]`.

[55] A. Ali *et al.*, *Charmless nonleptonic* B_s *decays to PP, PV, and VV final states in the perturbative QCD approach*, Phys. Rev. D **76** (7 2007) 074018, DOI: `10.1103/PhysRevD.76.074018`, `https://link.aps.org/doi/10.1103/PhysRevD.76.074018`.

[56] M. Beneke and M. Neubert, *QCD factorization for* $B \rightarrow PP$ *and* $B \rightarrow PV$ *decays*, Nucl. Phys. **B675** (2003) 333–415, DOI: `10.1016/j.nuclphysb.2003.09.026`, `arXiv:hep-ph/0308039 [hep-ph]`.

[57] A. R. Williamson and J. Zupan, *Two body B decays with isosinglet final states in SCET*, Phys. Rev. **D74** (2006), [Erratum: 10.1103/PhysRevD.74.03901] 014003, DOI: `10.1103/PhysRevD.74.014003`, `arXiv:hep-ph/0601214 [hep-ph]`.

[58] L. Evans and P. Bryant, *LHC Machine*, JINST **3** (2008), ed. by L. Evans S08001, DOI: `10.1088/1748-0221/3/08/S08001`.

[59] M. Lamont, *Status of the LHC*, J. Phys. Conf. Ser. **455** (2013) 012001, DOI: `10.1088/1742-6596/455/1/012001`.

[60] C. Lefèvre, *The CERN accelerator complex. Complexe des accélérateurs du CERN*, 2008, `https://cds.cern.ch/record/1260465/files/0812015.pdf` (visited on 2015-07-21).

[61] G. Aad *et al.*, *The ATLAS Experiment at the CERN Large Hadron Collider*, JINST **3** (2008) S08003, DOI: `10.1088/1748-0221/3/08/S08003`.

[62] S. Chatrchyan *et al.*, *The CMS experiment at the CERN LHC*, JINST **3** (2008) S08004, DOI: `10.1088/1748-0221/3/08/S08004`.

[63] G. Aad *et al.*, *Observation of a new particle in the search for the Standard Model Higgs boson with the ATLAS detector at the LHC*, Phys.Lett. **B716** (2012) 1–29, DOI: `10.1016/j.physletb.2012.08.020`, `arXiv:1207.7214 [hep-ex]`.

[64] S. Chatrchyan *et al.*, *Observation of a new boson at a mass of 125 GeV with the CMS experiment at the LHC*, Phys. Lett. **B716** (2012) 30–61, DOI: `10.1016/j.physletb.2012.08.021`, `arXiv:1207.7235 [hep-ex]`.

[65] K. Aamodt *et al.*, *The ALICE experiment at the CERN LHC*, JINST **3** (2008) S08002, DOI: `10.1088/1748-0221/3/08/S08002`.

[66] G. Anelli *et al.*, *The TOTEM experiment at the CERN Large Hadron Collider*, JINST **3** (2008) S08007, DOI: `10.1088/1748-0221/3/08/S08007`.

[67] O. Adriani *et al.*, *The LHCf detector at the CERN Large Hadron Collider*, JINST **3** (2008) S08006, DOI: `10.1088/1748-0221/3/08/S08006`.

[68] B. Acharya *et al.*, *The Physics Programme Of The MoEDAL Experiment At The LHC*, Int. J. Mod. Phys. **A29** (2014) 1430050, DOI: `10.1142/S0217751X14300506`, `arXiv:1405.7662 [hep-ph]`.

[69] R. Aaij *et al.*, *Measurement of J/ψ production in pp collisions at $\sqrt{s} = 7$ TeV*, Eur.Phys.J. **C71** (2011) 1645, DOI: `10.1140/epjc/s10052-011-1645-y`, `arXiv:1103.0423 [hep-ex]`.

[70] R. Aaij *et al.*, *Production of J/ψ and Υ mesons in pp collisions at $\sqrt{s} = 8$ TeV*, JHEP **1306** (2013) 064, DOI: `10.1007/JHEP06(2013)064`, `arXiv:1304.6977 [hep-ex]`.

[71] B. Rachwał, *Production Measurements at the LHCb*, Acta Phys. Polon. **B48** (2017) 1157–1166, DOI: `10.5506/APhysPolB.48.1157`.

[72] K. Olive *et al.*, *Review of Particle Physics*, Chin. Phys. **C38** (2014) 090001, DOI: `10.1088/1674-1137/38/9/090001`.

[73] The LHCb Collaboration, *$b\bar{b}$ Production Angle Plots*, `http://lhcb.web.cern.ch/lhcb/speakersbureau/html/bb_ProductionAngles.html` (visited on 2018-08-01).

[74] J. Alves A. Augusto *et al.*, *The LHCb Detector at the LHC*, JINST **3** (2008) S08005, DOI: `10.1088/1748-0221/3/08/S08005`.

[75] C. Ilgner *et al.*, *The Beam Conditions Monitor of the LHCb Experiment* (2010), `arXiv:1001.2487 [physics.ins-det]`.

[76] R. Aaij *et al.*, *LHCb Detector Performance*, Int. J. Mod. Phys. **A30** (2015) 1530022, DOI: `10.1142/S0217751X15300227`, `arXiv:1412.6352 [hep-ex]`.

[77] D. van Eijk *et al.*, *Radiation hardness of the LHCb Outer Tracker*, Nucl. Instrum. Meth. **A685** (2012) 62–69, DOI: `10.1016/j.nima.2012.05.033`.

[78] T. Ruf, *Web Page of a Panoramix User*, `http://lhcb-reconstruction.web.cern.ch/lhcb-reconstruction/panoramix/running_panoramix.htm` (visited on 2018-09-05).

[79] R. Aaij *et al.*, *The LHCb Trigger and its Performance in 2011*, JINST **8** (2013) P04022, DOI: `10.1088/1748-0221/8/04/P04022`, `arXiv:1211.3055 [hep-ex]`.

[80] J. Albrecht *et al.*, *Performance of the LHCb High Level Trigger in 2012*, J. Phys. Conf. Ser. **513** (2014) 012001, DOI: `10.1088/1742-6596/513/1/012001`, `arXiv:1310.8544 [hep-ex]`.

[81] B. Sciascia, *LHCb Run 2 trigger performance*, *16th International Conference on B-Physics at Frontier Machines (BEAUTY2016)*, 2016 29.

[82] *The* `Gaudi` *Project*, `http://cern.ch/proj-gaudi/` (visited on 2018-06-13).

[83] *The* `Brunel` *Project*, `http://lhcb-release-area.web.cern.ch/LHCb-release-area/DOC/brunel/` (visited on 2018-06-13).

[84] R. W. Forty, *Track Seeding*, tech. rep. LHCb-2001-109, revised version number 1 submitted on 2001-10-12 16:38:05, Geneva: CERN, 2001.

[85] M. Needham, *Clone track identification using the Kullback-Liebler distance* (2008), `http://cds.cern.ch/record/1082460`.

[86] E. Bos *et al.*, *The Trajectory Model for Track Fitting and Alignment*, tech. rep. LHCb-2007-008. CERN-LHCb-2007-008, Geneva: CERN, 2007.

[87] *The* `DaVinci` *Project*, `http://lhcb-release-area.web.cern.ch/LHCb-release-area/DOC/davinci/` (visited on 2018-08-14).

[88] `ROOT`, `http://root.cern.ch` (visited on 2018-08-14).

[89] *The* `Gauss` *Project*, `http://lhcb-release-area.web.cern.ch/LHCb-release-area/DOC/gauss/` (visited on 2018-06-13).

[90] M. Clemencic *et al.*, *The LHCb simulation application, Gauss: Design, evolution and experience*, J. Phys. Conf. Ser. **331** (2011), ed. by S. C. Lin 032023, DOI: `10.1088/1742-6596/331/3/032023`.

[91] T. Sjostrand, S. Mrenna, and P. Z. Skands, *PYTHIA 6.4 Physics and Manual*, JHEP **0605** (2006) 026, DOI: `10.1088/1126-6708/2006/05/026`, `arXiv:hep-ph/0603175 [hep-ph]`.

[92] T. Sjöstrand *et al.*, *An Introduction to PYTHIA 8.2*, Comput. Phys. Commun. **191** (2015) 159–177, DOI: `10.1016/j.cpc.2015.01.024`, `arXiv:1410.3012 [hep-ph]`.

[93] D. Lange, *The EvtGen particle decay simulation package*, Nucl. Instrum. Meth. **A462** (2001) 152–155, DOI: `10.1016/S0168-9002(01)00089-4`.

[94] S. Agostinelli *et al.*, `Geant4`*: A Simulation toolkit*, Nucl. Instrum. Meth. **A506** (2003) 250–303, DOI: `10.1016/S0168-9002(03)01368-8`.

[95] J. Allison *et al.*, `Geant4` *developments and applications*, Nuclear Science, IEEE Transactions on **53**.1 (2006) 270–278, ISSN: 0018-9499, DOI: `10.1109/TNS.2006.869826`.

[96] *The* `Boole` *Project*, `http://lhcb-release-area.web.cern.ch/LHCb-release-area/DOC/boole/` (visited on 2018-06-13).

[97] *LHCb trigger schemes*, `http://lhcb.web.cern.ch/lhcb/speakersbureau/html/TriggerScheme.html` (visited on 2015-07-24).

[98] R. Aaij *et al.*, *LHCb VELO Upgrade Technical Design Report* (2013), `http://cds.cern.ch/record/1624070`.

[99] R. Aaij *et al.*, *LHCb PID Upgrade Technical Design Report* (2013), `http://cds.cern.ch/record/1624074`.

[100] W. D. Hulsbergen, *Decay chain fitting with a Kalman filter*, Nucl. Instrum. Meth. **A552** (2005) 566–575, DOI: `10.1016/j.nima.2005.06.078`, `arXiv:physics/0503191 [physics]`.

[101] F. James and M. Roos, *Minuit: A System for Function Minimization and Analysis of the Parameter Errors and Correlations*, Comput. Phys. Commun. **10** (1975) 343–367, DOI: `10.1016/0010-4655(75)90039-9`.

[102] W. Verkerke and D. P. Kirkby, *The RooFit toolkit for data modeling*, *Statistical problems in particle physics, astrophysics and cosmology*, ed. by L. Lyons and M. Karagoz, 2006 310, `arXiv:physics/0306116 [physics]`.

[103] M. Pivk and F. R. Le Diberder, *SPlot: A Statistical tool to unfold data distributions*, Nucl. Instrum. Meth. **A555** (2005) 356–369, DOI: `10.1016/j.nima.2005.08.106`, `arXiv:physics/0402083 [physics.data-an]`.

[104] A. Rogozhnikov, *Reweighting with Boosted Decision Trees*, `http://arogozhnikov.github.io/2015/10/09/gradient-boosted-reweighter.html` (visited on 2018-08-15).

[105] J. H. Friedman, *Greedy Function Approximation: A Gradient Boosting Machine*, Ann. Statist. **Volume 29, Number 5** (2001) 1189–1232.

[106] L. Mason *et al.*, 'Boosting Algorithms as Gradient Descent', *Advances in Neural Information Processing Systems 12*, ed. by S. Solla, T. Leen, and K. Müller, MIT Press, 1999 512–518.

[107] L. Anderlini *et al.*, *The PIDCalib package*, tech. rep. LHCb-PUB-2016-021.

[108] V. V. Gligorov, C. Thomas, and M. Williams, *The HLT inclusive B triggers*, tech. rep. LHCb-PUB-2011-016. CERN-LHCb-PUB-2011-016. LHCb-INT-2011-030, LHCb-INT-2011-030, Geneva: CERN, 2011, `https://cds.cern.ch/record/1384380`.

[109] R. Aaij *et al.*, *Observation of the* $\Lambda_b^0 \to \Lambda\phi$ *decay*, Phys. Lett. **B759** (2016) 282–292, DOI: `10.1016/j.physletb.2016.05.077`, `arXiv:1603.02870 [hep-ex]`.

[110] D. Martínez Santos and F. Dupertuis, *Mass distributions marginalized over per-event errors*, Nucl. Instrum. Meth. **A764** (2014) 150–155, DOI: `10.1016/j.nima.2014.06.081`, `arXiv:1312.5000 [hep-ex]`.

[111] M. Oreglia, *A Study of the Reactions* $\psi' \to \gamma\gamma\psi$, Ph.D. thesis, Stanford University, 1980; J. Gaiser, *Charmonium Spectroscopy From Radiative Decays of the* J/ψ *and* ψ', Ph.D. thesis, Stanford University, 1982; T. Skwarnicki, *A study of the radiative CASCADE transitions between the Upsilon-Prime and Upsilon resonances*, Ph.D. thesis, Cracow, INP, 1986.

[112] I. Abt *et al.*, *K^* and ϕ meson production in proton-nucleus interactions at $\sqrt{s} =$* 41.6 GeV, Eur. Phys. J. **C50** (2007) 315–328, DOI: `10.1140/epjc/s10052-007-0237-3`, `arXiv:hep-ex/0606049 [hep-ex]`.

[113] G. A. Cowan, D. C. Craik, and M. D. Needham, *RapidSim: an application for the fast simulation of heavy-quark hadron decays*, Comput. Phys. Commun. **214** (2017) 239–246, DOI: `10.1016/j.cpc.2017.01.029`, `arXiv:1612.07489 [hep-ex]`.

[114] G. Punzi, *Sensitivity of searches for new signals and its optimization*, eConf **C030908** (2003), [79 (2003)] MODT002, `arXiv:physics/0308063 [physics]`.

[115] *Updated average f_s/f_d b-hadron production fraction ratio for* 7 TeV *pp collisions*, LHCb-CONF-2013-011 (2013).

[116] U. Uwer, *Revised SciFi stereo-layer geometry*, tech. rep. LHCb-INT-2017-010. CERN-LHCb-INT-2017-010, Geneva: CERN, 2017, `https://cds.cern.ch/record/2264922`.

[117] B. D. Leverington, *The LHCb Upgrade Scintillating Fibre Tracker*, PoS **TIPP2014** (2014) 113. 8 p, `https://cds.cern.ch/record/2014696`.

[118] F. D. Brooks, *Development of organic scintillators*, Nuclear Instruments and Methods **162** (1979) 477505, DOI: `10.1016/0029-554X(79)90729-8`.

[119] H. Leutz, *Scintillating fibres*, Nuclear Instruments and Methods in Physics Research Section A: Accelerators, Spectrometers, Detectors and Associated Equipment **364** (1995) 422448, DOI: `10.1016/0168-9002(95)00383-5`.

[120] L. Collaboration, *LHCb Tracker Upgrade Technical Design Report*, tech. rep. CERN-LHCC-2014-001. LHCB-TDR-015, 2014, `http://cds.cern.ch/record/1647400`.

[121] T. Förster, *Zwischenmolekulare Energiewanderung und Fluoreszenz*, Annalen der Physik **437**.1-2 () 55–75, DOI: `10.1002/andp.19484370105`.

[122] I. Berlmann, *Handbook of Fluorescence Spectra of Aromatic Molecules*, 2nd, New York and London: Academic Press, 1971.

[123] C. D'Ambrosio *et al.*, *Organic scintillators with large Stokes shifts dissolved in polystyrene*, Nucl. Instrum. Meth. **A307** (1991) 430–435, DOI: `10.1016/0168-9002(91)90214-B`.

[124] M. Deckenhoff, *Scintillating Fibre and Silicon Photomultiplier Studies for the LHCb upgrade*, Presented 23 Feb 2016, PhD thesis, TU Dortmund University, 2015, `http://cds.cern.ch/record/2140068`.

[125] T. O. White, *Scintillating Fibres*, Nucl. Instrum. Meth. **A273** (1988) 820–825, DOI: `10.1016/0168-9002(88)90102-7`.

[126] K. Wick and T. Zoufal, *Unexpected behaviour of polystyrene-based scintillating fibers during irradiation at low doses and low dose rates*, Nuclear Instruments and Methods in Physics Research Section B: Beam Interactions with Materials and Atoms **185**.1 (2001) 341–345, ISSN: 0168-583X, DOI: `https://doi.org/10.1016/S0168-583X(01)00776-5`.

[127] T. Zoufal, *Beeinträchtigung der optischen Eigenschaften und Veränderung der Fluoreszenz von Kunststoffszintillatoren durch Röntgenstrahlung*, PhD thesis, Hamburg U., 2002, DOI: `10.3204/DESY-THESIS-2002-013`.

[128] J. Blaha *et al.*, *Scintillating fibers for particle physics experiments — on-line-induced absorption measurements in gamma radiation field*, Radiation Measurements **38**.4 (2004), Proceedings of the 5th European Conference on Luminescent Detectors and Transformers of Ionizing Radiation (LUMDETR 2003) 805–808, ISSN: 1350-4487, DOI: `https://doi.org/10.1016/j.radmeas.2004.04.005`.

[129] J. Wallace *et al.*, *Color center annealing in γ - irradiated polystyrene, under vacuum and air atmospheres*, Radiation Physics and Chemistry **41**.1 (1993) 85–100, ISSN: 0969-806X, DOI: `https://doi.org/10.1016/0969-806X(93)90045-V`.

[130] W. Busjan, K. Wick, and T. Zoufal, *Shortlived absorption centers in plastic scintillators and their influence on the fluorescence light yield*, Nuclear Instruments and Methods in Physics Research Section B: Beam Interactions with Materials and Atoms **152**.1 (1999) 89–104, ISSN: 0168-583X, DOI: `https://doi.org/10.1016/S0168-583X(98)00974-4`.

[131] A. D. Bross and A. Pla-Dalmau, *Radiation damage of plastic scintillators*, IEEE Trans. Nucl. Sci. **39** (1992) 1199–1204, DOI: `10.1109/23.173178`.

[132] R. J. Ekelhof, *Studies for the LHCb SciFi Tracker - Development of Modules from Scintillating Fibres and Tests of their Radiation Hardness*, Presented 18 May 2016, PhD thesis, TU Dortmund University, 2016, `https://cds.cern.ch/record/2212494`.

[133] J. Menne, *The LHCb SciFi Tracker: studies on scintillating fibres and development of quality assurance procedures for the SciFi serial production*, Presented 02 May 2018, 2018, `https://cds.cern.ch/record/2316726`.

[134] M. Deckenhoff, *Simulation of Scintillating Fibres in Geant4*, tech. rep. LHCb-PUB-2014-023. CERN-LHCb-PUB-2014-023. LHCb-INT-2014-009. LHCb-INT-2014-009, Geneva: CERN, 2014, `http://cds.cern.ch/record/1662547`.

[135] S. Agostinelli *et al.*, *GEANT4: A Simulation toolkit*, Nucl. Instrum. Meth. **A506** (2003) 250–303, DOI: `10.1016/S0168-9002(03)01368-8`.

[136] J. Surmann and R. J. Ekelhof, *Simulating the Properties of Scintillating Fibres - The influence of angles and track lengths of photons on the absorption*, tech. rep. LHCb-INT-2016-009. CERN-LHCb-INT-2016-009, Geneva: CERN, 2016, `https://cds.cern.ch/record/2130616`.

[137] T. T. Böhlen *et al.*, *The FLUKA Code: Developments and Challenges for High Energy and Medical Applications*, Nucl. Data Sheets **120** (2014) 211–214, DOI: `10.1016/j.nds.2014.07.049`.

[138] A. Ferrari *et al.*, *FLUKA: A multi-particle transport code (Program version 2005)*, CERN-2005-010, CERN Yellow Reports: Monographs (2005), DOI: `10.5170/CERN-2005-010`.

[139] M. Karacson, *Evaluation of the Radiation Environment of the LHCb Experiment*, TU Vienna, 2016, `https://cds.cern.ch/record/2243499/`.

[140] N. Lopez March and M. Karacson, *Radiation studies for the LHCb tracker upgrade*, tech. rep. LHCb-PUB-2014-022. CERN-LHCb-PUB-2014-022. LHCb-INT-2013-003, Geneva: CERN, 2014, `https://cds.cern.ch/record/1662546`.

[141] M. Calvo Gomez *et al.*, *Studies of a neutron shielding for the upgraded LHCb detector*, tech. rep. LHCb-INT-2017-014. CERN-LHCb-INT-2017-014, Geneva: CERN, 2017, `https://cds.cern.ch/record/2268537`.

[142] A. Kuonen, *Status of SiPM and Flex Cables - talk at SciFi General Meeting*, `https://indico.cern.ch/event/674476/`, 2017.

[143] M. Demmer *et al.*, *Simulation of Light Yield Attenuation Maps for the LHCb SciFi Tracker Upgrade*, tech. rep. LHCb-INT-2016-015. CERN-LHCb-INT-2016-015, Geneva: CERN, 2016, `https://cds.cern.ch/record/2141533`.

[144] V. Bellee *et al.*, *Simulation of the SciFi detector*, tech. rep. LHCb-INT-2018-023. CERN-LHCb-INT-2018-023, Geneva: CERN, 2018, `https://cds.cern.ch/record/2630152`.

[145] M. Clemencic, N. Gilardi, and J. Palacios, *LHCb Conditions Database*, LHCb-2006-017. CERN-LHCb-2006-017 (2006) 9 p, `https://cds.cern.ch/record/951971`.

[146] M. Clemencic, *LHCb Distributed Conditions Database*, tech. rep. LHCb-PROC-2007-023. CERN-LHCb-PROC-2007-023, Geneva: CERN, 2007, `https://cds.cern.ch/record/1431867`.

[147] O. Gerber, *Simulation studies to investigate the effects of radiation dose on the LHCb SciFi detector*, M.Sc. thesis, TU Dortmund University, in preparation.

Danksagung – Acknowledgements

An dieser Stelle möchte ich einigen Personen, ohne die diese Arbeit nicht möglich gewesen wäre, meinen tief empfundenen Dank aussprechen.
Als erstes steht da natürlich mein Doktorvater, Herr Prof. Dr. Spaan. Schon in der Vorlesung „Einführung in die Kern- und Teilchenphysik“, aber auch in weiterführenden Vorlesungen und Seminaren, haben Sie durch die Vermittlung Ihres Wissens und den vielen Anekdoten mein Interesse für die Teilchenphysik zunächst geweckt und anschließend immer wieder entfacht, wenn es mal einzuschlafen drohte. Seit der Bachelorarbeit ermöglichen Sie mir zudem in einem sehr spannenden und internationalen Umfeld zu forschen und mich weiter zu entwickeln, nicht zuletzt durch Ihre Ermutigung mich für ein Promotionsstipendium zu bewerben. Vielen Dank für alles!
Außerdem danke ich Herrn Prof. Dr. Kevin Kröninger, dass er sich trotz des wachsenden Stapels an Abschlussarbeiten auf seinem Schreibtisch dazu bereit erklärt hat, als Zweitgutachter zu fungieren. Ebenfalls danken möchte ich Herrn apl. Prof. Dr. Heinz Hövel und Frau Dr. Julia Nase, die die Prüfungskommission vervollständigen.
Ich danke zudem der Friedrich-Ebert-Stiftung sowie dem Bundesministerium für Bildung und Forschung und der Deutschen Forschungsgemeinschaft für die Unterstützung meiner Promotion und die persönliche Förderung, durch die ich mich voll und ganz auf diese Arbeit konzentrieren konnte und wertvolle Lebenserfahrung sammeln durfte.
Vor der Doktorarbeit kam das Studium. Dieses hätte ich ohne die Beratung von Herrn Prof. Dr. Joachim Stolze vielleicht niemals begonnen. Vielen Dank für die ermutigenden Worte und Ihr Vorbild, dass man auch ohne einschlägige LK-Wahl Physik studieren kann, Herr Stolze!
Kurz vor der Bachelorarbeit machte ich im Rahmen der Übungen zur „Einführung in die Kern- und Teilchenphysik“ Bekanntschaft mit Till Moritz Karbach (†). Dir lieber Moritz möchte ich danken, dass du mich für die experimentelle Teilchenphysik, das CERN und im speziellen das LHCb-Experiment begeistert hast. Du warst mir ein guter Mentor und Kumpel!
Durch Moritz und Herrn Prof. Spaan gelangte ich schließlich zum Lehrstuhl E5. Hier habe ich Laufe der letzten Jahre viele Menschen kennen gelernt, die meinen Lebensweg geprägt haben und teilweise zu Freunden geworden sind. Namentlich möchte ich hier Vanessa, Kevin und Alex für die gemeinsame bereichernde, inspirierende, lustige, entspannte, …Zeit als Bürokollegen und / oder „auf Schichten“ danken, auf euch konnte man sich immer verlassen. Ferner möchte ich unserem SciFi Post-Doc Dr. Robert Ekelhof danken. Lieber Robert, seit der Master-Arbeit warst du immer mein Ansprech- und Diskussionspartner zum Thema SciFi-Tracker und auch über den Arbeitsalltag hinaus hast du mich ertragen, danke! Auch unser Post-Doc a.D., Dr. Julian Wishahi, darf an dieser Stelle nicht fehlen. Trotz seiner neuen Verpflichtungen außerhalb von E5, stand er mir bis zur letzten Seite meiner Doktorarbeit mit wertvollen Ratschlägen zu jeder Lebenslage beiseite. Lieber Julian, ich danke dir sehr!

I would like to thank the LHCb BnoC and SciFi Simulation working groups at CERN for the precious input that helped a lot in retrieving the results shown in this thesis. I would like to thank our analysis note reviewers Wenbin and Matt, and all other LHCb colleagues who helped to polish our analysis approach.

Besonders hervorheben unter diesen zu Freunden gewordenen Bürokollegen möchte ich an dieser Stelle Timon Schmelzer. Danke lieber Timon, dass du dich zusammen mit mir durch diese Analyse gekämpft hast und zusammen auch mal bisher in der Arbeitsgruppe nicht „erforschte Pfade“, wie das Arbeiten mit Python, beschritten hast. Bis zuletzt hatten wir immer was zu lachen und auch privat bist du mir immer ein guter Freund gewesen, dafür danke ich dir sehr!

So eine Doktorarbeit ist eigentlich undenkbar durch die Unterstützung durch Familie und Freunde, deshalb möchte ich an dieser Stelle auch meinen Eltern und Geschwistern danken.

Lieber Ramon, wir kennen uns seit dem ersten Tag unseres Physik-Studiums und über die Jahre sind wir gute Freunde geworden, was sich immer am besten in den schwierigen Zeiten des Lebens zeigt. Ich danke dir von Herzen für deine Freundschaft und Unterstützung, nicht nur aber auch in der heißen Phase dieser Arbeit!

Lieber Kai, dass das geflügelte Wort „Freund – Feind – Parteifreund“ auf dich nicht zutrifft habe ich schnell bemerkt. Ganz im Gegenteil sind wir in den letzten Jahren zu guten Freunden geworden, was sehr zu meiner persönlichen Entwicklung beigetragen hat. Danke, dass es dich gibt!

Zu guter Letzt danke ich in besonderem Maße meiner Freundin Anastasija. Du warst mir ein Quell der Freude, Inspiration und Kraft, hast mir geholfen im Hier und Jetzt zu bleiben und hast es tatsächlich geschafft mich vom Rand des Abschlussphasen-Wahnsinns fern zu halten.

ཇང་ཆུབ་སེམས་ནི་རིནཔོ་ཆེ་
མ་ཀྱེ་པ་ནམས་ཀྱེ་གྱུར་ཅིག་
ཀྱེ་པ་ཉམཔ་མེཔ་ཡང་
གོངནསྨ་གོངདུ་ཕེལ་བུར་ཤོ་

ཨོཾ་མ་ཎི་པདྨེ་ཧཱུཾ་